ANALYSIS AND CONSTITUTIVE MODELING OF DYNAMIC IMPACT BEHAVIOUR OF HAYNES 282 SUPERALLOY

By

NNAEMEKA EMMANUEL UGODILINWA

A thesis submitted to the Faculty of Graduate Studies in partial fulfillment of the requirements for the degree of

MASTER OF SCIENCE

Department of Mechanical Engineering

University of Manitoba, Winnipeg

Canada

ABSTRACT

Haynes 282 is a newly developed nickel-based superalloy that is used in the static and rotating components of aerospace and power generation engines owing to its high-temperature mechanical strength and oxidation resistance. Several studies have reported on the mechanical properties of Haynes 282; however, little information is available on its impact behaviour which is critical in determining the resistance of Haynes 282 to damage under high strain rate loading. Using a direct impact Hopkinson pressure bar, this study investigates the dynamic impact behaviour of Haynes 282 at strain rates that range from 2×10^3 to 9×10^3 s^{-1} and temperatures from 25ºC to 800ºC. The experimental results show that, in contrast to other superalloys, the flow stress of Haynes 282 is less sensitive to the strain rate, a remarkable feature that could ease the machinability of this alloy. It is seen that Haynes 282 is more susceptible to impact failure after aging as opposed to solutionized due to its higher strength and lower strain hardening capability that predisposes it to the formation of adiabatic shear bands. Furthermore, an Arrhenius-type constitutive model is used to model the dynamic impact behaviour of Haynes 282 and this model can be useful in the future for the numerical simulation of high strain rate deformation applications, such as machining, high velocity impact, ballistic impact, and blade containment system in aero engines. Furthermore, the one-step ageing heat treatment developed at the University of Manitoba (900ºC/1 hour/FC) for Haynes 282 shows better tensile properties than the manufacturer's recommended two-step ageing heat treatment (1010ºC/2 hours/AC and 788ºC/8 hours/AC) for the alloy.

ACKNOWLEDGMENT

I would like to thank my advisor, Dr. O. A. Ojo, for the privilege of completing my post-graduate study under his excellent tutelage. I appreciate his guidance, support, mentorship, encouragement, and provision of research facilities for the successful completion of this study. I also thank my co-advisor, Dr. M. R. Khoshdarregi, for his advice and contributions. The immense support of Mr. Gbenga Asala throughout the course of this research work is highly appreciated. I also thank Mike Boskwick and Trevor Smith for their technical assistance.

I extend my gratitude to my colleagues and friends, Francis Amushi, Yemi Aina, Taiwo Dada, Deborah Michael, Masego Boikanyo, Mallikarjuna Thammaiah, Hassan Oyeleja, Oluwasanmi Oguntuase, Chidinma Anyanwu, James Adu, Emmanuel Adejumo, Ibraheem Abdulganiyu, Sixtus Ekezie, Godwin Ajaezi, Alexander Afuberoh, and others too numerous to mention, for their support throughout this journey. The assistance of Dr. L. O. Osoba is highly appreciated.

Finally, I especially thank my parents, Chief and Mrs. Felix Ugodilinwa, and my siblings, for their prayers, love, and support in making this dream a reality.

DEDICATION

I dedicate this dissertation to the almighty God, the giver of all knowledge.

LIST OF ACRONYMS

ASB: Adiabatic Shear Band

ASTM: American Society for Testing and Materials

DRX: Dynamic Recrystallization

EDS: Energy Dispersive Spectroscopy

FCC: Face Centered Cubic

HCP: Hexagonal Closed Packed

JC: Johnson-Cook

SEM: Scanning Electron Microscopy

SHPB: Split Hopkinson Pressure Bar

TCP: Topologically Close-Packed

TABLE OF CONTENTS

LIST OF TABLES

LIST OF FIGURES

CHAPTER 1

INTRODUCTION

1.1 Background Information

The development of alloys that can withstand higher operating temperatures and retain their structural integrity is critical for improving the efficiency of new generation jet turbine engines [1] and reducing the damaging effects of carbon dioxide (CO_2), nitrogen oxide (NOx), and sulphide oxide (SOx) emissions [2], [3]. Haynes 282 is one example of such an alloy, with an operating temperature of up to 800 ^oC. Haynes 282 is a gamma-prime (γ') strengthened nickel (Ni)-based superalloy that has been well received due to its high-temperature mechanical properties, ease of fabricability, ability to resist oxidation, and thermal stability [4]. Compared to similar alloys in the same category, such as Haynes R-41, Waspaloy, and 263 alloy, Haynes 282 has a lower γ' content that provides a unique combination of strength and processability otherwise not currently found in any other commercially available superalloy [5]. Developed primarily for land- and aero-based gas turbine components [5], Haynes 282 has been identified by the U.S Department of Energy as a leading candidate material for steam boiler components in advanced ultra-supercritical (A-USC) power plants, [6], [7] where the steam temperature approach 760^oC and an operating pressure of 36 MPa [8]. Haynes 282 is been considered for use in A-USC power plants as superheater boiler tubing, large steam header piping, casings, and rotors [9]. This new alloy derives its high-temperature usability from the precipitation of γ' particles Ni_3 (aluminum (Al), titanium (Ti)) within the Ni matrix. Additional strengthening is achieved through solid solution strengthening from alloying elements and carbide precipitation along the grain boundaries [10].

The development of a new high-temperature alloy usually originates from the attempts by the research community to gain a better understanding of the mechanical properties of a material to ensure its appropriateness for the intended applications. In addition, researchers in the extant literature have also explored other application areas for a new material. These also apply to Haynes 282, and its mechanical properties are currently being studied by different academics. For instance, Joseph et al. [10] examined the influence of heat treatment on the tensile properties of Haynes 282 and observed that reducing the temperature of the stabilization step during aging resulted in a bimodal γ' distribution and grain boundary γ' without any loss in the tensile and yield strengths. Hawk et al. [8] examined the stability of the γ' precipitates in Haynes 282 at room and higher temperatures by varying the ratio of Al and Ti in Haynes 282. They observed a trans-interface-diffusion-controlled coarsening behavior of the γ' precipitates. Pike [7] reported that Haynes 282 has excellent microstructural stability after exposure to a temperature of 871°C for 16,000 hours. Saarimäki et al. [11] studied time- and cycle-dependent crack propagation in Haynes 282 and observed that at room temperature, cracks grow in a transgranular manner, but transition from cycle-dependent transgranular growth to time-dependent intergranular behaviour at elevated temperatures. For high temperature fatigue behaviour, Rozman et al. [12] observed transgranular crack growth, with limited intergranular cracking. In the same manner, Buckson and Ojo [13] investigated the cyclic deformation characteristics and fatigue crack growth behaviour of Haynes 282 and reported that the alloy has strong resistance against cyclic deformation.

Although a large number of studies have been carried out on the mechanical properties of this new alloy, its dynamic impact behaviour has received little attention in the literature. Recently, Rodríguez-Millán et al. [14] offered some insights into the thermo-viscoplastic behaviour of Haynes 282 at temperatures below 250°C and strain rates up to 2,800/s. However, their

experimental configuration does not consider the in-service temperature of the alloy and typical strain rates found under dynamic impact loading applications, such as machining. This study aims to address the research gap in the literature by investigating the dynamic impact response of Haynes 282 at strain rates from 2 x 10^3 to 9 x 10^3 /s and temperatures that range from 25°C to 800°C.

The impact energy absorbing characteristics of a material, which is beneficial for applications such as in machining, high-velocity projectiles, and ballistic loading, can be assessed through several factors that cause the dynamic shear localization of a material. Dynamic material properties such as strength, work hardening behaviour, strain rate sensitivity, and critical strain to failure can be used to define the behaviour of a candidate material for high impact resistance applications [15]. Work hardening occurs during the early stages of impact deformation due to the generation and motion of dislocations in the lattice which strengthen the material [16]. During the work hardening stage, the material tends to increase in plastic deformation. However, as the deformation progresses, the material undergoes inhomogeneous deformation due to localized strain [17]. This localized deformation leads to adiabatic heating from excessive heat accumulation which results in thermal softening [18]. For γ'-strengthened alloys, the thermal softening effect can be exacerbated by the continual shearing of γ' precipitates that leads to the localization of plastic flow into narrow zones, otherwise known as adiabatic shear bands.

The term “adiabatic shear bands” (ASBs) which originated in [19] imply the absence of heat transfer within the shear bands. However, depending on the thermal diffusivity of the material and other deformation variables, some of the heat from plastic deformation is conducted away from the localized regions [20]. The formation of ASBs during deformation is a major contributor to the catastrophic failure of materials under impact loading. It is well known that adiabatic shear failure

ensues when the rate of thermal softening exceeds that of strain hardening and strain rate hardening/softening in the strengthening of a material during deformation. A widely acknowledged theory that explains for the susceptibility of a material to adiabatic shear failure is based on the stiff competition between the effects of strain hardening and thermal softening during plastic deformation at high strain rates [19], [21]–[23]. Since the flow stress of a material during high strain rate deformation is strongly influenced by the prevailing deformation strain, strain rate, and temperature, Culver [21] derived the condition for the onset of adiabatic instability as:

$$d\sigma = \left(\frac{\partial\sigma}{\partial\varepsilon}\right)_{\dot{\varepsilon},T} d\varepsilon + \left(\frac{\partial\sigma}{\partial\dot{\varepsilon}}\right)_{\varepsilon,T} d\dot{\varepsilon} + \left(\frac{\partial\sigma}{\partial T}\right)_{\dot{\varepsilon},\varepsilon} dT \qquad (1.1)$$

where $\dot{\varepsilon}$ is the deformation strain rate (s^{-1}), T is the absolute temperature (K), σ represents the flow stress (MPa), and ε is the corresponding strain. The first term in Equation 1.1 represents strain hardening, the second and last term denotes strain rate hardening/softening and thermal softening effect, respectively. With constant strain rate deformation, the effect of strain rate hardening/softening can be neglected. Differentiating Equation 1.1 gives the criterion for mechanical instability to occur:

$$\left(\frac{\partial\sigma}{\partial\varepsilon}\right)_{\dot{\varepsilon},T} + \left(\frac{\partial\sigma}{\partial T}\right)_{\dot{\varepsilon},\varepsilon} \frac{\partial T}{\partial\varepsilon} = 0 \qquad (1.2)$$

The expression in Equation 1.2 supposes that if the rate of strain hardening outweighs that of thermal softening, the localization of plastic flow is suppressed thus preventing or delaying the formation of ASBs during dynamic impact deformation. However, when the thermal softening effect from plastic work of deformation dominates strain hardening, a point is reached, which is called the critical strain of deformation, at which mechanical instability sets in, thus leading to catastrophic failure of the material [24]. Moreover, the propensity of a material to form ASBs is

influenced by its microstructure [25], [26]. The microstructural state of a material is affected by the heat treatment to which that material is subjected [27], [28]. Therefore, an understanding of the propensity of a material to form ASBs is important in understanding its resistance to damage under high strain rate loading and also vital is knowing how the ASB formation changes with heat treatment condition.

1.2 Research Objectives

The main objectives of this research work are to:

- investigate the influence of heat treatment on the quasi-static compressive and tensile behaviours of Haynes 282 under three heat treatment conditions (solutionized, standard heat treatment, and special aged),
- evaluate the influence of temperature and strain rate on the dynamic impact behaviour of Haynes 282 under three heat treatment conditions (solutionized, standard heat treatment, and special aged) and the formation of ASB during deformation of the alloy, and
- develop a constitutive model that can predict the high strain rate behaviour of Haynes 282.

1.3 Major Findings

To achieve the objectives, the quasi-static compressive and tensile deformation behaviours of Haynes 282 are examined with a servo hydraulic testing system at room temperature. The dynamic impact behaviour is characterized by using a direct impact Hopkinson bar at strain rates that range from 2×10^3 to 9×10^3 /s and temperatures from 25°C to 800°C.

The experimental results show that under quasi-static compressive and tensile loading, Haynes 282 has the highest strength after the special aged heat treatment, followed by standard heat

treatment, whilst the lowest strength is observed after solutionizing. The alloy strain hardens more after solutionizing as opposed to aging. The special aged process that was developed at the University of Manitoba (900^{o}C/1 hour/furnace cooled (FC)) results in higher hardness, higher yield strength and better ductility than the manufacturer's recommended heat treatment for Haynes 282 (1010^{o}C/2 hours/air-cooled (AC) and 788^{o}C/8 hours/AC).

Under impact loading, a similar trend, as observed under quasi-static deformation, is seen in the strength and strain hardening capability of Haynes 282 for the three heat treatment conditions. However, the higher strength and lower strain hardening behaviour of the alloy after the special aged heat treatment, which are desirable features under quasi-static loading, predisposes this alloy to form ASBs under impact loading. The flow stress of Haynes 282 shows a near constant to negative dependence on the strain rate at room and higher temperatures after undergoing all three types of heat treatments, a remarkable feature that could reduce its machinability. In addition, it is seen that the flow stress of this alloy decreases with increases in deformation temperature at all the strain rates investigated. Scanning electron microscopy (SEM) images of the fractured samples after aging show the presence of cracks that emanate from the ASBs and dissolution of the main strengthening phase of the alloy, that is, the γ' precipitate phase, in the ASBs. These could be attributed to the effect of adiabatic heating, γ' precipitate, and strain-enhanced diffusion during impact deformation.

It is found that a constitutive model that uses an Arrhenius-type phenomenological equation can predict the observed dynamic impact behaviour of Haynes 282. The model is useful for the numerical simulation of high strain rate applications, such as machining, ballistic impact, and blade containment system in aero engines.

1.4 Thesis Structure

The layout of this dissertation is as follows:

- Chapter 1 provides the background information, motivation for the study, research objectives, and the major findings of this study.
- Chapter 2 is a literature review of superalloys and their technological importance, the physical metallurgy of Haynes 282, deformation mechanics at high strain rates, and the use of constitutive models to predict the high strain rate of materials.
- Chapter 3 outlines the material, heat treatment procedures, and the experimental methodology adopted to achieve the research objectives.
- Chapter 4 is a discussion on the microstructural characterization of Haynes 282 under the different types of heat treatments applied in this study. The results obtained under quasi-static and dynamic impact deformation conditions are analyzed. The constitutive equation that predicts the dynamic impact response of Haynes 282 is presented and the prediction accuracy of the proposed model is validated.
- Finally, Chapter 5 provides a summary and a conclusion on the findings in this study and recommendations for future work.

CHAPTER 2

LITERATURE REVIEW

2.1 Introduction

The first use of the term “superalloy” is believed to be in the mid-1940, shortly after World War II, to describe a group of high temperature, heat-resistant alloys of Ni, Ni–iron (Fe), or cobalt (Co) that have a unique combination of mechanical strength at high temperatures and resistance to surface deterioration [29], [30]. Primarily developed for use in turbo superchargers [31] and the hottest sections of gas turbine aero-engines [29], the origin of superalloys and their technological development are correlated with the advancement of gas turbine jet engines for military applications [32]. Their development has evolved over the years as shown in Figure 2.1. Designers can now select from a wide range of these alloys for use, including the recently introduced Haynes 282 superalloy. Superalloys can function effectively for extended periods at temperatures of up to 1000^{o}C, thus rendering them the ideal engineering material for use in modern jet engines as shown in Figure 2.2. Increasing the maximum temperature that can be tolerated in the turbine section of a jet engine increases engine thrust and reduces fuel consumption [33], which result in a substantial improvement in the efficiency, durability, and reliability of gas turbine engines. This improvement is attributed, in part, to the development of superalloys, a feat unrealizable by using other metallic materials. Recently, they have found tremendous use in nuclear reactors, steam turbine power generating plants, petrochemical plants, metal processing, the medical and biomedical industries, and other challenging applications [29], [34]. They can be processed in both wrought and cast forms or by powder metallurgy depending on the application. Superalloys are broadly classified as Fe-, Co-, or Ni-based alloys [35].

This item has been removed due to copyright issues. To view it, visit:

https://link.springer.com/article/10.1007/s11665-015-1711-y

Figure 2.1: Elevated temperature capability of superalloys from 1940 to 2010 [8]

(a)

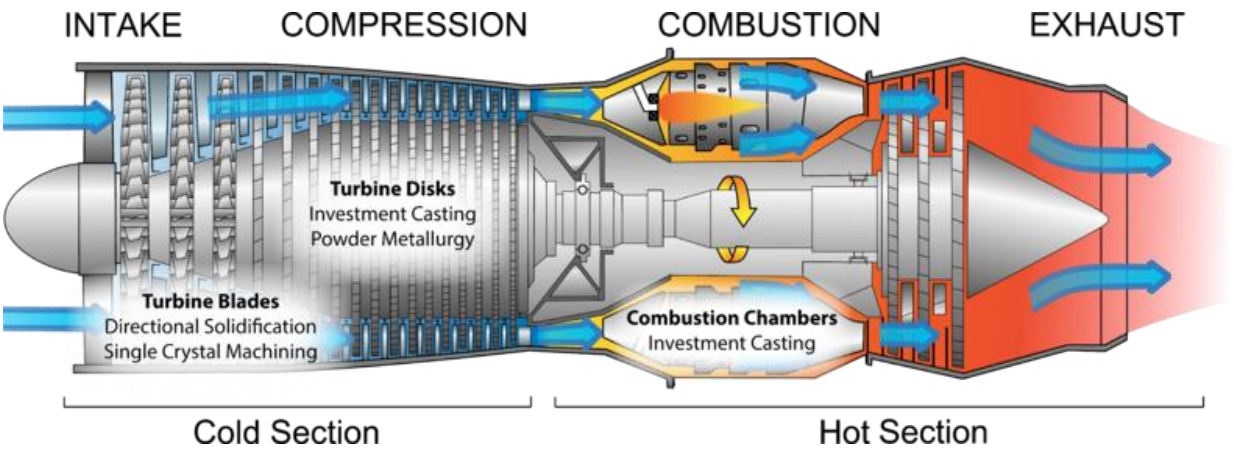

(b)

This item has been removed due to copyright issues. To view it, visit:

https://www.slideshare.net/johnpsilk/ati-jet-engine

Figure 2.2: Overview of aircraft gas turbine engine: (a) air flow from inlet to outlet with corresponding temperature increase [36] and (b) material selection for different sections in engine [37].

2.2 Superalloys: Classification and Applications

2.2.1 Iron-based Superalloys

Fe-based superalloys emanated from austenitic stainless steels and are based on the principle of combining a face-centered cubic (FCC) close-packed matrix (15% – 60% Fe) with precipitate-forming and solid-solution strengthening elements, such as Al, niobium (Nb), and carbon (C) [38]. The FCC phase is stabilized by using a minimum of 25% Ni addition for solid-solution strengthening and chromium (Cr) for oxidation and hot corrosion resistance [33], [38]. These alloys are known to be more affordable and also expand less at high temperatures than Ni- or Co-based superalloys, making them ideal for use as discs, casings, and blades in aero engines [33]. Fe-based superalloys can be strengthened in three different ways: martensitic transformation, hot and cold working of the austenitic alloy, and precipitation strengthening of the austenitic alloy with γ' [Ni_3 (Al, Ti), $L1_2$], γ'' (Ni_3Nb, DO_{22}), and carbide phases ($M_{23}C6$, M_6C) [33], [38], [39]. Strengthening by precipitation is achieved by the addition of Ni, Al, Nb, and Ti to the matrix. Ti primarily forms γ'. γ'', which is a body-centered tetragonal structure, is precipitated due to the presence of Nb [39]. The effect of alloying elements on this class of superalloys is shown in Table 2.1. Fe-based superalloys have a high tendency to form deleterious topologically close-packed (TCP) phases, which have a plate-like morphology [40], such as sigma, Laves, and mu [39]. These alloys are commonly Inconel X750, A-286, V-57, Hastelloy X, Pyromet 860, and Inconel 718, which is the most widely used Ni-Fe superalloy to date [39]. They have found substantial applications in gas turbine engines as blades, rotors, disks, etc. [41].

Table 2.1: Effects of Alloying Elements in Nickel-Iron-Based Superalloys [42]

Element	**Possible Effects***
Aluminum, Titanium	Form γ′ precipitates; Al retards the formation of the eta phase and Ti enhances the formation of the MC carbide phase
Chromium	Enhances oxidation resistance and solid solution strengthening
Molybdenum, Tungsten	Solid solution strengthening and form M_6C carbides
Phosphorus	Aids overall precipitation of carbide phases
Carbon	Forms primary and secondary carbides (MC, M_6C, M_7C_3, and $M_{23}C_6$). Used to stabilize FCC matrix
Niobium	Forms γ″ and delta-phase
Boron, Zirconium	Enhances rupture life and retards the formation of eta phase
Tantalum	Used for solid solution strengthening and forms MC carbides.
Nitrogen	Forms M (C, N) carbonitrides
Nickel	Stabilizes FCC matrix; forms γ′ and γ″ precipitates, and inhibits the formation of deleterious phases

*These effects may not take place at the same time in the material

2.2.2 Cobalt-based Superalloys

Co-based superalloys are strengthened by solid-solutions and refractory metal carbides, usually a combination of 0.4 – 0.85% of C and other metals, such as molybdenum (Mo), Nb, tantalum (Ta) and tungsten (W), which tend to segregate at the grain boundaries [38], [43]. They also contain high levels of Cr which increase their resistance to corrosion in aggressive environments [38]. The contribution of alloying elements to a typical Co-based superalloy is illustrated in Table 2.2. Co-based superalloys depend on carbide formation as their main strengthening mechanism, since the precipitation of intermetallic compounds in the alloy can cause severe embrittlement issues [30]. Although they are known to have less mechanical strength than Ni-based superalloys, their tendency to retain their strength at high temperatures and their minimal sensitivity to hot cracking make them useful for applications that require hot working or welding, such as in the intricate parts of a gas turbine combustion chamber, transition ducts, and turbine vanes [38], [44]. They are also utilized for applications where resistance to hot corrosion is a critical factor and components that experience less structural stress at moderate to high temperatures [45]. X-40, one of the first Co-based superalloys fabricated by Thielemann [46] in 1943, is used in the first stage nozzle of turbines [43]. Co-based alloys, such as Haynes 188, Haynes 25, S-816, MAR-M 302, and FSX-414, have been successfully utilized in gas turbine engines [45].

The demand for Co-based superalloys has increased over the years largely due to the limitations in developing Ni-based superalloys that can withstand higher temperatures for increased turbine efficiency [46]. Co-based superalloys are thought to have excellent hot corrosion resistance in the most aggressive environments due to the formation of thermodynamically stable protective oxide layers, such as chromium(III) oxide (Cr_2O_3) and aluminum oxide (Al_2O_3) [47]. In addition, they have better creep resistance properties and improved weldability compared to other classes of

superalloys [48]. However, they have limited structural stability, which is manifested as an in-service reduction in ductility, due to the phase transformation effect of Co [49]. Thermodynamically, pure Co is an allotropic element which transforms from a hexagonal close-packed (HCP) to FCC structure [49]–[51] at ~419^{o}C. The FCC crystal structure, which is stable at high temperatures, is stabilized with the use of elements such as Ni, C, and Ta to avoid the deleterious effect of service-induced FCC to HCP transformation in the alloy [52].

Table 2.2: Effects of Alloying Elements in Cobalt-Based Superalloys [42]

Element	**Possible Effects***
Aluminum	Increases oxidation resistance and forms CoAl.
Titanium	Forms MC carbides, Co_3Ti, and Ni_3Ti in exceptional cases**
Chromium	Hot corrosion and oxidation resistance, and forms M_7C_3, and $M_{23}C_6$ carbides.
Molybdenum, Tungsten	Solid solution strengthening and forms M_6C carbides and Co_3M.
Carbon	Forms primary and secondary carbides – MC, M_6C, M_7C_3, and $M_{23}C_6$.
Nickel	Stabilizes FCC matrix, and forms γ' in exceptional cases**
Boron and Zirconium	Enhances rupture strength
Tantalum and Niobium	Solid solution strengthening, forms MC carbides and increases oxidation resistance

*These effects may not take place at the same time in the material

**With sufficient nickel addition

2.2.3 Nickel-based Superalloys

The first Ni-based superalloy, Nimonic-75, was developed in 1940 for the gas turbine engine of British aviation engineer, Frank Whittle [53]. Nimonic-75 was an adaptation of Nichrome-V by adding 0.1% C and 0.3% Ti [54]. In Britain, Nimonic 80 was introduced in 1941 by increasing the Ti content followed by Nimonic 80A with a low Fe content; Nimonic 90 with a higher Co content; and Nimonic 100 with an increased Mo content, all with the intent to enhance the temperature capability of these new "super" alloys [53]. In the United States, Inconel-X that was a modification of Inconel (15% Cr, 7% Fe, and 78% Ni), was the first Ni-based superalloy that was developed by controlled additions of Ti, Al, Nb, Co, and other minor elements. These alloys have a more superior high-temperature strength and corrosion resistance than stainless steels and to further increase their thermal stability, the controlled addition of Al and Ti to the Ni matrix resulted in the precipitation of a coherent γ' phase [55]. This γ' phase confers exceptional strength to Ni-based superalloys.

The Ni content usually ranges from 30% to 75%, with Cr additions up to 30% to provide outstanding oxidation resistance. The Fe content in this class of superalloy is minimal and in most cases, limited to a specified amount. Table 2.3 lists the main alloying elements and their effects on Ni-based superalloys. Typical γ'-strengthened alloys include wrought alloys such as Waspaloy, Astroloy, Haynes 282, U-700, the Inconel 600 series, and cast alloys such as Mar-M-247, IN-713, and Rene 80 [34]. Ni-based superalloys are the most widely used engineering materials in the hottest sections of a component as they can withstand the highest homologous temperatures compared to other alloys for structural applications [56]. Alloys such as Inconel 600, 601, and 690 are used for combustion systems, gas turbines, nuclear reactors, chemical processing plants, furnace parts, and heat-treatment equipment [57], [58].

Table 2.3: Effects of Alloying Elements in Nickel-Based Superalloys [42]

Element	**Possible Effects***
Aluminum, Titanium	Al and Ti form γ′ precipitates; Ti forms MC carbides and Al forms protective oxide coating - Al_2O_3
Chromium	Hot corrosion and oxidation resistance, and solid solution strengthening
Molybdenum, Tungsten	Solid solution strengthening and forms M_6C carbides
Cobalt	Increases γ′ solvus temperature
Carbon	Forms primary and secondary carbides – MC, M_6C, M_7C_3, and $M_{23}C_6$.
Niobium	Forms γ″ and delta-phase
Boron, Zirconium	Enhances rupture life; boron forms borides in some alloys
Tantalum	Solid solution strengthening; forms MC carbides, and increases oxidation resistance

*These effects may not take place at the same time in the material

2.3 Physical Metallurgy of Haynes 282 Superalloy

The nominal composition of Haynes 282 superalloy is shown in Table 2.4. The addition of 20 wt.% Cr provides resistance to hot corrosion and oxidation, whilst a low level of Co controls the γ′ solvus temperature of the alloy [5]. The excellent creep strength of Haynes 282 is attributed to the presence of 8.5 wt.% Mo through solid-solution strengthening [5]. Controlled additions of Al and Ti, which are γ′ forming elements, are required as small variations of these alloying elements significantly affect the processability and mechanical properties of the alloy at elevated temperatures. Minor additions of C and boron (B) enhance the mechanical properties, whilst manganese (Mn), silicon (Si), and Fe are restricted to a specific maximum amount in the alloy [5]. The phases, such as the γ-matrix (Ni-based), γ′ precipitates (Al- and Ti-based), primary MC carbides (Mo- and Ti-rich), M_5B_3 (Mo-rich), secondary $M_{23}C_6$ carbides (Cr-rich), and M_6C carbides (Mo-rich), reported in Haynes 282 in the mill annealed condition and after standard heat treatment will be briefly discussed [10], [59]–[61].

Table 2.4: Nominal composition of Haynes 282 superalloy [62]

Element	Weight %
Nickel (Ni)	balance
Cobalt (Co)	10
Chromium (Cr)	20
Molybdenum (Mo)	8.5
Aluminum (Al)	1.5
Titanium (Ti)	2.1
Iron (Fe)	1.5 maximum
Manganese (Mn)	0.3 maximum
Silicon (Si)	0.15 maximum
Carbon (C)	0.06
Boron (B)	0.005

2.3.1 Nickel Matrix (γ phase)

Ni, a silvery-white lustrous metal, is the fifth most abundant element in the earth's crust. It occurs naturally in sulfides, arsenides, oxides, and silicates [63]. Ni has an FCC structure with an atomic number of 28 and belongs to the 4D block of transition metals in the periodic table. It is found in 5 stable isotopes, with an average atomic weight of 58.71 [64], [65]. Table 2.1 lists the physical properties of pure Ni and those of Haynes 282. Ni, with a density of 8.9 g/cm^3, is denser than competing metals for aerospace applications, such as Al and Ti with a density of 2.7 g/cm^3 and 4.5 g/cm^3, respectively. However, Ni is preferred by materials engineers as the γ matrix for most high-temperature alloys owing to its nearly filled third electron shell which provides high tolerance for significant alloying without undergoing phase instability [66] at all austenitic temperatures up to its absolute melting point. Also, its tendency to form stable Al-rich oxides for oxidation resistance and a Cr-rich protective layer which restricts outwards diffusion of elements and ingress of elements such as oxygen, nitrogen, and sulfur, renders Ni the preferred element for the γ matrix [66].

The gamma (γ) phase in Haynes 282 is a continuous matrix of FCC Ni-based austenite [65], [67] which contains solid solution strengtheners, such as, Co, Cr, Al, Ti, and Mo, and their corresponding effect is directly related to the atomic radii difference between the solute and host atoms [68].

Table 2.5: Physical properties of pure nickel and Haynes 282 at room temperature

Property	**Pure Nickel**	**Haynes 282**
Crystal Structure	FCC	FCC
Density (g/cm^3)	8.9	8.29*
Melting point (^oC)	1453	1300 - 1375
Elastic modulus (GPa)	207	217
Shear modulus (GPa)	76	82
Poisson's Ratio	0.31	0.319
0.2% Offset Yield Strength (MPa)	-	715**
Ultimate Tensile Strength (MPa)	-	1147**
% Elongation	-	30**

*Standard heat treatment

**Standard heat-treated plate samples

2.3.2 Gamma-prime (γ′) Phase

Gamma-prime (γ′) is a primitive cubic intermetallic compound that confers high-temperature strength to Haynes 282. γ′ precipitates have an ordered $L1_2$ FCC structure of nominal composition Ni_3 (Al, Ti) with Ni atoms at the face centers and Al/Ti atoms at the cube corners [68] as shown in Figure 2.3. The volume fraction of γ′ in Haynes 282 (~19%) was optimized to achieve a unique combination of strength and processability that currently do not exist in any commercially available superalloy [5]. These γ′ particles are primarily precipitated by adding controlled amounts of Al and Ti to the rich Ni matrix. In addition, they may contain trace amounts of other alloying elements such as Cr, Fe, and Mo.

The ordered nature of the γ′ phase in superalloys has been confirmed by using atom probe experiments and it is believed that the phase remains ordered up to nearly its melting temperature of ~1375^{o}C which strongly depends on impurity concentration and the degree of stoichiometry [65]. The gamma-prime solvus is primarily controlled in most Ni-based superalloys by the Ti and Al content. Minor compositional variations from other alloying elements do not significantly affect the solvus temperature [69]. For Haynes, the γ′ solvus is 997^{o}C [5].

This item has been removed due to copyright issues. To view it, visit:

http://www.phase-trans.msm.cam.ac.uk/2003/Superalloys/superalloys.html

Figure 2.3: Unit cell of gamma-prime structure [70]

2.3.2.1 Gamma-prime (γ') Precipitation Kinetics in Haynes 282 Superalloy

Gamma-prime precipitation is a solid state diffusion process which is implemented by the nucleation of spherical nano-sized precipitates within the matrix and subsequent growth following the classical Ostwald ripening process which is controlled by the volume diffusion of solute atoms into the precipitate [71]. Controlled distribution, size, and morphology of these particles are critical for maintaining their strengthening effect at elevated temperatures. Precipitation hardening of alloy is accomplished by first heating the alloy to an elevated temperature and holding for an appropriate amount of time to dissolve a significant concentration of the solute elements into solid solution, which is a process called solutionizing. Solutionizing is done at temperatures above the γ' solvus in Ni-based superalloys. The solutionized alloy is then rapidly cooled to room temperature to trap the solute atoms in the solvent matrix, thus resulting in the formation of a thermodynamically metastable supersaturated solid solution. The amount of cooling depends on the precipitation kinetics of the alloy. The supersaturated solid solution is reheated to an intermediate (aging) temperature below the γ' solvus and held at this temperature for a sufficient amount of time to allow for the precipitation of nano-sized fine particles that are uniformly distributed within the matrix.

During aging, clusters of the solute atoms are formed in the matrix lattice. These solute-rich regions form the embryonic sites for nucleation to occur. As nucleation proceeds, more solute atoms diffuse to the clusters to form a new phase [72]. The driving force for the precipitation reaction is provided by lowering the surface and strain energy of the second phase to minimize the free energy of the system. For Ni-based superalloys, this requirement favors the formation of spherical precipitates that are coherent with the matrix. The aging temperature has a more profound influence than the aging time on the mechanical behaviour of a precipitation-hardened alloy. If an

alloy is aged at a lower than normal temperature, the second phase precipitation is retarded, which results in an alloy with reduced strength in higher temperature applications. In this case, the alloy is said to be underaged. However, an intermediate heat treatment temperature that is too high leads to the coarsening of the precipitates so that they are larger than the optimal size that again leads to a decline in the mechanical strength of the ensuing component. In this case, the alloy is said to be overaged. Similar, but less drastic, effect results when the holding time is varied during aging. An optimal aging temperature and time for any alloy should be carefully chosen to allow treatment at high-temperatures to strengthen the alloy through precipitate shearing or Orowan looping of dislocations. In general, higher aging temperatures are preferred to enhance creep and stress rupture strength, while lower aging temperatures are used for applications that require fatigue resistance and strength in elevated temperature environments [72]. A similar effect with temperature versus holding time has been reported for solution treatments. In a study on the influence of heat treatment on γ′ precipitation kinetics in Udimet 720, Monajati et al. [73] observed that some of the γ′ precipitates cannot dissolve after a solution treatment is carried out at 1110 ^{o}C for 24 hours. By increasing the solutionized temperature to 1150^{o}C, complete dissolution of the precipitates resulted after 10 minutes. This shows that the solutionized temperature rather than the holding time is the most effective parameter for the dissolution of the γ′ precipitates.

For Haynes 282, full solution heat treatments have been done for a temperature range of 1120 ^{o}C to 1149^{o}C for 2 hours to dissolve the γ′ precipitates and secondary carbide phases, usually $M_{23}C_6$ carbides [5], [10]. The solutionized alloy is air-cooled, which is adequate due to the sluggish precipitation kinetics of γ′ in the alloy. It has also been observed that no γ′ precipitates form in the grain interior after cooling [10]. Although the solutionized treatment is done at a temperature higher than the solvus temperature of $M_{23}C_6$ carbides, Cr-rich $M_{23}C_6$ carbides with a discontinuous

grain boundary [10], and large blocky Ti-rich MC carbides [5] and carbonitrides [10], [74] have been observed in the microstructure after solution treatment. These are attributed to an incomplete solution treatment or re-precipitation of these carbide phases upon cooling [10]. The presence of partially dissolved carbides after solutionized can limit the precipitation of the γ′ particles in subsequent aging treatments due to the possible volume diffusion of the Al/Ti atoms into the carbides [73].

The solution treatment is followed by a recommended two-step aging heat treatment at 1010^{o}C for 2 hours and air cooled, and then at 788^{o}C for 8 hours and air-cooled. The temperature of 1010^{o}C, in the first step, is higher than the γ′ solvus temperature of 997^{o}C but ensures the discrete formation of $M_{23}C_6$ carbides at the grain boundaries for improved creep resistance and ductility at high temperatures [5]. A temperature of 788^{o}C in the second step provides a uniform distribution of approximately 19% volume fraction of spherical γ′ precipitates in the Ni-matrix, typically with an average diameter of 20 nm [75].

2.3.3 Carbide Phases

Carbides are preferentially precipitated along the grain boundaries to stabilize the microstructure against deformation at higher temperatures [55]. They are found in the form of MC, $M_{23}C_6$, M_7C_3, and M_6C in most Ni-based superalloys depending on the C content, other alloying elements in the alloy, and the processing conditions [67]. The M stands for metallic elements such as hafnium (Hf), Cr, Ti, Mo, and Ta [65]. They are known to have globular, script, and blocky morphologies [76]. Carbides form through the following reactions, where M' and M'' represent the matrix metals [68].

$$MC + \gamma \rightarrow M_{23}C_6 + \gamma'$$

$$MC + \gamma \rightarrow M_6C + \gamma'$$

$$M_6C + M' \rightarrow M_{23}C_6 + M''$$

MC carbides are primary carbides, with an FCC structure, and form as discrete particles that are heterogeneously distributed throughout the alloy during freezing (at a temperature below the solidification temperature). They form when C is combined with strong carbide formers such as Hf, Ta, Nb, and Ti, to form HfC, TaC, NbC, and TiC in order of decreasing stability [56], [65]. They tend to occupy intergranular or transgranular positions, with minimal to no orientation with the Ni-matrix [56]. In Haynes 282, MC carbides are found in the form of large blocky Mo- and Ti-rich carbides [5]. These carbides provide a good source of C for use during subsequent heat treatment and in-service conditions at higher temperatures where they degenerate slowly into more stable carbides such as $M_{23}C_6$ and M_6C [77], [78]. The addition of Nb and Ta in some of the superalloys is believed to counter this decomposition reaction at temperatures up to 1260^{o}C [56].

$M_{23}C_6$ carbides have a complex cubic structure that readily form in alloys with higher Cr content, such as Haynes 282, at temperatures between 760^{o}C – 980^{o}C during the decomposition of MC carbides and from the soluble C residual in the matrix. They usually occur as discontinuous grain boundary carbides [10] which enhance the ductility, rupture strength, and creep resistance of the alloy by inhibiting grain boundary sliding. However, rupture failure can result from the fracturing of these carbides or through the decohesion of the carbide interface which usually occurs when the carbide is precipitated into a cellular structure [56]. $M_{23}C_6$ precipitation is the major carbide reaction in most superalloys. $M_{23}C_6$ carbides have been found in Haynes 282 in the aged condition [51]–[53].

M_6C carbides form at higher temperatures than $M_{23}C_6$, typically between 815°C – 980°C. They have a complex cubic structure similar to that of $M_{23}C_6$ but are preferentially formed along the grain boundaries in alloys with higher W and/or Mo content [56]. Their composition varies from M_3C to $M_{13}C$ depending on the matrix content of the alloy [78]. M_6C carbides are more beneficial than $M_{23}C_6$ carbides in controlling the grain size of wrought alloys due to their higher stability at elevated temperatures [56].

2.3.4 Minor Phases

In addition to the γ, γ′, and carbide phases, a Mo-rich boride phase (M_5B_3) was reported by Osoba et al. [79] that precipitates intergranularly as submicron particles in Haynes 282. Mo-rich borides in the M_3B_2 form was observed during the transient liquid phase bonding of the alloy [80]. Borides segregate to the grain boundaries as hard refractory particles with varying morphologies from blocky to half-moon in appearance [56]. These borides, which are believed to delay the onset of grain boundary tearing during creep deformation [56], are found to cause grain boundary liquation cracking in the heat affected zone of the alloy [79]. The TiN particles, σ phase, and carbosulfides of the Ti- and Mo-rich borides in the M_2SC form have been identified in the as-cast condition [81]. Deleterious TCP phases, such as sigma, Laves, and mu are not found in the wrought alloy [82].

2.3.5 Strengthening Mechanism in Ni-based Superalloy

The strength of Haynes 282, a Ni-based superalloy, is attributed to the solid solution strengthening of the matrix with the addition of alloying elements, grain boundary strengthening from carbide formation and precipitation hardening by the γ′ phase, with the latter providing most of the strength at elevated temperatures. The FCC Ni matrix has a high solubility for many alloying elements

because of its electronic structure. The mechanism for strengthening the gamma matrix involves changes in the lattice parameter, modulus of elasticity, stacking fault energy (SFE), and to some extent, short-range ordering from the alloying elements [83]–[85]. Ni has a high SFE and its reduction by solute atoms in the matrix increases the resistance to dislocation motion by cross-slipping [85]. Solid solution strengthening is attributed to the lattice distortion effect between the matrix atoms and solute atoms. This strengthening effect increases as the atomic radii difference between the matrix atoms and the solute atoms is increased up to about 10%. High melting point elements, such as Mo, provide strong lattice cohesion and reduced diffusion rate at high temperatures which contribute to improving the strength [86].

The contribution of γ′ precipitates to the excellent thermal stability of Haynes 282, which depends on their morphology and volume fraction [87], is reviewed with the aim to provide a better understanding of the mechanisms behind the γ-γ′ dislocation interactions during order strengthening and coherency hardening in Ni-based superalloys.

2.3.5.1 Order Strengthening

The spherical coherent γ′ precipitates in Haynes 282 have a cubic lattice structure with similar lattice parameters as the FCC γ phase. γ′ is an atomically ordered phase which hinders the motion of dislocations and strengthens the material. In a disordered FCC γ matrix, the Burgers vector of a dislocation is a/2 <110>. Since this is a lattice vector, slip does not change the crystal structure of the γ matrix. In contrast, a/2 <110> is not a lattice vector in γ′ [70]. The Burgers vector of a dislocation in γ′ is a <110> as illustrated in Figure 2.4. Notwithstanding the coherency of the γ′ phase with the γ matrix, glide dislocation (a/2 <110>) from the γ matrix into γ′ disrupts the order which creates an antiphase boundary (APB) across the slip plane of the precipitate [88], [89]. As

the APB energy increases, more force is required to shear the precipitate. A second dislocation (a/2 <110>) on the same γ′ slip plane is needed to restore the order. This requires superlattice dislocations, which are dislocation pairs, from the γ matrix to the γ′ phase to restore the ordered γ′ structure by removing the APBs created after each shearing process as shown in Figure 2.5. This requirement for paired dislocation makes it difficult for dislocations to shear the precipitates; thus, strengthening the alloy. It should be noted that the order-hardening behavior is reduced with an increase in precipitate size as dislocation by-pass or Orowan looping becomes easier than precipitate shearing. Order hardening is thought to have the highest contribution to the strength of most Ni-based superalloys at room temperature [65], [90].

Figure 2.4: Lattice vectors along <110> direction and lying on {111} plane in: (a) face cubic lattice of γ and (b) primitive cubic lattice of γ′ [70].

This item has been removed due to copyright issues. To view it, visit:

J. C. Lippold, S. D. Kiser, and J. N. DuPont, *Welding metallurgy and weldability of nickel-base alloys*. John Wiley & Sons, 2011, page 164.

Figure 2.5: Transmission electron micrograph of Ni-based superalloy that shows: (a) paired superlattice dislocations and (b) dislocation shearing of γ′ precipitates. Image reproduced from [88], original image from [91].

2.3.5.2 Coherency Strain Strengthening

The mechanical properties of Ni-based superalloys depend on the coherency effect between the γ and γ′ phases, which are represented as lattice misfit, δ, and can be negative or positive depending on the temperature and composition of the alloy [92], [93]. Coherency is the enforced alignment in the crystallographic structure and lattice spacing between the γ and γ′ phases. During nucleation and growth, the precipitate size and morphology evolve to minimize the surface and strain energies of the system. Haynes 282 has a small degree of lattice mismatch between the lattice structures of the γ and γ′ and hence a low strain energy. This favors the formation of spherical precipitates that minimize the surface energy of the lattice. The lattice mismatch causes elastic strain around the precipitates. As dislocations move through the matrix along the slip planes, they encounter the strain field, which impedes their movement [94]. Dislocations pile up against this strain field barrier and strengthen the alloy by restricting further plastic deformation. For plastic flow to continue, the dislocation must climb around the barrier to continue along the most easily available slip plane [95].

Lippold et al. [88] concluded that a smaller lattice misfit provides a favorable microstructure for applications at higher temperatures, whilst a larger lattice misfit increases the rate of coarsening of the γ′ phase in service, an undesirable phenomenon that reduces the mechanical strength and rupture life of the material. As the particles coarsen, coherency strains from the precipitates increase which is then released when the precipitates become incoherent. The loss of coherency changes the interaction process between dislocations and particles from precipitate cutting to dislocation bypassing, which results in Orowan strengthening [96].

2.4 Deformation Mechanics at High Strain Rates

The dynamic behaviour of materials subjected to high strain rate loading is a complex phenomenon [97]. The influence of the strain rate on the deformation behaviour of materials is characterized by different deformation mechanisms as the loading rate is increased from low (10^{-3}/s) to ultra-high strains (10^{6}/s). These deformation mechanisms are grouped into three regimes: athermal flow, thermally dependent flow and phonon drag [98]. Athermal flow is found with low strain rates in which a non-rate dependent flow governs the deformation mechanism. In this phase, the material shows less sensitivity to flow stress and Oosterkamp et al. [98] stated that thermal vibrations of the lattice atoms provide less energy than required to overcome a wide range of deformation barriers. At higher strain rates (10^{2}/s), the flow stress of materials that are sensitive to thermally dependent flow show a linear dependence on the strain rate. In this phase, thermal vibrations of the lattice atoms provide sufficient energy to overcome dislocations; hence, the sensitivity of the flow stress to the strain rate is observed [98]. At ultra-high strain rates, phonon drag is reported, a condition in which the flow stress shows a linear dependence with the strain rate [98]. The flow of the material at these strain rates becomes viscous [99], which is likely due to the saturation of mobile dislocations at an average dislocation velocity [98].

For most alloys, the strain rate hardening effect has been reported during dynamic impact deformation due to rapid and dislocation increase and pile up [100]. The dislocation pile up and entanglement increases the deformation flow stress levels by restricting further movement of the dislocation in the matrix during deformation [101]. However, at very high strain rates, the dislocation density may increase so much that the dislocations begin to annihilate which results in a strain rate softening effect [100]. Moreover, very high strain rates lead to increased adiabatic

heating with a subsequent increase in dislocation motion [100]. The dynamic behaviour of alloys at high strain rates is then studied by using the split Hopkinson pressure bar (SHPB), or any of its variants.

2.4.1 Split Hopkinson Pressure Bar

When an alloy experiences a sudden load, the deformation and stresses do not propagate immediately throughout the material. There are disturbed and undisturbed parts due to the local excitation of the material. As time progresses, the deformation and stresses travel through the material from the point of the load with a finite velocity that is characteristic of the transmitting medium. High strain rate studies that have applied the conventional SHPB have normally assumed uniaxial elastic wave propagation during impact deformation. This means that they have neglected the effects of transverse strain, lateral inertia, body forces, and internal friction. However, the assumption of uniaxial elastic wave propagation is still valid for situations where the wavelength of the stress pulse is at least 6 - 10 times more than that of the cross-sectional area of the bar [102], [103].

First proposed by Bertram Hopkinson in 1914 [104], the SHPB test or Kolsky bar method is among the most widely used test methods in high strain rate studies ($10^3 – 10^4$ s^{-1}). In his pioneering work [104], Hopkinson examined the dynamic response behaviour of steel and measured the pressure generated under impulsive loading by using induced wave propagation in a long elastic metallic bar. In his study, momentum traps of varying lengths were used to analyze the shape and evolution of stress pulses as a function of time. This was modified by Kolsky in 1949 [105] who used two Hopkinson pressure bars in series and a sample placed in-between the bars to determine the dynamic flow behaviour of soft materials, including rubber, plastic, and metal. The experimental

configuration that incorporated the modifications of Kolsky became known as the "split-Hopkinson" pressure bar or less commonly, the Kolsky bar. Several versions of this testing apparatus have been developed to study materials in tension, torsion, or compression-torsion. The basic assumptions upon which an SHPB experiment relies include (a) one-dimensional stress wave propagation in the bar, (b) axially homogeneous state of stress and strain in the sample, and (c) negligibility of the radial, inertial, and frictional effects [106].

The SHPB setup, which is shown in Figure 2.6, consists of four major mechanical components: two strong elastic bars called the incident and transmitter pressure bars, a pressure control system, and a striker bar. The striker bar, incident, and transmitter pressure bars are made of the same material and only elastic deformation along the bars is assumed throughout the test. A sample is sandwiched in-between the incident and transmitter pressure bars. The striker bar is fired by using a gas gun to strike the incident bar thus generating a constant compressive stress pulse in both bars. This compressive stress pulse travels along the incident bar and upon reaching the incident bar – the sample boundaries, some of the incident stress pulses is reflected back as a tension wave into the input bar and some of the incident stress pulse is transmitted as a compressive wave through the sample into the output bar. A strain gauge is attached on the center of the bars to capture the voltage-time history at the bar ends that is used to determine the dynamic stresses and strains that occur in the sample under the prevailing strain rate.

The ratio of the reflected-transmitted stress waves is affected by the acoustic impedance mismatch between the bars and sample. If the physical properties of a medium that transmits a passing pulse change suddenly, the disturbance will also change as it crosses the boundary between the two materials. A fraction of the pulse will be transmitted, and the remainder is reflected. To understand the behaviour of a pulse as it crosses the interface between two dissimilar materials with different

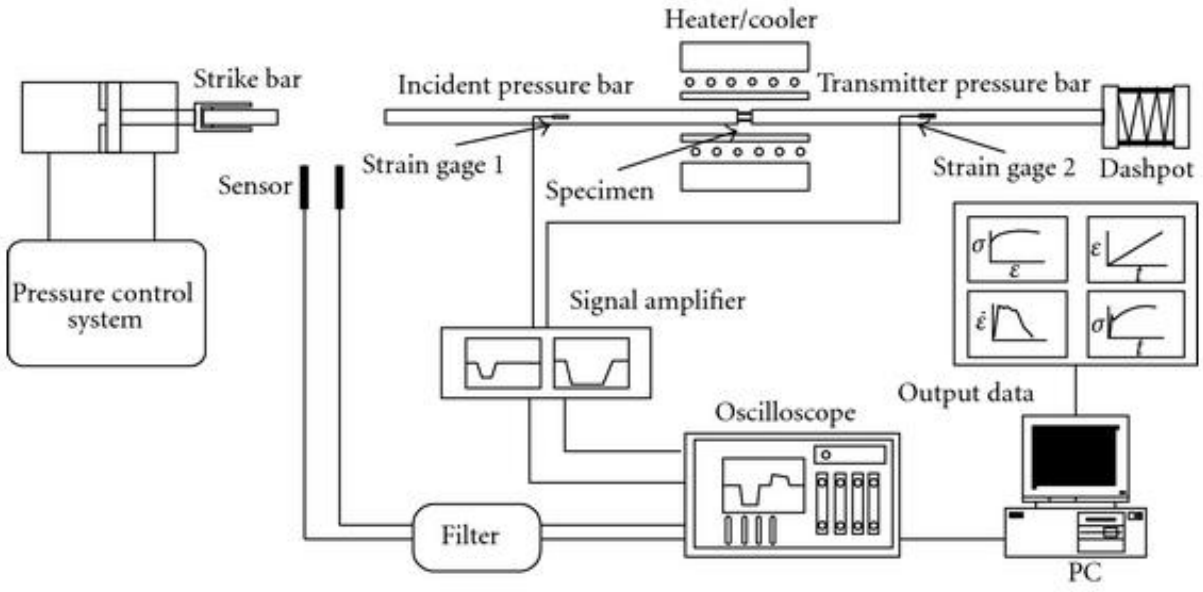

Figure 2.6: A schematic diagram of a compressive split Hopkinson pressure bar system [107]

cross-sectional areas, there are two boundary conditions that must be satisfied at the interface [108]. The two conditions are that:

1. the stresses on the two sides of the interface are equal, and
2. the particle velocities normal to the boundaries are equal.

The first boundary condition is derived from the fundamental law of hydrostatic pressure and valid for solids only when normal incident waves are considered. The second boundary condition implies that the two materials remain in constant contact at the interface. These boundary conditions must hold for every point on the incident wave. Mathematically, these conditions can be represented as:

$$A_1(\sigma_I + \sigma_{R)} = A_2\sigma_T \qquad (2.1)$$

$$U_I - U_R = U_T \qquad (2.2)$$

where A_1 and A_2 are the cross-sectional areas of the two mediums, $\sigma_I, \sigma_R,$ and $\sigma_T,$ are the instantaneous values of stress for the incident, reflected and transmitted pulses respectively, $U_I, U_R,$ and U_T are the particle velocity for the incident, reflected, and transmitted pulses, respectively, as shown in Figure 2.7.

Using the expression $\sigma = \rho cv,$ where σ is the bar density, v is the particle velocity, and c is the velocity of the propagation of the wave disturbance [97] gives:

$$U_I = \frac{\sigma_I}{\rho_1 c_I} \; ; \; U_R = \frac{-\sigma_R}{\rho_1 c_I} \; ; \; U_T = \frac{\sigma_T}{\rho_2 c_2} \qquad (2.3)$$

Subscripts 1 and 2 are used to denote the first and second mediums. Substituting Equation (2.3) into Equation (2.2) gives:

$$\frac{\sigma_I}{\rho_I c_I} - \frac{\sigma_R}{\rho_I c_I} = \frac{\sigma_T}{\rho_2 c_2} \qquad (2.4)$$

Solving Equations (2.1) and (2.4) simultaneously, for σ_T in terms of σ_I, and then σ_R in terms of σ_I, Asada [108] obtained two fundamental equations that govern the distribution of stress at the interface of different materials, as follows:

$$\sigma_T = \frac{2A_1\rho_2 c_2}{A_1\rho_2 c_2 + A_2\rho_I c_I}\,\sigma_I \qquad (2.5)$$

$$\sigma_R = \frac{A_2\rho_2 c_2 - A_1\rho_I c_I}{A_1\rho_2 c_2 + A_2\rho_I c_I}\,\sigma_I \qquad (2.6)$$

Equations (2.5) and (2.6) provide an understanding of how an incident stress pulse during impact is modified when there is an abrupt change in the material properties at an interface. The ratio of the reflected stress and the transmitted stress σ_R/σ_T yields:

$$\frac{\sigma_R}{\sigma_T} = \frac{A_2\rho_2 c_2 - A_1\rho_I c_I}{2A_1\rho_2 c_2} \qquad (2.7)$$

The implications of Equation (2.7) are as follows:

1. If $\rho_2 c_2$ is approximately equal to $\rho_1 c_1$, then almost all of the incident stress wave is transmitted [108].
2. If $\rho_2 c_2$ differs greatly from $\rho_1 c_1$, then almost the entire incident stress wave is reflected at the interface of the two mediums [108].
3. If $A_2 < A_1$, as obtained in the SHPB tests, the incident and reflected waves will have opposite signs. In impact tests, the errors due to friction, longitudinal and radial inertia can

be reduced by minimizing the areal mismatch between the bar (A_1) and the sample (A_2) [109].

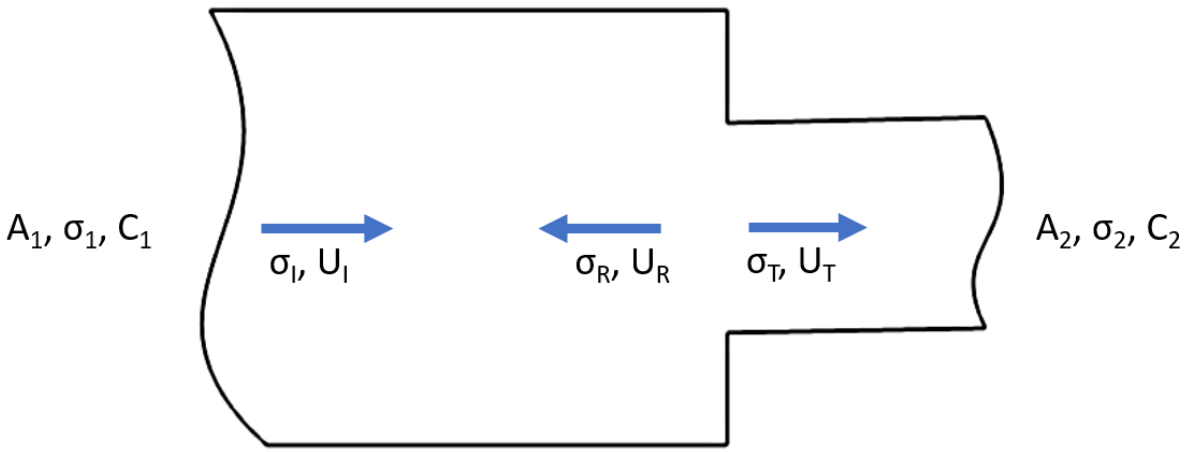

Figure 2.7: Interface boundary conditions

2.5 Material Constitutive Equation for Numerical Simulation

An understanding of the high strain rate behaviour of engineering materials over a wide range of temperatures is important in military applications, high-speed machining, high-velocity impact situations, blade containment systems in jet engines, and any other event that exposes a material to strain rates greater than 10^3 s^{-1}. However, implementing experimental tests to characterize the dynamic impact response of a material are expensive and time-consuming. Hence, considerable efforts have been devoted to developing constitutive models that can accurately predict the plastic flow behaviour of materials for numerically simulating impact events and optimizing machining operations. Constitutive models use experimentally obtained data for strain, strain rate, and deformation temperature of the material to represent its dynamic impact behaviour. An ideal constitutive equation should accurately predict the dynamic behaviour of a material over a wide range of deformation conditions with a reasonable number of material constants. Such models are in high demand by designers for numerically simulating the thermo-mechanical response of a material under impact loading conditions. There are three types of constitutive models: phenomenological, physical-based, and artificial neural network. Here, only the most commonly used models, the phenomenological and physical-based constitutive models will be discussed.

2.5.1 Phenomenological Constitutive Models

Phenomenological constitutive models are extensively used to simulate metal forming processes in high strain rate conditions. These empirical models can be represented as a function of the deformation temperature, strain rate, and strain to predict the effect of the processing parameters on the dynamic flow response of a material. Some of the more widely applied phenomenological models include the Johnson-Cook (JC), Voce-Kocks, Khan-Huang, and Arrhenius-type models

[19], [110]–[113]. These macroscopic models rely on accurately fitting the experimental test data to describe the material behaviour. The fundamentals of the JC and Arrhenius-type models will be presented as follows, as they continue to be the most successfully used phenomenological models to date.

2.5.1.1 Johnson-Cook Material Model

The JC model, which was proposed in 1983 [110], remains the most widely used phenomenological model for describing the effect of deformation history (strain), strain rate, and temperature on the dynamic behaviour of a material. The JC model is popular due to its simplicity and a small number of material parameters that makes it well suited for numerical computation. The original JC model is expressed as:

$$\sigma = (A + B\varepsilon^{n})(1 + C\ln\dot{\varepsilon}^{*})(1 - T^{*m}) \qquad (2.8)$$

where σ is the flow stress, ε is the equivalent plastic strain, and $\dot{\varepsilon}^{*}$ is a dimensionless strain rate given as $\dot{\varepsilon}^{*} = \dot{\varepsilon}/\dot{\varepsilon}_0$. $\dot{\varepsilon}_0$ is the reference strain rate and A the material yield strength (at the reference temperature and strain rate). B is the coefficient of strain hardening, n represents the strain-hardening exponent, and m is the thermal softening exponent. The dimensionless parameter, C, is the coefficient of strain rate hardening. A, B, C, n, and m are the five material constants of the JC model required to describe the dynamic behaviour of a material. T^{*} is the homologous temperature expressed as:

$$T^{*} = \frac{T - T_r}{T_m - T_r} \qquad (2.9)$$

where T_m is the melting temperature of the material, T is the absolute test temperature, and T_r is the reference temperature. In Equation (2.8), the first set of brackets contains an expression that

gives the effect of strain as a function of stress. The expression in the second set of brackets represents the effect of the strain rate and those in the third set of brackets describe the dependence of the flow stress on temperature during deformation. These three expressions in the JC model are independent of each other and can be isolated [114]. The uncoupling of isotropic hardening, strain rate hardening and thermal softening oversimplifies the model and introduces some errors as these effects have been observed to be strongly dependent on each other during high strain rate tests [100]. Nevertheless, the JC model has attracted a significant amount of interest from scientists. Modified versions of the original JC model have been proposed by researchers, such as [100], [115]–[118] to account for the observed coupled effects of strain, strain rate hardening/softening and thermal softening during dynamic deformation.

2.5.1.2 Arrhenius-type Model

The Arrhenius-type model is one of the most successfully used phenomenological-based models to predict the flow behaviour of materials, especially at higher temperatures. The coupled effects of strain rate and deformation temperature can be represented by using a Zener-Hollomon parameter (Z) in the exponential form as:

$$Z = \dot{\varepsilon}\exp\left(\frac{Q}{RT}\right) \qquad (2.10)$$

$$\dot{\varepsilon} = AF(\sigma)\exp\left(-\frac{Q}{RT}\right) \qquad (2.11)$$

$$F(\sigma) = \begin{cases} \sigma^n & \alpha\sigma < 0.8 \\ \exp(\beta\sigma) & \alpha\sigma > 1.2 \\ [\sinh(\alpha\sigma)]^n & \text{for all } \sigma \end{cases} \qquad (2.12)$$

where $\dot{\varepsilon}$ is the deformation strain rate (s^{-1}), R is a universal gas constant (8.31 J mol^{-1} K^{-1}), T is the absolute deformation temperature (K) and Q represents the activation energy for hot deformation (KJ mol^{-1}). σ is the material flow stress (MPa). A, α and n are material constants, with $\alpha = \frac{\beta}{n}$. It has been shown that the hyperbolic law in the Arrhenius-type model gives a much better approximation between the Z parameter and the dynamic flow stress of the material [119]–[121]. As such, the relationship between the deformation flow stress, temperature, and strain rate can be represented at all stress levels by:

$$\dot{\varepsilon} = A[\sinh(\alpha\sigma)]^n \exp\left(-\frac{Q}{RT}\right) \qquad (2.13)$$

$$\sigma = \frac{1}{\alpha}\ln\left\{\left(\frac{Z}{A}\right)^{1/n} + \left[\left(\frac{Z}{A}\right)^{2/n} + 1\right]^{1/2}\right\} \qquad (2.14)$$

2.5.2 Physical-based Constitutive Models

The material constants for phenomenological based models are primarily obtained by accurately fitting the experimental data. This reliance on a mathematical expression on curve fitting introduces some errors into the model, as they cannot represent the microstructural evolution that occurs during deformation. Physical-based models, therefore, have been introduced to account for the internal microstructural changes that accompany and influence the behavior of a material during high strain rate tests. These models are considered to more accurately represent the deformation behaviour of a material; however, they are not always adopted by users as they have more material constants and require extensive data from precisely-controlled experiments [122]. Physical-based models include the Zerilli-Armstrong, dynamic recrystallization, mechanical threshold stress, and Bonder-Partom models, to name a few [123]–[129]. The Zerilli-Armstrong

model will be briefly discussed, as it is the most commonly used physical-based model in the literature.

2.5.2.1 Zerilli-Armstrong Model

In 1987, Zerilli and Armstrong [123] proposed a dislocation mechanics-based model which depends on the crystal structure of a material to describe the inter-dependence of strain, strain rate and temperature during deformation. Two separate models were proposed for FCC and body-centered cubic (BCC) crystal structures [130] by varying thermal activation mechanisms to overcome the obstacles to dislocation motion and the accompanying dislocation interaction during deformation. The Zerilli-Armstrong model can be represented as [131]:

$$\sigma = \begin{cases} C_0 + C_1\varepsilon^n[\mathrm{EXP}(-C_3T + C_4T\ln\dot{\varepsilon}^*)] + C_5\varepsilon^n & \text{For BCC materials} \\ C_0 + C_2\varepsilon^n[\mathrm{EXP}(-C_3T + C_4T\ln\dot{\varepsilon}^*)] & \text{For FCC materials} \end{cases} \quad (2.15)$$

where as in the JC model, σ, ε, T and $\dot{\varepsilon}^*$ denote the flow stress, equivalent plastic strain, absolute test temperature, and a dimensionless strain rate, respectively. C_o, C_1, C_2, C_3, C_4, C_5, and n are experimentally determined material constants.

CHAPTER 3

RESEARCH METHODOLOGY

3.1 Material

Wrought plates of Haynes 282 (610 mm x 10 mm x 11.5 mm) for this study were supplied by Haynes International Inc. in a bright-annealed form with a mill finish. The nominal chemical composition of Haynes 282 is listed in Table 2.4. The as-received samples underwent three distinct types of heat treatments: solutionized, standard heat treatment, and special aged, as shown in Table 3.1. The solutionized heat treatment was done to dissolve the main strengthening phase of Haynes 282 (γ'). The standard heat treatment denotes the manufacturer's recommended two-step age hardening heat treatment for Haynes 282 before it is placed in service [62]. The special aged heat treatment was developed in an unpublished internal report of an undergraduate work done by Lius Braga [132] at the University of Manitoba. After evaluation of several heat treatment schedules, it was observed by [132] that ageing at 900^{o}C for 1 hour, then furnace cooled gives the optimal mechanical properties for Haynes 282. Moreover, the special aged heat treatment was conceived in response to the increasing need for a one-step age hardening process, particularly for large power plant components, to remedy the difficulties associated with the two-step ageing process [9].

3.2 Sample Preparation for High Strain Rate Tests

To study the effect of heat treatment on the ballistic behaviour of Haynes 282, the as-received Haynes 282 was machined by using a water-jet that sliced the alloy into cylindrical compression samples with a diameter of 11.5 mm and height 11.5 mm, per the recommended aspect ratio of 0.5 – 1.0 to minimize errors from inertial and frictional effects [109], [133]. The tests were

conducted at an impact momentum that ranged from 27 – 47 $kg.ms^{-1}$ and temperatures that ranged from 25^{o}C – 800^{o}C. Each test was done thrice to ensure repeatability and accuracy.

Table 3.1: Heat treatment conditions used in this study

Heat Treatment	**Heat Treatment Procedure**
Standard heat treatment (B)	Solution treated at 1120^{o}C for 2 hours and air cooled, followed by carbide stabilization at 1010^{o}C for 2 hours and air cooled, and then recommend aging treatment at 788^{o}C for 8 hours and air cooled
Solutionized (C)	Solution treated at 1120^{o}C for 2 hours and air cooled
Special aged (D)	Aged at 900^{o}C for 1 hour, then furnace cooled

3.3 Experimental Set-up for High Strain Rate Tests

A direct impact Hopkinson pressure bar, which is a variant of the conventional split Hopkinson bar, was used to investigate the impact behaviour of Haynes 282 at strain rates that ranged from 2×10^3 to 9×10^3 s^{-1} and temperatures from 25ºC to 800ºC. A schematic of the test apparatus is shown in Figure 3.1, which consists of a pneumatic firing chamber, a transmitter bar, projectile, furnace, data acquisition system, and other ancillary components. The projectile is made from a 4340 steel bar with a length of 0.2 m, diameter of 3.8 cm, and weight of 1.1 kg. The transmitter bar has a length of 1.5 m and a diameter of 3.8 cm and is made of 4340 steel that was heat-treated to achieve a Rockwell hardness value between 45 – 50 HRC [134]. The sample was held in contact with the transmitter bar by using a sample holder and the projectile was fired by using a light gas gun at a set pressure. The impact momentum was varied by adjusting the firing pressure.

Excessive friction, radial, and longitudinal inertia at the sample/bar boundaries can cause deviation from the uniaxial state of stress that is necessary for accuracy in the test measurement. Deviation from uniaxial stress state constrains the lateral flow of a material, thus giving rise to a complex triaxial state of stress which over-estimates the true flow stress of a material [135]. To minimize these inertial and frictional effects, a sample size with an aspect ratio between 0.5 and 1.0 (length-to-diameter) was used to reduce the areal mismatch between the sample and the bar diameter [109], [133], [136]. In addition, the polished contacting surfaces of the projectile, transmitter bar, and sample were lubricated by using molybdenum disulphide for tests at room temperature and super enhanced graphite lubricant for tests carried out at higher temperatures to reduce frictional effects. For tests carried out at higher temperatures, the lubricated samples were heated inside a furnace

for 10 minutes to homogenize the temperature. After heating, the sample was quickly taken out from the furnace at an average time of 1 to 4 seconds and the projectile was immediately fired to ensure that the compensated temperature drop in the sample remained less than 10^{o}C. The average duration of the impact is between 50 – 200 microseconds depending on the momentum of the impact. The dynamic impact response of the deformed sample was obtained by recording the stress wave that was propagating through the transmitter bar with the use of strain gauges that were attached to the center of the transmitter bar. The elastic stress pulse recorded by the strain gauges was stored in an oscilloscope as voltage-time history data.

Based on the assumption that the elastic wave propagation is one-dimensional, the true stress and true strain in the sample were calculated using [137]:

$$\varepsilon_t = \ln \frac{l(t)}{l_o} \qquad (3.1)$$

where l_o is the original sample length and $l(t)$ gives the variation in the instantaneous length during deformation. The instantaneous length is obtained directly from the time-dependent force, $f(t)$ as [133], [138]:

$$l(t) = l_o - v_o t + \frac{2}{ZA}\int_0^t f(t')dt' \qquad (3.2)$$

where v_o is the velocity of the impact, Z is the bar impedance, and A is the cross-sectional area of the bar.

The corresponding true stress, σ is derived from [139] as:

$$\sigma = \sigma_t - \sigma_r \qquad (3.3)$$

where σ_t gives the flow stress obtained experimentally by using the relation:

$$\sigma_t = \frac{F(t)}{A(t)} \qquad (3.4)$$

$F(t)$ is the time-dependent loading pulse and A is the instantaneous cross-sectional area of the sample during deformation.

The radial stress, σ_r, which was derived from the inertial effect, was estimated by using [139]:

$$\sigma_r = \frac{3\rho}{8}\left(\frac{a_0}{l_0}\right)^2 \frac{v_0}{(1-\epsilon(t))^3} \qquad (3.5)$$

where a_0 is the radius of the original sample, ρ is the density of the transmitter bar, and $\epsilon(t)$ is the nominal strain.

3.4 Quasi-Static Compression Test

The quasi-static behaviour of Haynes 282 was tested in compression at room temperature with a hydraulic testing machine having a maximum load bearing capacity of 600 KN under the three heat treatment conditions: solutionized, standard heat treatment, and special aged. For ease of comparison with the dynamic impact behaviour, cylindrical samples with a diameter of 11.5 mm and a height of 11.5 mm were used in the compression tests. The samples were lubricated with molybdenum disulphide to minimize barreling from frictional effects [140]. The tests were carried out at loading rates of 5, 25, and 100 mm/min. Each test was repeated twice for accuracy of the data generated.

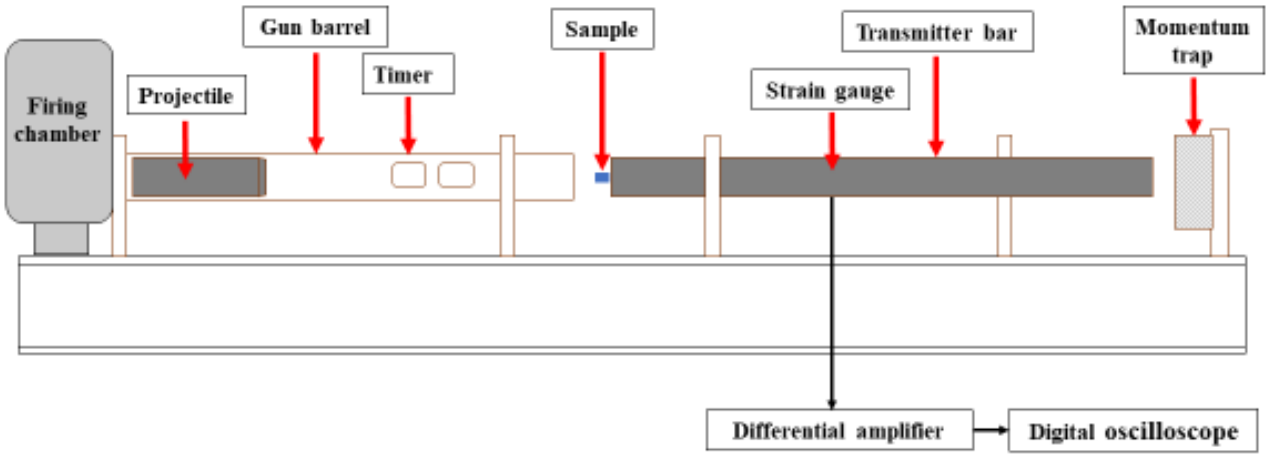

Figure 3.1: Schematic diagram of direct impact Hopkinson bar at the University of Manitoba [137]

Adapted by permission from the Springer Nature Customer Service Centre GmbH: Asala, G., J. Andersson, and O. A. Ojo. "Microstructure Dependence of Dynamic Impact Behaviour of ATI 718plus® Superalloy." Proceedings of the 9th International Symposium on Superalloy 718 & Derivatives: Energy, Aerospace, and Industrial Applications. Springer, Cham, 2018.

3.5 Quasi-static Tension Test

Tensile testing of Haynes 282 under the three heat treatment conditions were done at room temperature by using a servo hydraulic testing system, MTS 647, which is equipped with an extensometer. Sub-size tensile samples were used based on ASTM standard E8/E8M for tension testing of metallic materials [141]. The samples were polished until smooth to eliminate areas of stress concentration that could affect the result. Each type of heat treatment was tested twice at a loading rate of 5 mm/min to ensure repeatability and accuracy. The fracture morphology of the sample was examined with a scanning electron microscope.

3.6 Optical and Scanning Electron Microscopies

The as received and heat-treated samples were prepared for optical and scanning electron microscopies by using standard metallographic techniques. After polishing with a 6-micron colloidal suspension solution, the samples were electropolished in a solution of 20% sulfuric acid and 80% methanol at 25 DC volts for 20 seconds and ultrasonically cleaned in fresh acetone. The surface of the electropolished sample was released from the flow layer to reveal the inert carbides in the alloy. The aged samples were then etched at 5 volts for 5 seconds in a solution of 12 ml of phosphoric acid (H_3PO_4), 40 ml of nitric acid (HNO_3), and 48 ml of sulfuric acid (H_2SO_4) to reveal the γ' precipitates.

An optical microscopy of the microstructure was done by using a ZEISS inverted-reflected light microscope equipped with a CLEMEX vision 3.0-image analyzer. SEM was conducted by using a JEOL 5900 scanning electron microscope with an Oxford ultra-thin window energy dispersive spectrometer. SEM analysis of the nano-sized γ' particles was further carried out by using an FEI Nova NanoSEM 450 equipped with a high-resolution field emission gun.

Grain size measurement was done by using the linear intercept method in accordance with ASTM standard E112-13 [142]. The carbides in the alloy were identified by using an SEM-EDS analysis. Estimation of the average γ′ precipitate size in aged condition was done by using ImageJ, a public domain image processing software [143].

3.7 Hardness Measurement

The Vickers hardness value of the as received and heat-treated samples before deformation was obtained by using a Buehler MicroMet 5104 microindentation hardness tester that was operated at a test load of 300gf. The average of 10 measurements for each sample is reported in this study. Where applicable, the Vickers hardness value was converted into the Rockwell scale by using ASTM standard E140-12be1 [144].

CHAPTER 4

RESULTS AND DISCUSSION

4.1 Microstructural Analysis of Haynes 282

The optical and scanning electron microscopy micrographs of Haynes 282 in the as-received form, and after solutionizing, standard, and special aged heat treatments are discussed below to provide a better understanding of the main phases that are found in each condition.

4.1.1 Microstructure of As-received Haynes 282

Haynes International Inc. supplied the Haynes 282 superalloy for this study as a wrought plate in the bright-annealed form, with a mill finish. Figure 4.1 shows the optical microscopy micrograph of the as-received material. The microstructure, with an average grain size of ~90 μm, contains Ti- and Mo-rich MC-type and Mo-rich M_6C-type primary carbides, and carbonitrides inside the grains and sparsely along the grain boundaries. This is consistent with the microstructures reported in [74] and [137]. These primary carbides have an average size of ~4 μm. The FEI Nova NanoSEM 450 could not detect the presence of γ′ precipitates; however, very fine cooling γ′ precipitates was reported in [82] in the mill-annealed condition by using high magnification in-lens SEM imaging. The γ′ precipitates in the mill-annealed condition was attributed to the difficulty in suppressing γ′ precipitation on a mill-scale [9], [82]. The as-received Haynes 282 used in this study has an average Vickers hardness of 209 HV ±8. This hardness value correlates with those reported in [9], [55], and [138].

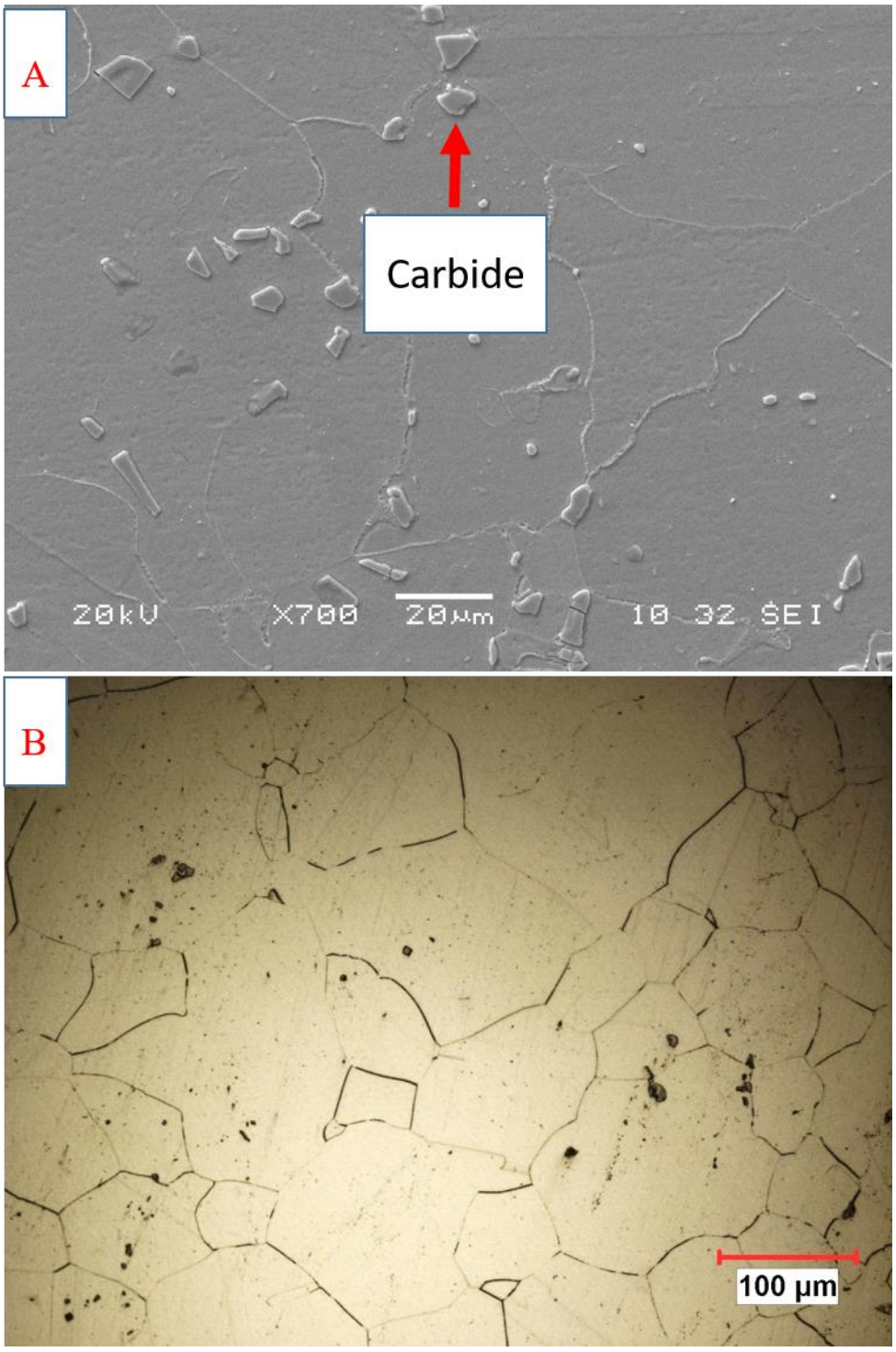

Figure 4.1: (a) SEM and (b) optical microscopy micrographs of as-received Haynes 282 that shows primary carbide particles distributed in the matrix and along grain boundaries

4.1.2 Microstructure of Solutionized Haynes 282

The microstructure of Haynes 282 after solutionized heat treatment at 1120^{o}C is shown in Figure 4.2. The microstructure, which has an average grain size of ~100 μm, consists of the γ matrix, and primarily MC-type (Mo- and Ti-rich), and M_6C-type (Mo-rich) carbides distributed inside the grains and rarely along the grain boundaries. The carbides have an average size of ~4 μm. The precipitation of secondary Cr-rich $M_{23}C_6$ carbides is highly suppressed since the solutionizing temperature of 1120^{o}C is above the solvus temperature of the $M_{23}C_6$ carbides. The $M_{23}C_6$ carbides could be present in the alloy after solutionizing due to incomplete solution treatment or carbide re-precipitation during cooling [10]. Similar to Haynes 282 in the as-received condition, the FEI Nova NanoSEM 450 could not detect the γ′ phase after solutionized heat treatment. The soft and ductile material that emerged after solutionizing has an average Vickers hardness value of 229 HV ± 15.

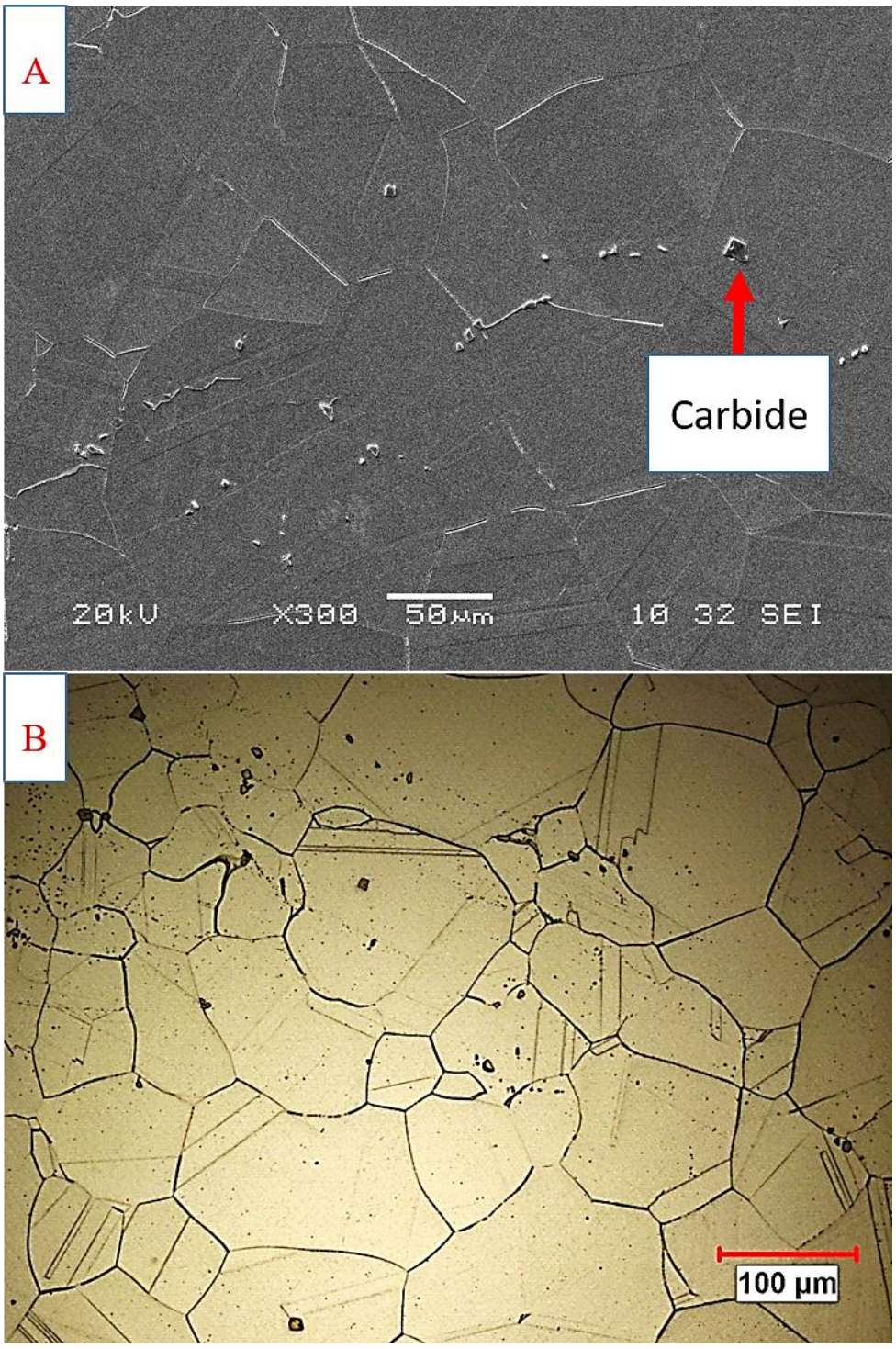

Figure 4.2: (a) SEM and (b) optical microscopy micrographs of Haynes 282 after solutionizing which show undissolved primary carbide particles in the matrix and sparsely along grain boundaries

4.1.3 Microstructure of Standard Aged Haynes 282

Figure 4.3 shows an optical microscopy micrograph of Haynes 282 after undergoing the recommended aging heat treatment [62]. The microstructure reveals that the grains have coarsened, with an average grain size of ~143 μm. Primary Ti- and Mo-rich MC-type and Mo-rich M_6C-type carbides can be seen inside the grains and along the grain boundaries, typically in the order of 2 to 10 μm. These primary carbides are usually formed during the solidification of Haynes 282 [29]. The carbide stabilization treatment at 1010^oC resulted in the precipitation of secondary Cr-rich $M_{23}C_6$ carbides. MC-type carbides are known to be thermodynamically metastable in high or service temperatures and tend to decay into more stable phases such as $M_{23}C_6$ and M_6C carbides [77].

The main strengthening phase of Haynes 282, the γ′ precipitate phase, is uniformly distributed in the matrix with an average spherical particle diameter that ranges from 15 – 30 nm as shown in Figure 4.4. The precipitates are mono-modal with an estimated volume fraction of 19% [9]. The low volume fraction of γ′ precipitates in the alloy was optimized during development to provide a unique combination of strength and ease of fabricability [5]. The microhardness value of Haynes 282 after the standard heat treatment is 349 HV ±6, which is equivalent to 37 HRC on the Rockwell hardness scale. This value is in agreement with those reported in [62].

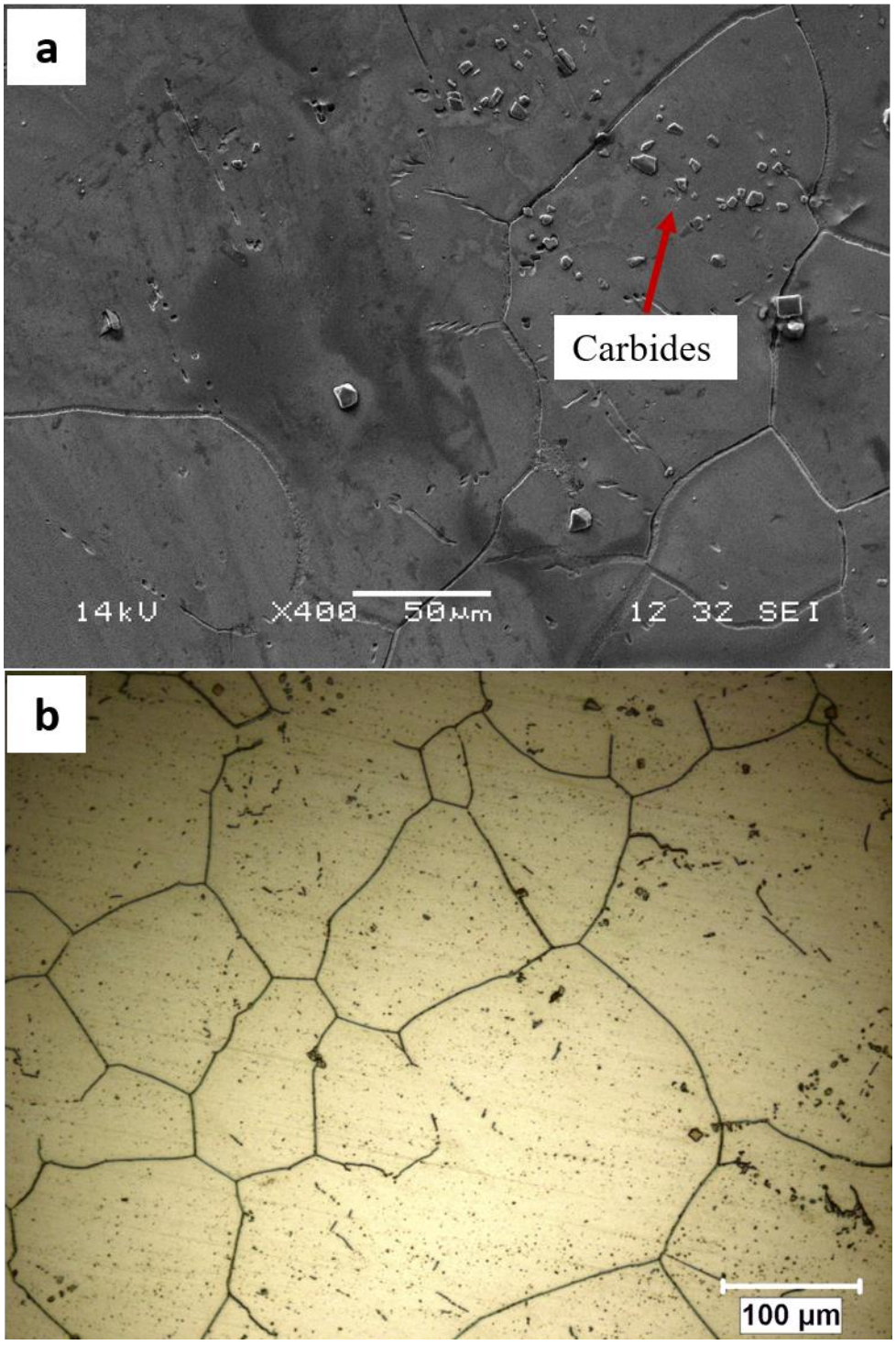

Figure 4.3: (a) SEM and (b) Optical microscopy micrographs of Haynes 282 in standard heat treatment which show carbide particles distributed along the grain boundaries and in the matrix

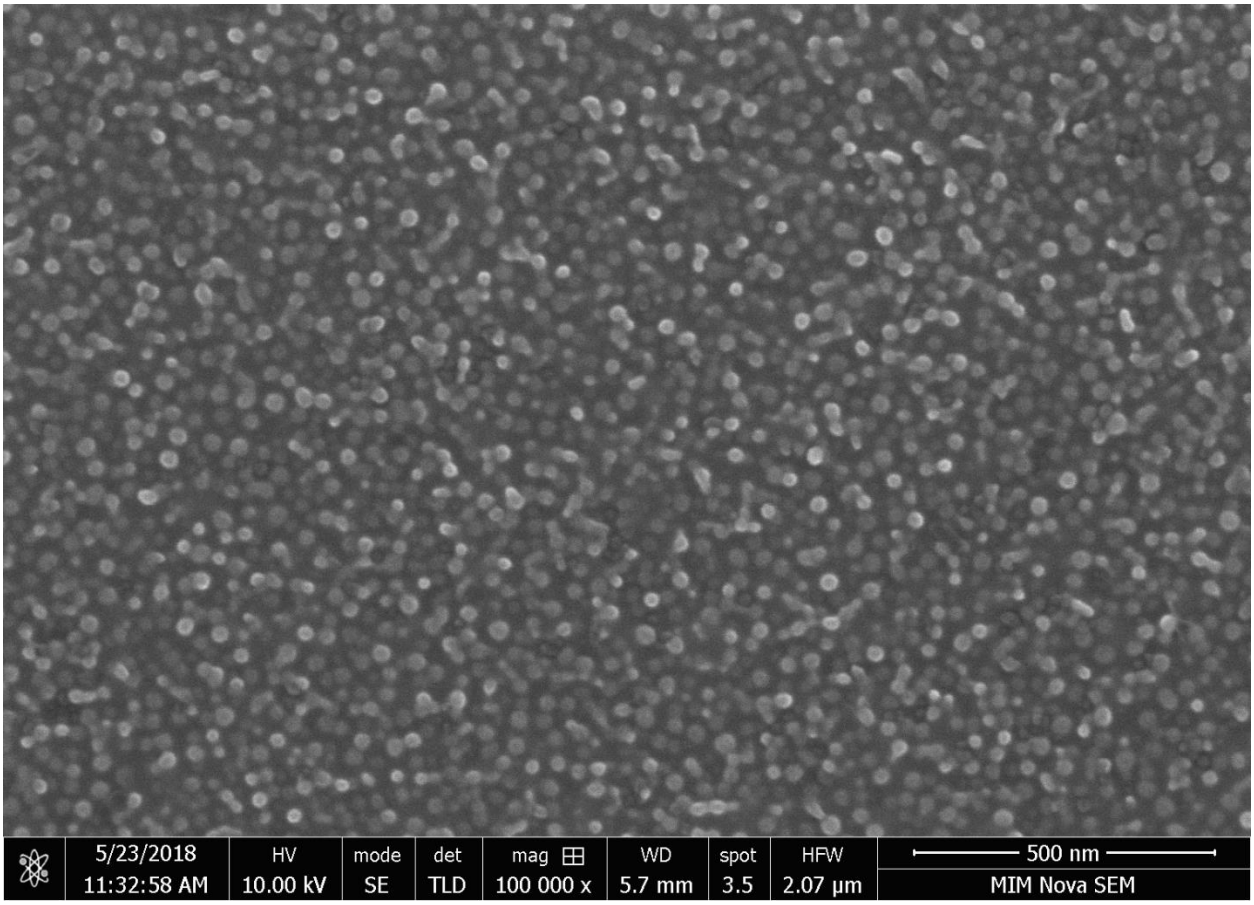

Figure 4.4: SEM micrograph of Haynes 282 after standard heat treatment that shows spherical γ′ precipitates (15 – 30 nm).

4.1.4 Microstructure of Special Aged Haynes 282

The optical microscopy and SEM micrographs in Figure 4.5 show the presence of sub-micron Mo- and Ti-rich primary carbides inside the grains and sparsely along the grain boundaries after the special aged heat treatment. These primary MC- and M_6C-type carbides have an average particle size, typically in the order of 2 to 5 μm. Minor secondary $M_{23}C_6$ carbides are precipitated along the grain boundaries and in the matrix, which can be attributed to the absence of the carbide stabilization step during the special aged heat treatment. The grain boundary is decorated with discrete carbides and spherical γ′ precipitates. This is consistent with a similar observation by Yan et al. [147] in which an increase in the aging temperature resulted in the precipitation of secondary γ′ particles and discontinuous carbides along the grain boundaries of a Ni-Fe-based superalloy. The special aged heat treatment resulted in an average grain size of ~90 μm. The higher aging temperature for the special aged, compared to the standard heat treatment, resulted in minimal coarsening of the γ′ precipitates, with an average precipitate size distribution of 40 – 60 nm as shown in Figure 4.6. The uniformly distributed precipitates remain mono-modal with a spherical morphology after the special aged heat treatment. The microhardness value of Haynes 282 after the special aged heat treatment is 390 HV ±13, which is equivalent to 41 HRC on the Rockwell hardness scale.

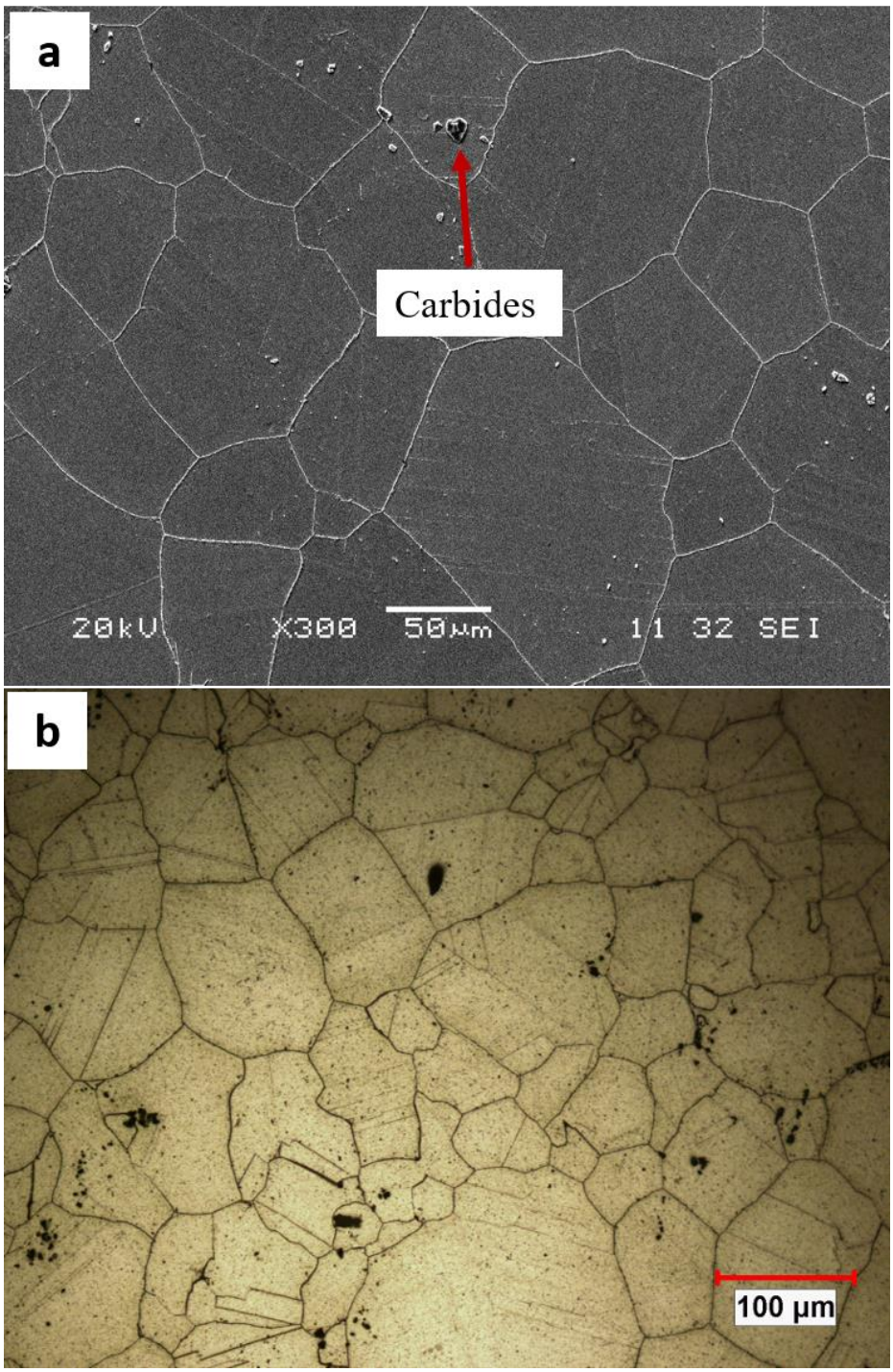

Figure 4.5: (a) SEM and (b) Optical microscopy micrographs of Haynes 282 after special aged heat treatment that shows carbide particles in the matrix and sparsely populated along the grain boundaries

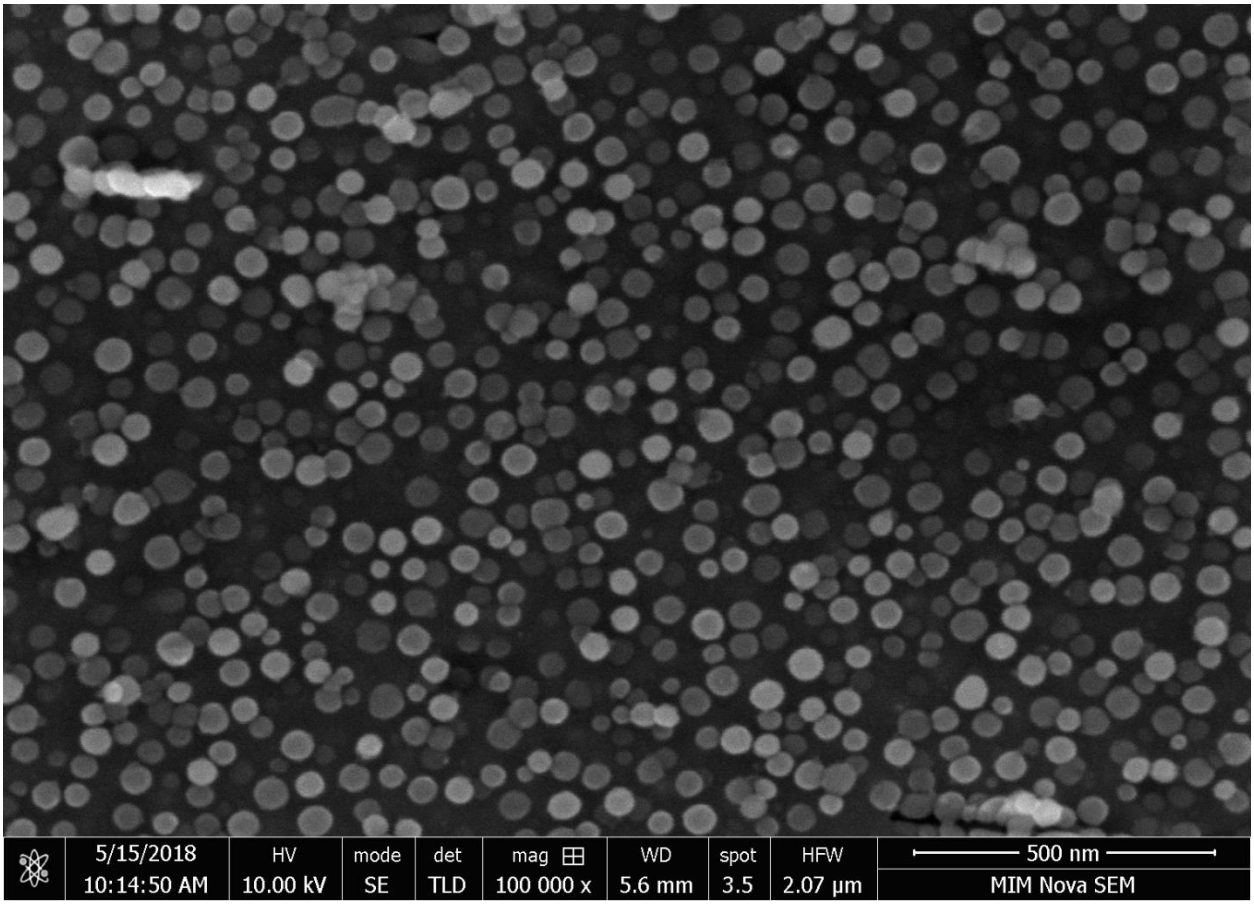

Figure 4.6: Micrograph of Haynes 282 taken with FEI Nova NanoSEM 450 after special aged heat treatment that shows spherical γ′ precipitates (40 – 60 nm).

4.2 Quasi-Static Compressive Behaviour of Haynes 282

This section presents the quasi-static compressive behaviour of Haynes 282 after solutionized, standard, and special aged heat treatments at room temperature and strain rates of 0.006/s and 0.035/s. The quasi-static behaviour of a material gives insight into the nature of loading pulses generated during impact deformation [148]. The experimental data from the quasi-static compression test are plotted as true stress against true strain. The tests were repeated for each test condition to ensure accuracy. Figure 4.7 shows the high repeatability of the tests done at room temperature and strain rate of 0.006/s for the solutionized heat treatment. Comparable results were obtained for the other test conditions.

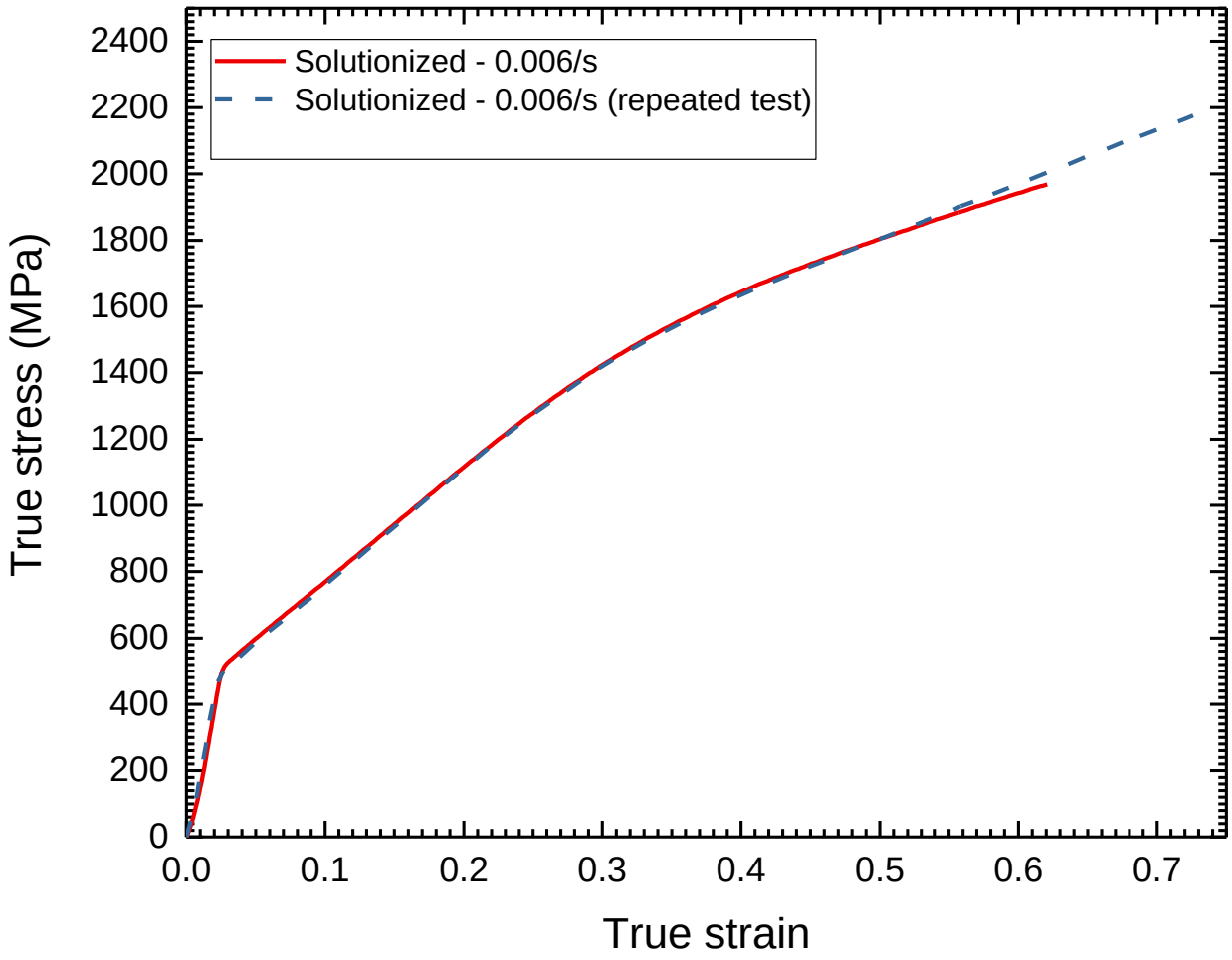

Figure 4.7: Plotted true stress vs true strain for the quasi-static behaviour of Haynes 282 after solutionized heat treatment at 0.006/s.

4.2.1 Standard Heat Treatment Condition

The plotted true stress vs. true strain curve of Haynes 282 after quasi-static compressive deformation is shown in Figure 4.8(a). The graphical representation shows that the flow stress in the standard heat treatment condition remains almost constant with an increase in the rate of deformation from 0.006/s to 0.035/s, up to the plastic strain of ~0.25. Beyond a true strain of 0.25, the flow stress of the alloy at the higher strain rate of 0.035/s slightly decreases in contrast to the strength at the lower strain rate of 0.006/s. However, stress saturation did not occur in the alloy within the range of strain rates and strains considered. The material showed an increase in strain hardening up to the maximum plastic strain of ~0.6 and flow stress of ~2000 MPa, at which stage the tests were stopped.

It is clear from the flow curve in Figure 4.8(a) that the plastic region of Haynes 282 during quasi-static deformation consists of only the work hardening stage. The steady state and softening stages are absent. The work hardening stage is characterized by a continuous increase in dislocation density as the deformation proceeds. The work hardening rate of the alloy computed by using the first derivative of the flow curve [149] is shown in Figure 4.8(b). The plot confirms that strain hardening is the dominant deformation mechanism as no thermal softening effect overriding those of work hardening occurred in the material during deformation. Moreover, the samples did not fracture at both strain rates investigated and there was no evidence of cracks on the surface of the samples after the test. After standard heat treatment, Haynes 282 is less sensitive to the strain rate effect under quasi-static compressive loading.

(a)

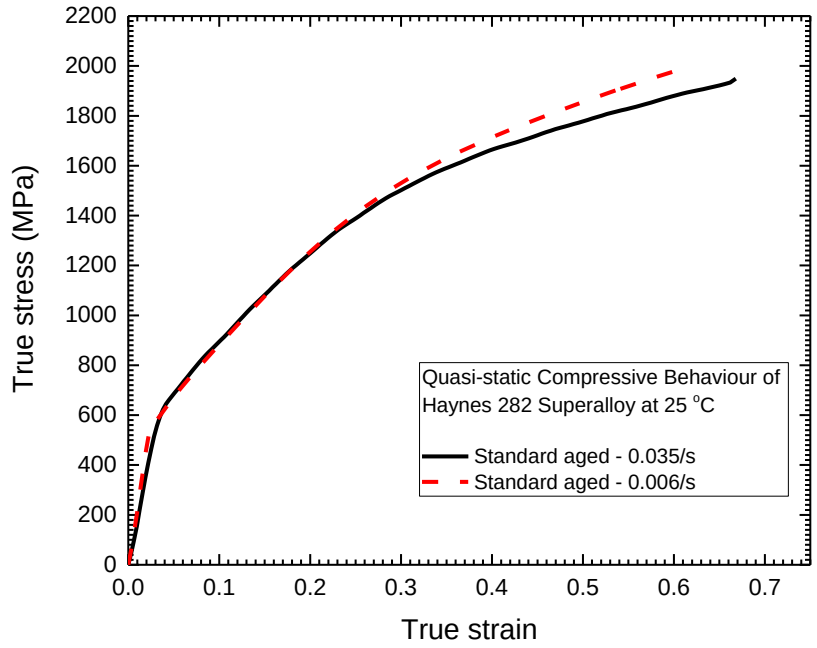

(b)

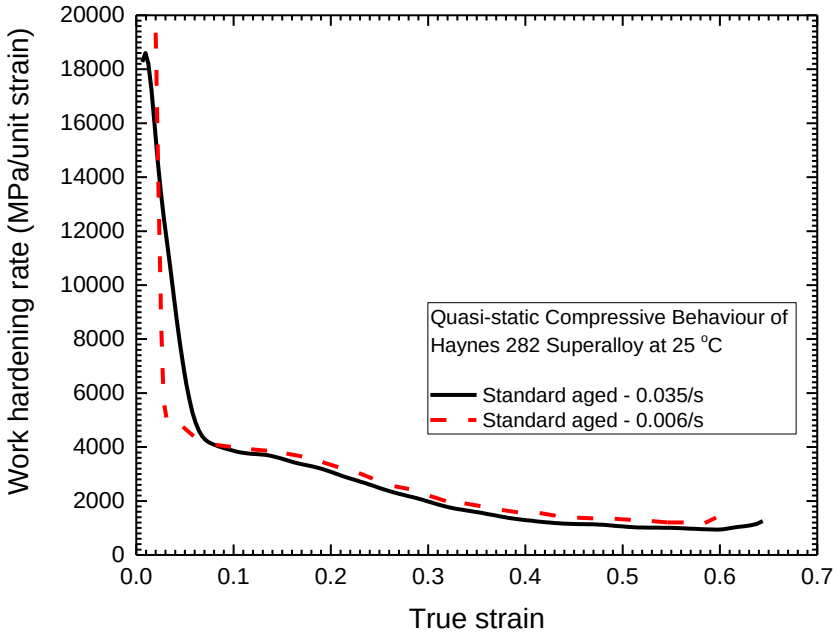

Figure 4.8: (a) True stress vs. true strain, (b) Work hardening rate vs. true strain for the quasi-static compressive behaviour of Haynes 282 after standard heat treatment at strain rates of 0.006/s and 0.035/s.

4.2.2 Special Aged Heat Treatment Condition

There was little decrease in the compressive flow stress of Haynes 282 in the special aged heat treatment condition, with an increase in the deformation strain rate from 0.006/s to 0.035/s, up to a plastic strain of ~0.25 as shown in Figure 4.9(a). Beyond this strain, the flow stress at the higher strain rate decreased more with increases in plastic strain. At a strain of 0.6, the flow stress at both strain rates approached a difference of ~140 MPa. The work hardening rate against the true strain plot in Figure 4.9(b) shows that strain hardening is the active deformation mechanism. As with the observations for the standard heat treatment, stress saturation and thermal softening are not observed in the special aged condition within the limits of the strain rates studied.

(a)

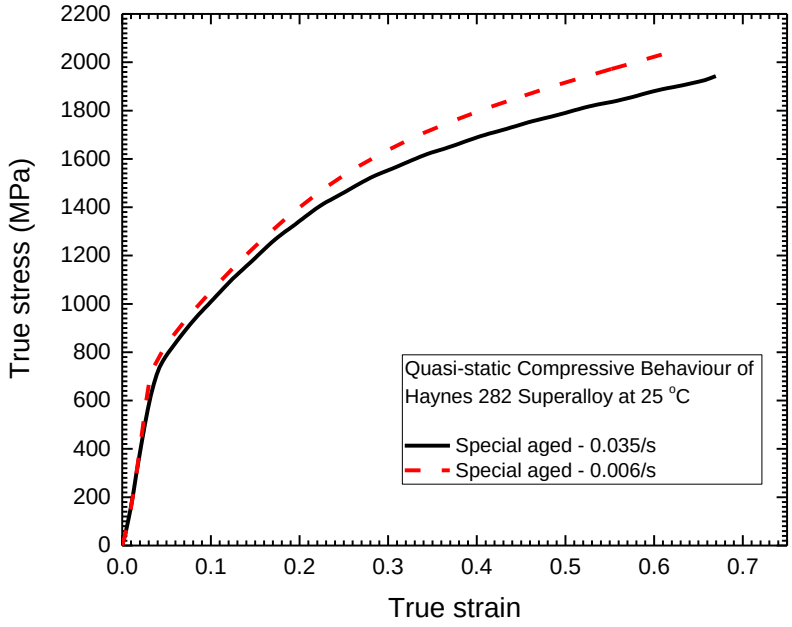

(b)

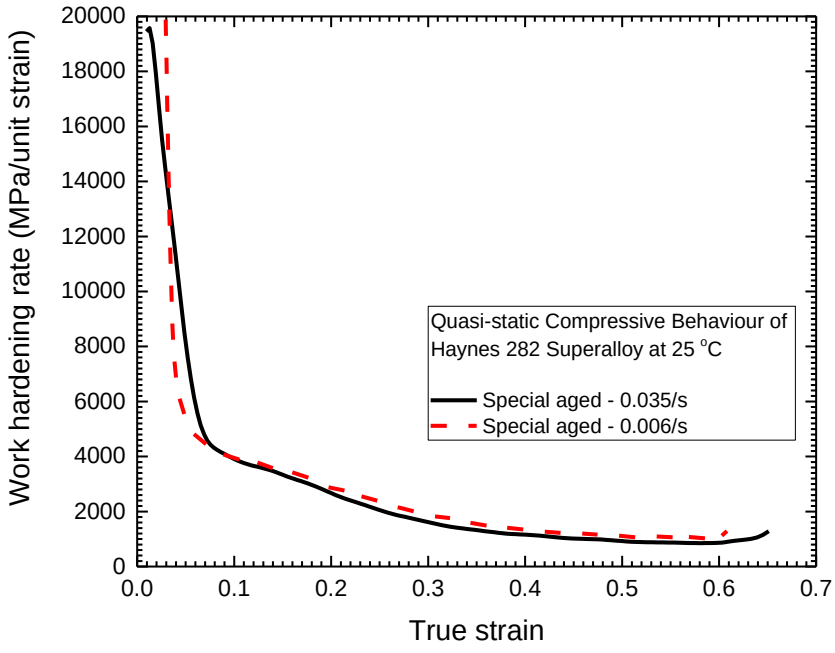

Figure 4.9: (a) True stress vs true strain, (b) Work hardening rate vs true strain for the quasi-static compressive behaviour of Haynes 282 after special aged heat treatment at strain rates of 0.006/s and 0.035/s.

4.2.3 Solutionized Heat Treatment Condition

Deformation in the solutionized condition proceeded more readily in comparison to the aged conditions. Figure 4.10(a) presents the flow curves at strain rates of 0.006/s and 0.035/s. As the deformation strain rate increases from 0.006/s to 0.035/s, the flow stress remains almost constant within the elastic range but decreases with increases in the plastic strain. The difference in the strength of the solutionized alloy at both strain rates is close to 160 MPa at a strain of 0.6. The work hardening rate of the alloy after solutionized is shown in Figure 4.10(b). Consistent with the observation in the aged condition, strain hardening dominates the deformation mechanism and no thermal softening effect is observed.

As expected, Haynes 282 has a lower compressive strength after solutionizing. This is because, after solutionized heat treatment, if γ' precipitates are present, their size would be very small, compared to those observed in the aged condition, such that most of the strength is imparted by solid solution strengthening from the alloying elements.

(a)

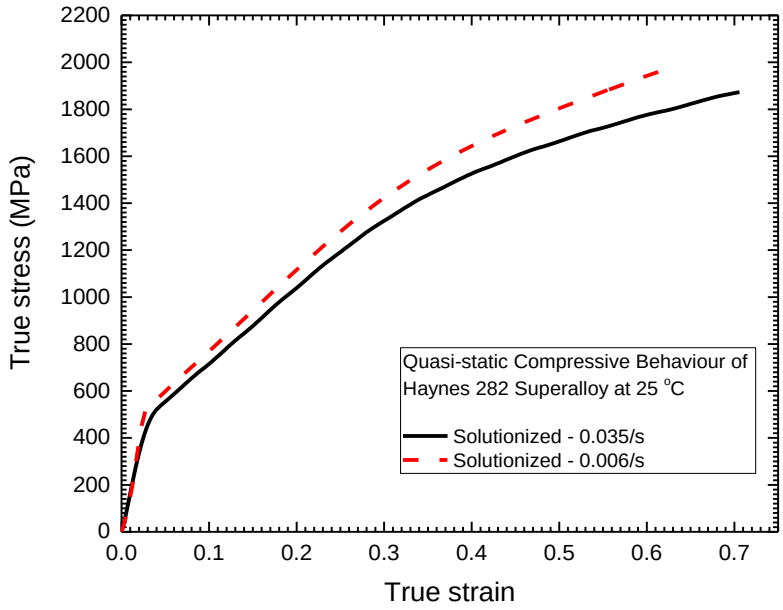

(b)

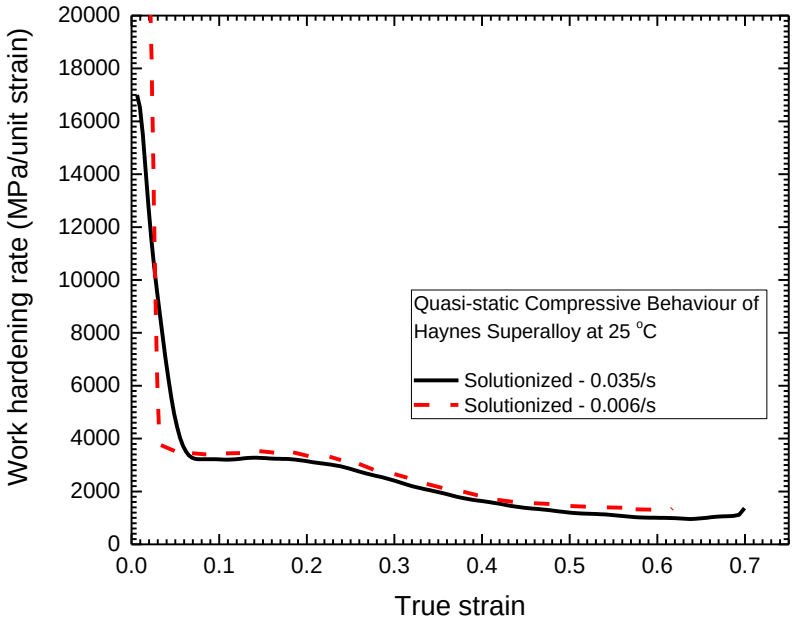

Figure 4.10: (a) True stress vs true strain, (b) work hardening rate vs true strain for the quasi-static compressive behaviour of Haynes 282 after solutionizing at strain rates of 0.006/s and 0.035/s.

4.2.4 Effect of Heat Treatment on Quasi-Static Compressive Response of Haynes 282

A comparison of the flow behaviour of Haynes 282 under the three heat treatment conditions and deformed at a strain rate of 0.006/s is shown in Figure 4.11(a). The flow curves show that the compressive strength of Haynes 282 under quasi-static deformation is highest after the special aged heat treatment, followed by standard heat treatment, and is lowest after solutionizing. At a strain of 0.1, there is a significant increase in the strength of the alloy when moving from the solutionized (780 MPa) to the standard heat treatment at 880 MPa, and then the special aged at 1060 MPa. A similar trend is observed for all the deformation conditions up to 0.5 plastic strain. Beyond the strain of 0.5, the difference in the corresponding strength of the alloy under the three heat treatment conditions decreases. The percentage difference in the strength of the alloy in the special aged and solutionized heat treatments, at a strain rate of 0.006/s, decreases from 26% at a true strain of 0.1 to 4% at a true strain of 0.6.

Figure 4.11(b) plots the work hardening rate against the true strain of Haynes 282 at the strain rate of 0.006/s. It can be observed that the aged conditions strain hardens more than the solutionized condition at the initial stage of deformation. However, at a strain of ~0.2, the aged alloy begins to lose its strain hardening capability; subsequently, the solutionized alloy strain hardens more than the aged conditions as it undergoes more uniform deformation with an increase in strain.

The higher strength of Haynes 282 after undergoing the special aged heat treatment, compared to the standard heat treatment, might be attributed to the different mechanisms of dislocation-precipitate interaction in both aged conditions. Precipitate shearing rather than Orowan looping could be the operating deformation mechanism in both aged conditions. This is supported by the

(a)

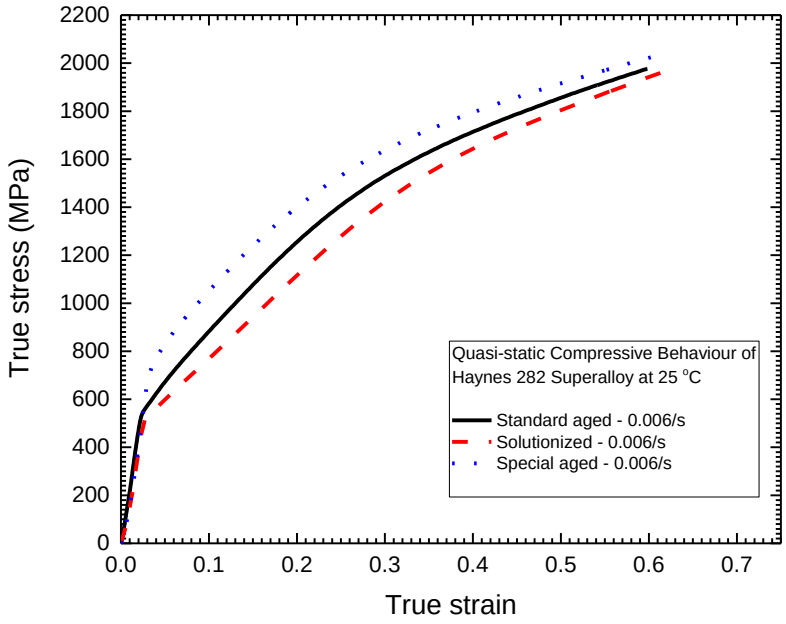

(b)

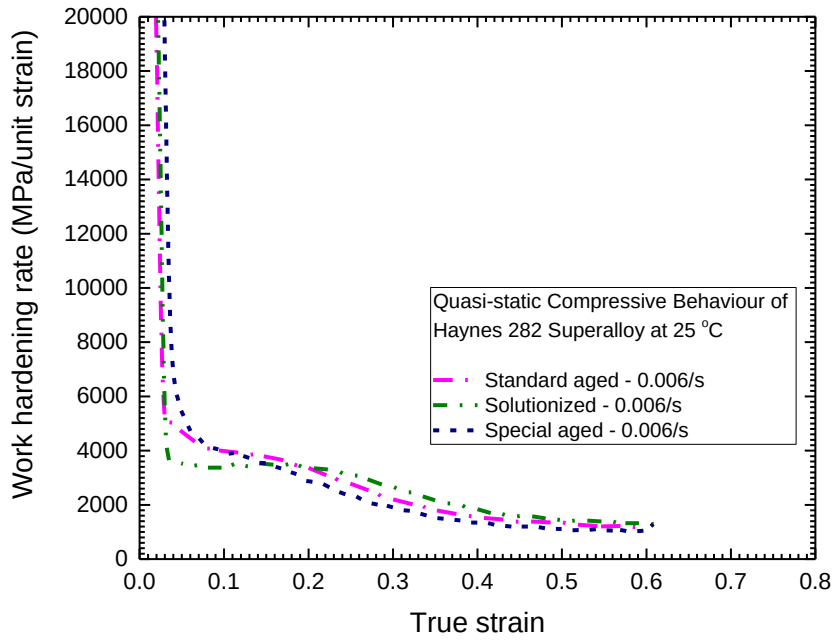

Figure 4.11: (a) True stress vs true strain, (b) Work hardening rate vs true strain for the quasi-static compressive behaviour of Haynes 282 superalloy at room temperature and strain rate of 0.006/s in the different heat treatment conditions

works of Zhang et al. [150] in which precipitate shearing was reported as the predominant deformation mechanism from room temperature up to 600^{o}C during the tensile deformation of Haynes 282 alloy with an average precipitate size of 49.8 ± 0.3 nm (1140^{o}C/2 hours/AC, 1010 ^{o}C/2 hours/AC, and 760 ^{o}C/24 hours/AC). Moreover, it is acknowledged in the literature that, for coherent precipitates, precipitate shearing rather than Orowan looping dominates the deformation mechanism if the precipitates are small and have not reached the critical size required for Orowan looping (or dislocation bypassing) to occur. In addition, larger precipitate size increases the critical resolved shear stress required for dislocations to shear the precipitates, which leads to increased hardening of the material [151], [152]. Therefore, the larger precipitate size after the special aged heat treatment (40 – 60 nm) could increase the critical resolved shear stress required for dislocations to shear the precipitates, which leads to increased hardening and stability of Haynes 282. In contrast, the smaller precipitate size after standard heat treatment heat treatment (15 – 30 nm) could provide less resistance to precipitate shearing by moving dislocations, leading to a reduction in the strength of the material. Furthermore, Haas et al. [1] reported that there is a correlation of the precipitate size with Vickers hardness in Haynes 282. They found that peak hardness could not be achieved in Haynes 282 at aging temperatures less than 825^{o}C, even after 4 hours of aging. Their observation and the results of this study suggest that the standard aging temperature of 788^{o}C may be insufficient to achieve the peak hardness of Haynes 282.

Within the range of strain rates investigated, Haynes 282 has the highest quasi-static compressive strength in the special aged condition, followed by the standard heat treatment, and the lowest strength is observed in the solutionized condition. No mechanical instability arising from thermal softening overcoming work hardening was observed across the three heat treatment conditions.

4.3 Quasi-Static Tensile Behaviour of Haynes 282

The quasi-static tensile behaviour of Haynes 282 after solutionized, standard, and special aged heat treatment conditions investigated at room temperature and a strain rate of 0.003/s is presented in this section. Tensile testing by applying a continuously increasing uniaxial load is used to provide a better understanding of the basic design parameters of the strength of a material and also serves as an acceptance criterion for material specification [153]. The experimental load-elongation measurement is converted into nominal stress-strain for analysis. The yield strength, ultimate tensile strength (UTS), strain-hardening exponent, Young's modulus of elasticity, and ductility expressed as a percentage of elongation are used to characterize the uniaxial tensile deformation behaviour of Haynes 282.

The flow curves and variations in the tensile properties across the three heat treatment conditions are presented in Figure 4.12 and Table 4.1, respectively. The UTS of Haynes 282 is highest after the special aged heat treatment at 1184 MPa, followed by the standard heat treatment at 1040 MPa, and the solutionized condition in which the UTS is the lowest at 866 MPa. Aging obviously provides a higher tensile strength with a concomitant reduction in ductility as opposed to solutionizing. It was observed in the standard heat treatment that Haynes 282 exhibits a ductility of 29% and yield strength of 678 MPa. These values are in agreement with those reported in [9], [55], [124], and [144]. After the special aged heat treatment was carried out, the ductility and yield strength of Haynes 282 increased to 40% and 752 MPa, respectively. However, solutionizing the alloy produces a larger ductility (70%) and lower yield strength (462 MPa).

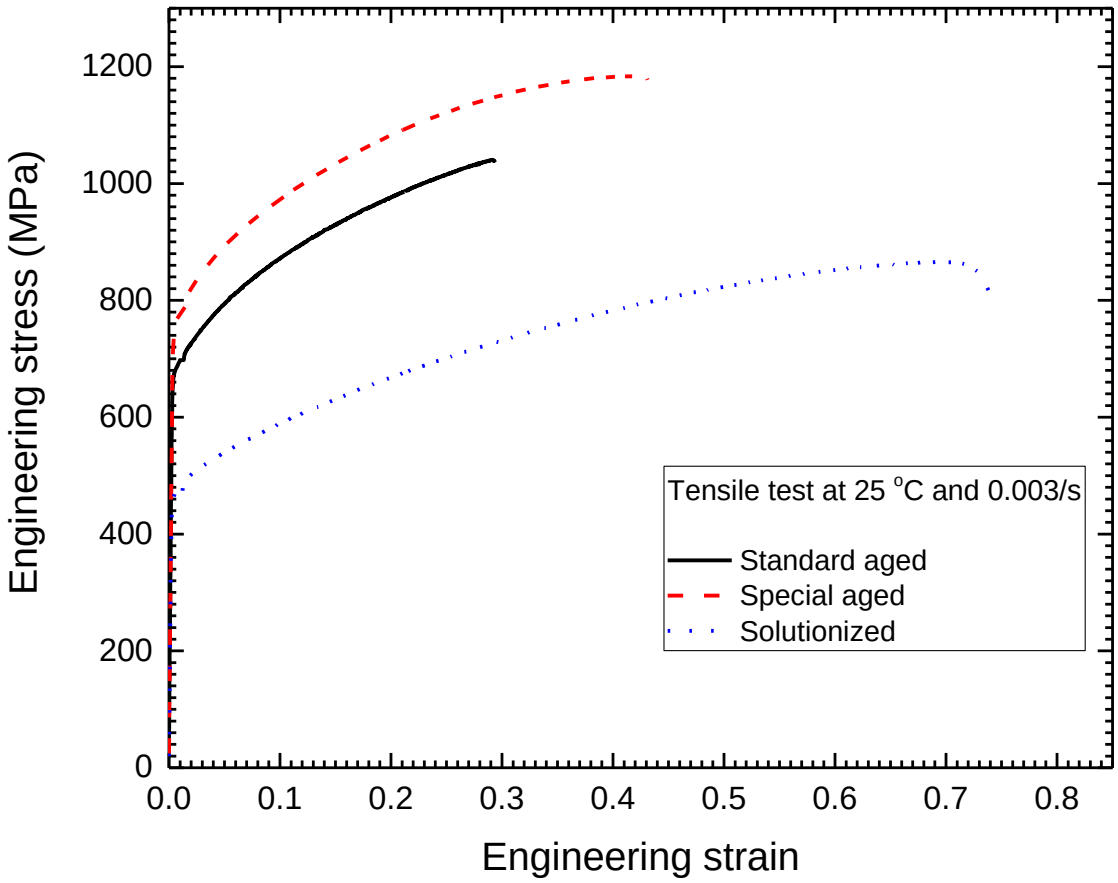

Figure 4.12: Nominal stress-strain tension curves for Haynes 282 under different heat treatment conditions at room temperature and strain rate of 0.003/s

Table 4.1: Tensile properties of Haynes 282 at room temperature

Type of heat treatment	**Yield strength 0.2% offset (MPa)**	**Modulus of elasticity (GPa)**	**% Elongation**	**UTS (MPa)**	**Strain hardening exponent**
Solutionized	462	200	70	866	0.538
Standard heat treatment	678	216	27	1040	0.377
Special aged	752	218	40	1184	0.382

The tensile flow curves in the plastic range (Figure 4.12) follows Hollomon's power law [155] which describes the strain hardening behaviour of a material by relating the true stress (σ) to the true strain (ε) during deformation as:

$$\sigma = K\varepsilon^n \qquad (4.1)$$

where K is the strength coefficient and n is the strain-hardening exponent. For Equation 4.1 to be valid, a log-log plot of true stress against true strain gives a linear relationship of the flow behaviour during deformation. The strain-hardening exponent is an indicator of the strain hardening capability of a material [156]. For a perfectly elastic material, the magnitude of n approaches one, whilst for a perfectly plastic material, the magnitude of n tends to zero. As such, materials with a higher n-value have better formability [157]. The tensile test results showed that the solutionized alloy has the highest strain-hardening exponent of 0.538, followed by the sample that underwent the special aged heat treatment at 0.382, and finally, the standard heat treatment at 0.377. This confirms that Haynes 282 has a higher strain hardening capability in the solutionized condition during quasi-static tensile deformation.

To understand the influence of the heat treatment on the fracture behaviour of Haynes 282, an SEM examination of the fracture morphologies was conducted. The fractured morphology in Figure 4.13 shows intergranular ductile failure resulting from grain boundary tearing after standard heat treatment. It has been suggested that reduction in ductility is caused by the precipitation of nearly continuous $M_{23}C_6$ carbides at the grain boundaries [10], similar to our observation in the standard heat treatment condition (Figure 4.16(a)). Presumably, the carbides act as crack initiation sites and the local fractures of the carbides easily propagate due to the interconnectivity of the carbide morphology [10], [158]. Lamellar $M_{23}C_6$ carbide tearing has been observed in aged Ni-Cr-W superalloy during tensile deformation [159].

The fractured surface of Haynes 282 after the special aged heat treatment shows intergranular ductile tearing at the grain boundaries with small dimples (Figure 4.14). The precipitation of the γ′ particles and some of the discrete carbides (Figure 4.16(b)) along the grain boundaries could contribute to the larger ductility observed in Haynes 282 after the special aged heat treatment as the tensile loads are easily transferred to the ductile Ni-matrix in the event of carbide fracture rather than propagating through interconnected carbides [10]. The fractured surface after solutionized heat treatment in Figure 4.15 shows dimpled ductile failure which results in high ductility, an indication of transgranular failure through microvoid coalescence [160], [161].

The higher strength of Haynes 282 after the special aged heat treatment, as opposed to the standard heat treatment, can also be related to the difference in precipitate size and the resultant effect on dislocation mobility during deformation. The strength of most superalloys tend to decrease with an increase in the size of the γ′ precipitate [147], [162], partly due to over-aging of the precipitates, however, the strength of some of the γ′-strengthened superalloys has been reported to increase with an increase in the size of the γ′ precipitates [163], [164]. Like the quasi-static compressive behaviour, the larger precipitate size resulting from the special aged heat treatment could increase the critical resolved shear stress required for dislocations to cut the precipitates, thus strengthening the material.

The tensile properties of Haynes 282 after undergoing the special aged heat treatment (a one-step aging process) proposed in this study slightly exceed those reported for a one-step aging treatment of Haynes 282 that has been evaluated in [165] for advanced ultra-supercritical (A-USC) steam boiler applications, see Table 4. 2.

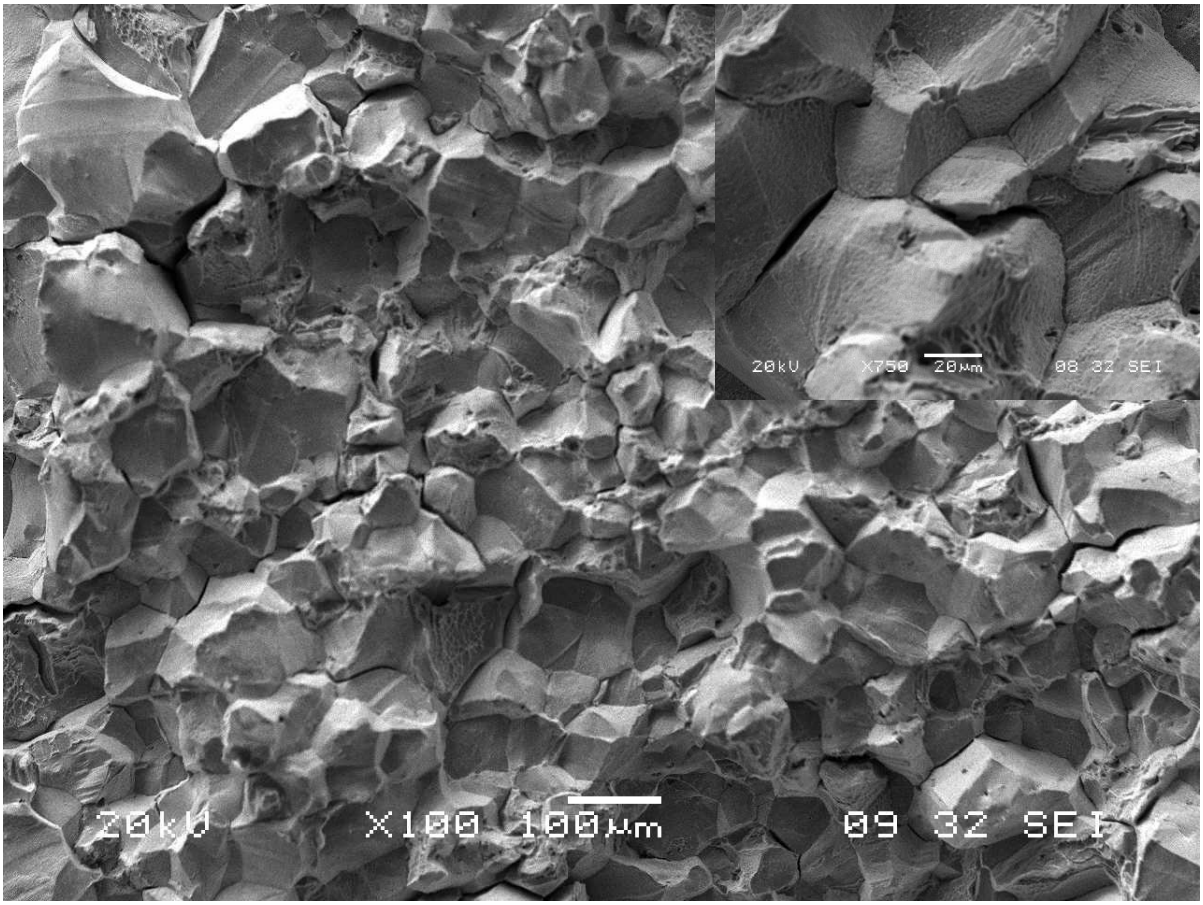

Figure 4.13: SEM micrograph of intergranular ductile fracture morphology after standard heat treatment

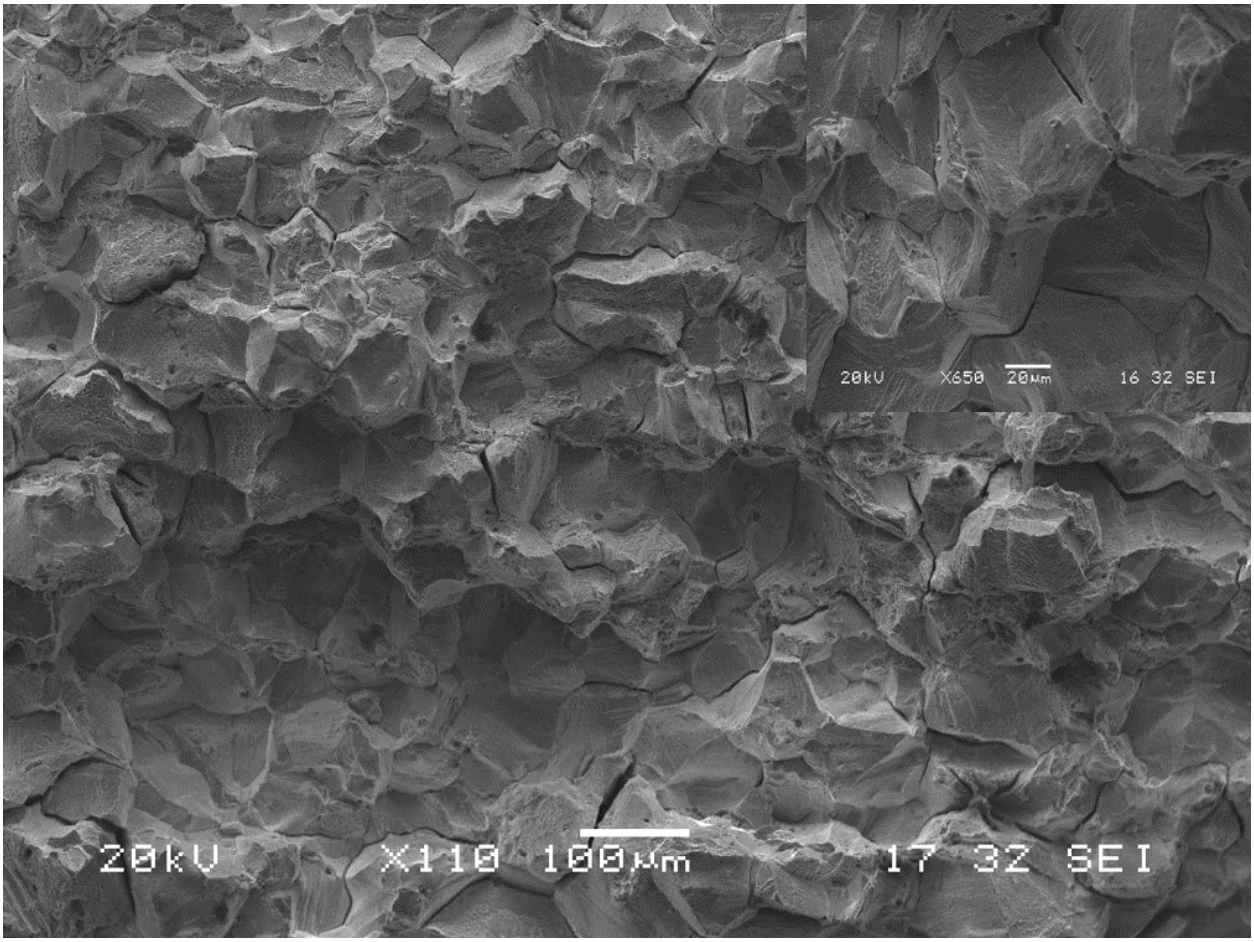

Figure 4.14: SEM micrograph of intergranular ductile failure with small dimples after special aged heat treatment

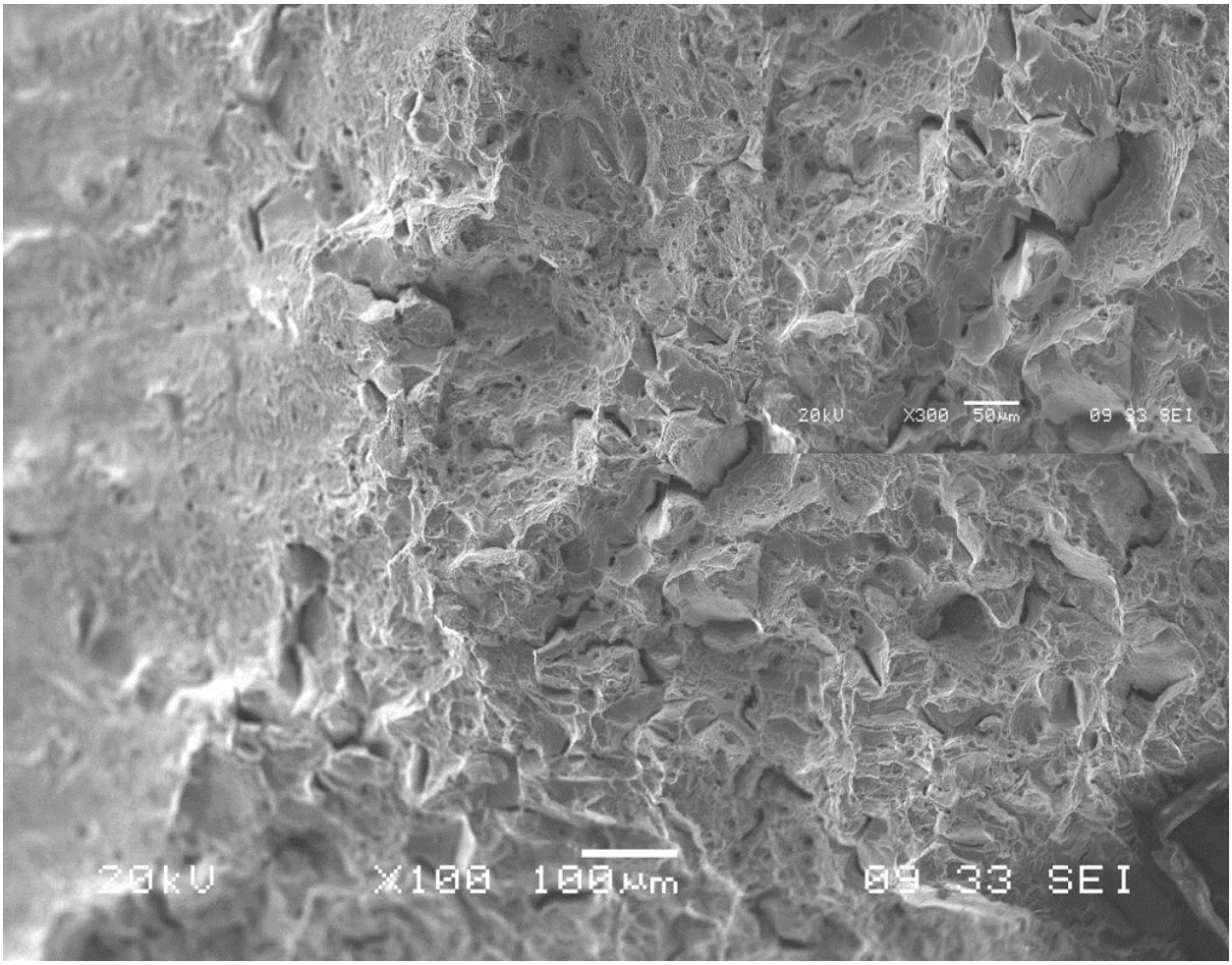

Figure 4.15: SEM micrograph that shows morphology with dimpled ductile fracture due to transgranular failure after solutionized heat treatment

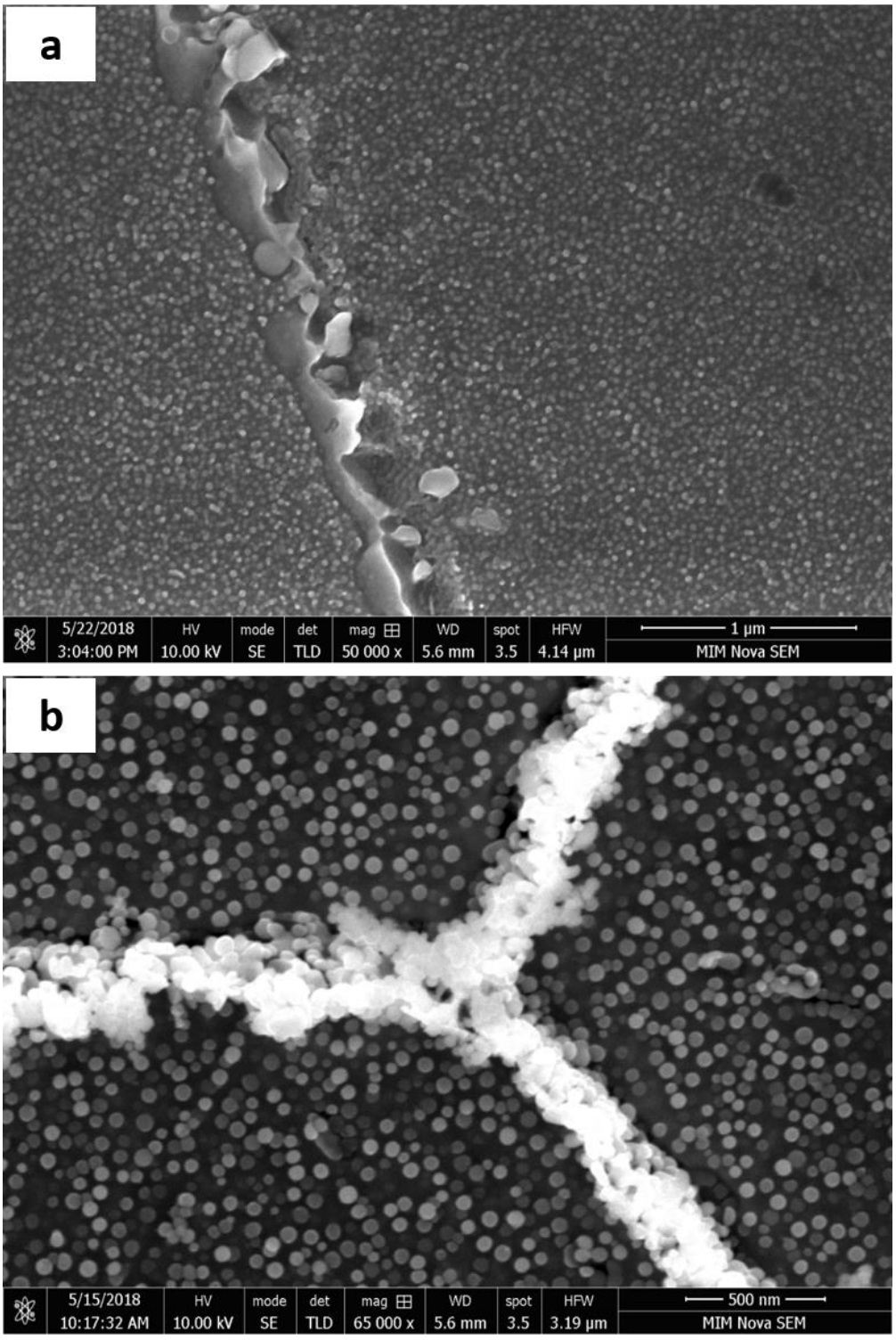

Figure 4.16: SEM micrograph of Haynes 282 after (a) standard heat treatment that shows interconnected carbides along the grain boundary, and (b) special aged heat treatment that shows γ′ precipitates along the grain boundary

Table 4. 2: Tensile properties of one-step aging treatment for Haynes 282 at room temperature

Type of heat treatment	**Yield strength (MPa)**	**UTS (MPa)**	**% Elongation**
900^{o}C/1 hour/FC	752	1184	40
800^{o}C/8 hours/AC*	741	1183	31.3
800^{o}C/4 hours/AC*	734	1169	34.6

* Data from [165]

4.4 Dynamic Impact Behaviour of Haynes 282

This section discusses the influence of strain rate and temperature on the dynamic impact behaviour of Haynes 282 and its susceptibility to form ASBs after solutionized, standard, and special aged heat treatments are carried out.

4.4.1 Influence of Strain Rate on Dynamic Impact Behaviour of Haynes 282

To understand the influence of the strain rate on the deformation behaviour of Haynes 282 under ballistic loading, an analysis is presented on its dynamic impact behavior observed at room temperature. A similar strain rate softening behaviour was observed at all temperatures studied.

4.4.1.1 Solutionized Heat Treatment Condition

Figure 4.17(a) shows the influence of strain rate on the deformation behaviour of Haynes 282 in the solutionized condition for tests carried out at room temperature and an impact momentum from 27 – 47 $Kg.ms^{-1}$ (which correspond to strain rates from 2,000 to 4,275/s). The flow curves show a slight decrease in the strength of Haynes 282 with an increase in the deformation strain rate at low strains of up to ~0.3. Beyond this strain, the flow stress remains nearly constant with further increases in the strain rate. The strain that corresponds to the peak stress increases with increases in the strain rate as observed for FCC alloys [166]. The work hardening rate of the solutionized alloy decreases with increasing strain rate at the initial stage of deformation; see Figure 4.17(b). However, the critical strain at which thermal softening dominates the deformation mechanism which leads to mechanical instability increases with an increase in the strain rate, from a strain of ~0.3 at a strain rate of 2,000/s to a plastic strain of ~0.5 at a strain rate of 3,300/s. The critical strain occurs when the work hardening rate of the material drops to zero.

(a)

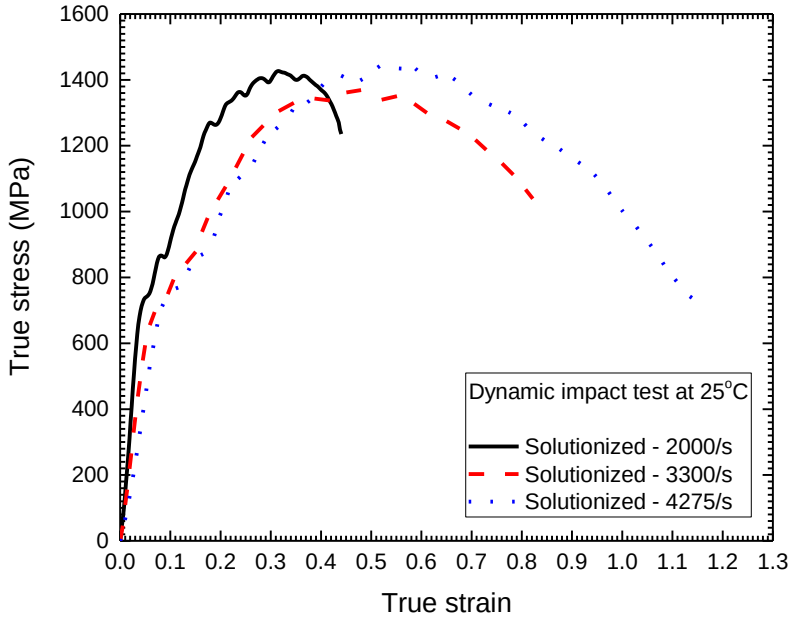

(b)

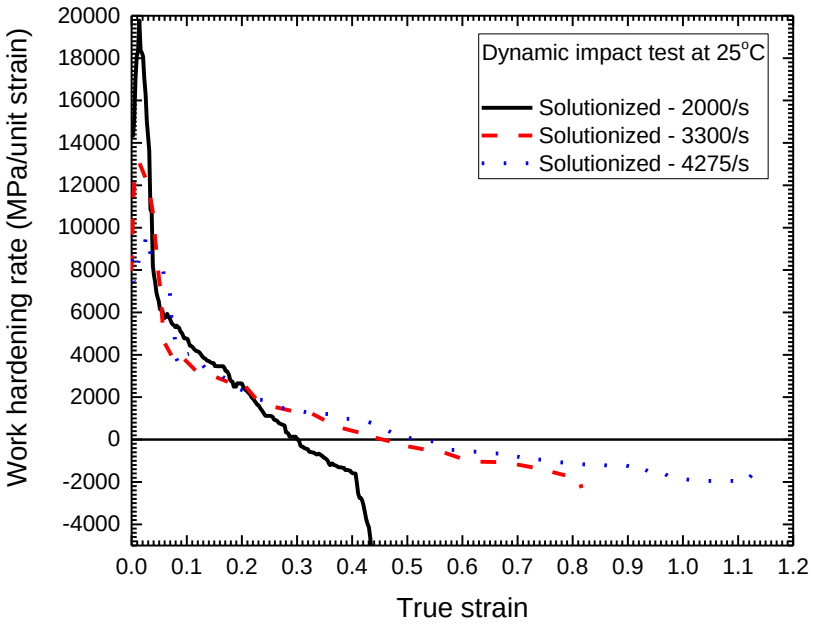

Figure 4.17: (a) True stress vs true strain, (b) Work hardening rate vs true strain plots for dynamic impact behaviour of Haynes 282 at room temperature after solutionized heat treatment

4.4.1.2 Special aged Heat Treatment Condition

After undergoing the special aged heat treatment, the strength of Haynes 282 decreased with an increase in the strain rate as shown in Figure 4.18(a) under high strain rate deformation. The effect is more pronounced as the deformation increases from 2000/s to 3300/s strain rates. However, there is a nearly constant flow stress dependence with strain rate after further increases in the strain rate greater than 3300/s. This contrasts with the findings for most Ni-based superalloys which show a positive strain rate dependence with flow stress during dynamic impact deformation [101], [167], [168]. The observed strain rate softening at higher strain rates may be attributed to the increase in dislocation density with a corresponding annihilation effect thus leading to strength reduction [100]. Also, higher strain rates could lead to increased adiabatic heating from precipitate shearing and strain-assisted diffusion in localized regions with a subsequent increase in dislocation motion and ease of deformation [100].

The critical deformation strain for mechanical instability, represented by the zero crossing in the work hardening rate versus true strain plot, as shown in Figure 4.18(b), increases with an increase in the deformation strain rate. The critical strain increased from a strain of ~0.25 at a strain rate of 2,000/s to a strain of ~0.36 at a strain rate of 3,300/s.

(a)

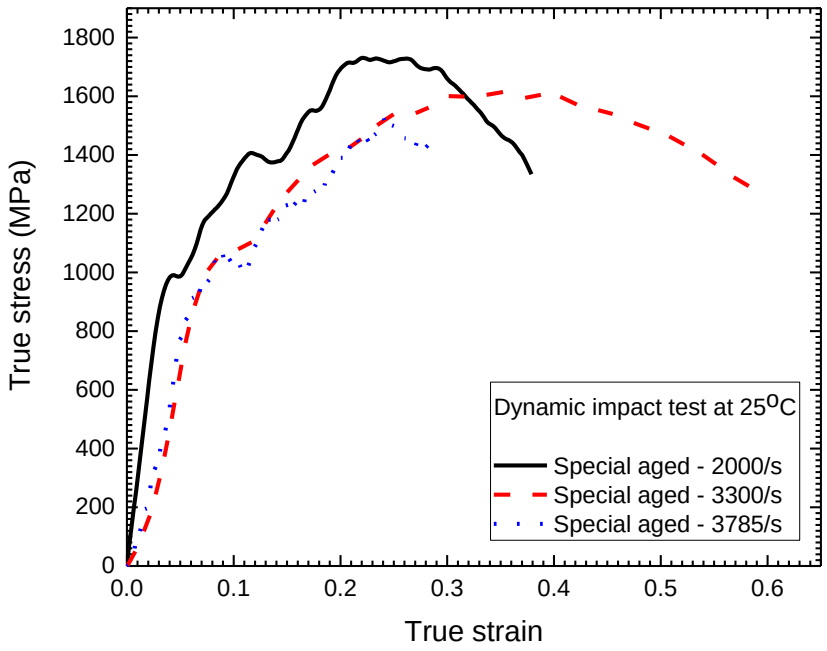

(b)

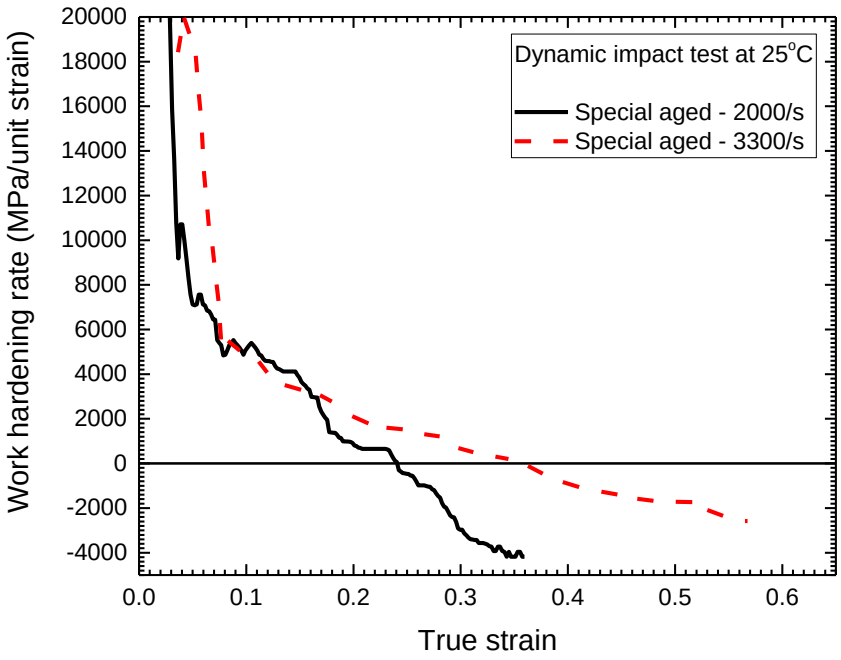

Figure 4.18: (a) True stress vs true strain, and (b) work hardening rate vs true strain plots for dynamic impact behaviour of Haynes 282 at room temperature during special aged heat treatment

4.4.1.3 Standard Heat Treatment Condition

The deformation flow curve at room temperature in the standard heat treatment condition, (Figure 4.19(a)), shows that Haynes 282 has a lower deformation stress value with increases in the strain rate up to a plastic strain of ~0.3. However, the peak strength of the alloy remains nearly constant at both deformation strain rates of 2000/s and 3300/s. In addition, it can be observed from the flow curves that the strain that corresponds to the peak stress increases with an increase in the strain rate. The deformation at a higher strain rate of 3300/s could absorb more impact energy, which is shown by the area under the stress-strain curve, prior to failure.

The work hardening rate versus true strain is plotted in Figure 4.19(b). For the deformation at a strain rate of 2000/s, work hardening remained the primary cause of deformation up to a critical strain of ~0.3 at which stage thermal softening effect dominates the deformation, thus leading to failure. At a strain rate of 3300/s, the critical strain for the onset of mechanical instability due to thermal softening increased to ~0.45.

(a)

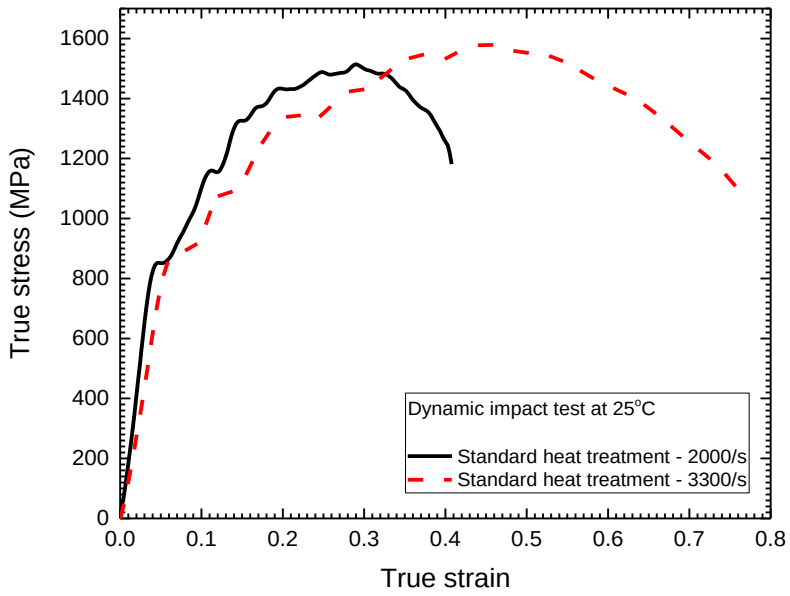

(b)

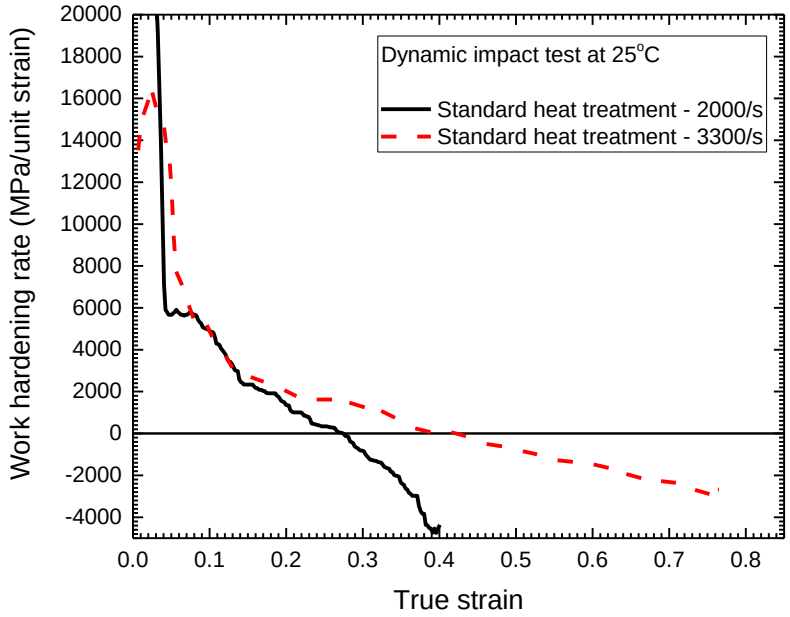

Figure 4.19: (a) True stress vs true strain, (b) Work hardening rate vs true strain plots for dynamic impact behaviour of Haynes 282 at room temperature for standard heat treatment condition

4.4.1.4 Comparison of Effect of Strain Rate on Dynamic Impact Behaviour of Haynes 282 in the Aged and Solutionized Heat Treatment Conditions

Figure 4.20(a) shows the dynamic impact flow curves of Haynes 282 superalloy at room temperature and impact momentum of 35 $Kg.ms^{-1}$ for the three heat treatment conditions (solutionized, standard, and special aged). Special aged leads to the highest flow stress across all of the heat treatment conditions. This is closely followed by the standard heat treatment, and then the solutionized condition with the least flow stress. A similar trend in the strength of Haynes 282 is observed for all strain rates and at all temperatures in this study. The flow stress of Haynes 282 for all of the heat treatment conditions shows a near constant to negative strain rate dependence. This is in close agreement with the findings by Rodríguez-Millán et al. [14] that the strength of Haynes 282 after standard heat treatment is nearly independent of the strain rate for deformations at room temperature up to a strain rate of 2800/s. This observation shows that Haynes 282 could be more easily machined in comparison to the most-widely used Ni-based superalloy, Inconel 718, which shows positive strain rate sensitivity with flow stress [168].

As can be seen in Figure 4.20(b), the rate of work hardening is highest after solutionizing, followed by standard heat treatment, and least after special aged heat treatment. The critical strain at which the thermal softening effect overrides that of the work hardening approaches 0.45 after solutionizing as opposed to 0.35 for special aged, in tests done at 35 $Kg.ms^{-1}$ (which corresponds to a strain rate of ~3300/s). After solutionizing, Haynes 282 can absorb more impact energy during deformation by diffusing the macroscopic shear zone over a wider area. This contrasts with the aged conditions with higher strength and lower strain hardening capability that predisposes the alloy to the formation of ASBs due to localized deformation on an active and narrow slip plane.

Within the limits of the high strain rate deformation investigated in this study, it is observed that Haynes 282 has the highest strength after special aged heat treatment, followed by standard heat treatment, and the least strength is observed in the solutionized condition. The reverse holds true for the strain hardening behaviour of Haynes 282 under ballistic loading in which the alloy strain hardened most after solutionized heat treatment, followed by standard heat treatment, and the least strain hardening capability is observed after special aged heat treatment.

(a)

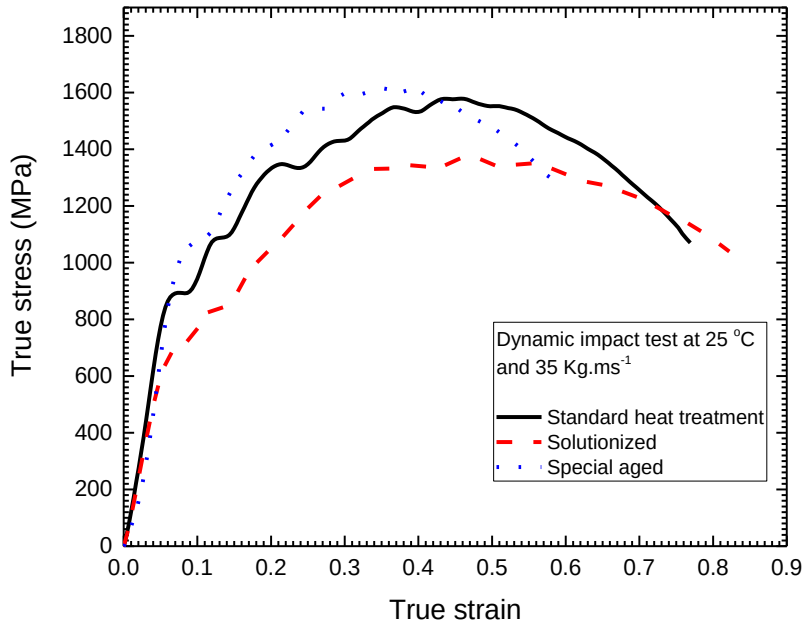

(b)

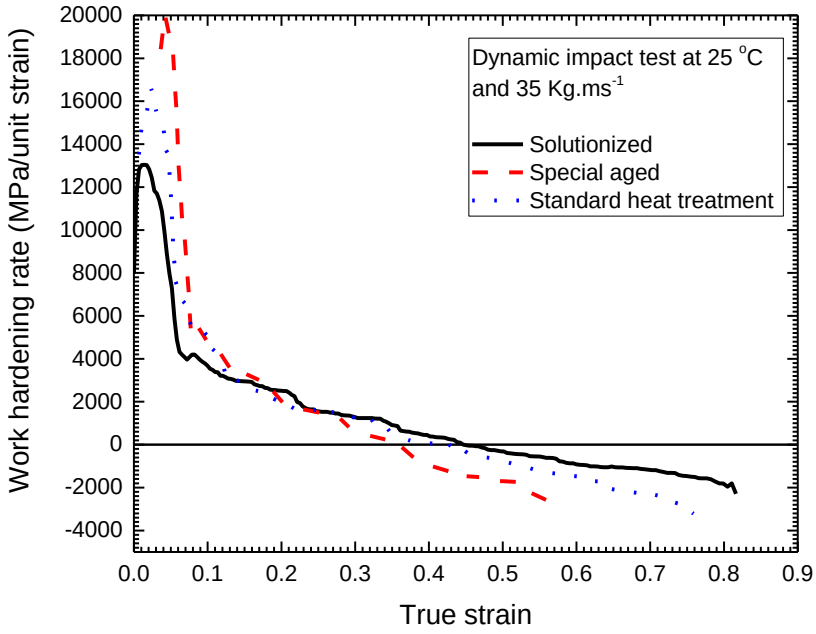

Figure 4.20: True stress vs true strain, (b) Work hardening rate vs true strain plots for dynamic impact behaviour of Haynes 282 at room temperature for different heat treatment conditions

4.4.2 Influence of Temperature on Dynamic Impact Behaviour of Haynes 282

The influence of temperature on the dynamic impact behaviour of Haynes 282 at impact momentums from 27 to 47 Kg.ms^{-1} (corresponding to strain rates from 2 x 10^3 to 9 x 10^3 s^{-1}) and temperatures that range from 25^{o}C to 800^{o}C by using the direct impact Hopkinson pressure bar is discussed in this section. The influence of temperature in the different heat treatment conditions is evaluated to provide a better understanding of the likelihood of failure of Haynes 282 as a function of deformation temperature.

4.4.2.1 Solutionized Heat Treatment Condition

The dynamic impact behaviour of Haynes 282 after solutionizing is discussed in this section. The flow curves in Figure 4.21(a) shows that at a constant impact momentum of 35 Kg.ms^{-1}, the strength of Haynes 282 is reduced with an increase in the deformation temperature from 25^{o}C to 800^{o}C. Similar observations were made for impact momentums of 27 and 47 Kg.ms^{-1}. Figure 4.21(b) presents the flow stress variation as a function of temperature. At a constant strain of 0.1, the strength of the solutionized alloy is reduced from ~700 MPa at room temperature to ~500 MPa at 800^{o}C, which is a reduction of ~28%. A similar trend in strength reduction from room temperature to 800^{o}C was observed at plastic strains of 0.2, 0.3, and 0.4 in which the strength of Haynes 282 decreased by ~20%, ~25%, and ~21%, respectively. It was observed that the reduction in strength at temperatures from 25^{o}C to 400^{o}C is less than that from 400^{o}C to 800^{o}C. This may be due to the increased thermal energy which 'softens' the alloy. The work hardening rate in the solutionized condition is graphically depicted in Figure 4.22, which shows that the work hardening capability of Haynes 282 is reduced with an increase in the deformation temperature. The plastic

strain at which the effect of thermal softening overrides that of work hardening is reduced with increases in the loading temperature from ~0.55 at 25ºC to ~0.45 at 800ºC.

During plastic deformation, the evolution of dislocations is characterized by dislocation multiplication during work hardening and dislocation annihilation during softening [169]. The relative ease at which the deformation proceeds at higher temperatures can be attributed to the decrease in activation energy for deformation and greater movement of dislocations in the lattice. Ning et al. [169] reported that high-temperature deformation leads to enhanced dislocation annihilation from thermal activation and diffusion. Also, the nucleation and growth of dynamically recrystallized (DRX) grains may occur during high-temperature deformation [169]. DRX grains increase the rate of dislocation annihilation and could contribute to the reduction in the deformation flow stress at higher temperatures.

(a)

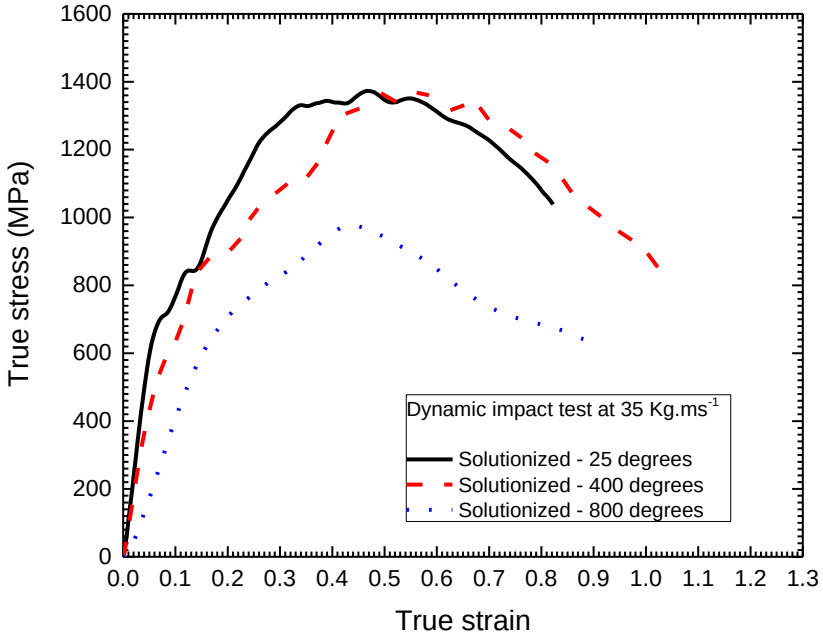

(b)

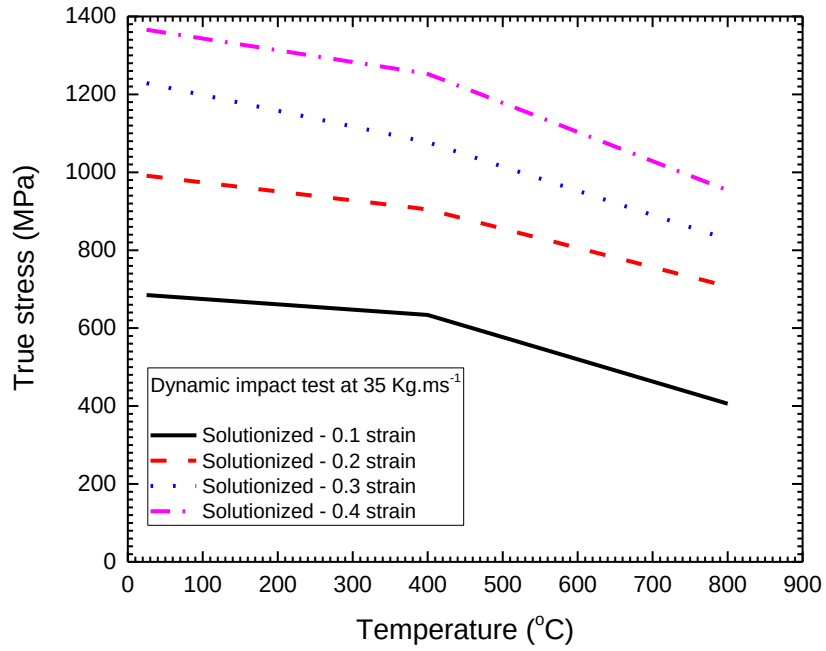

Figure 4.21: (a) True stress vs true strain, (b) Temperature sensitivity plots for dynamic impact behaviour of Haynes 282 from 25°C to 800°C in the solutionized heat treatment condition

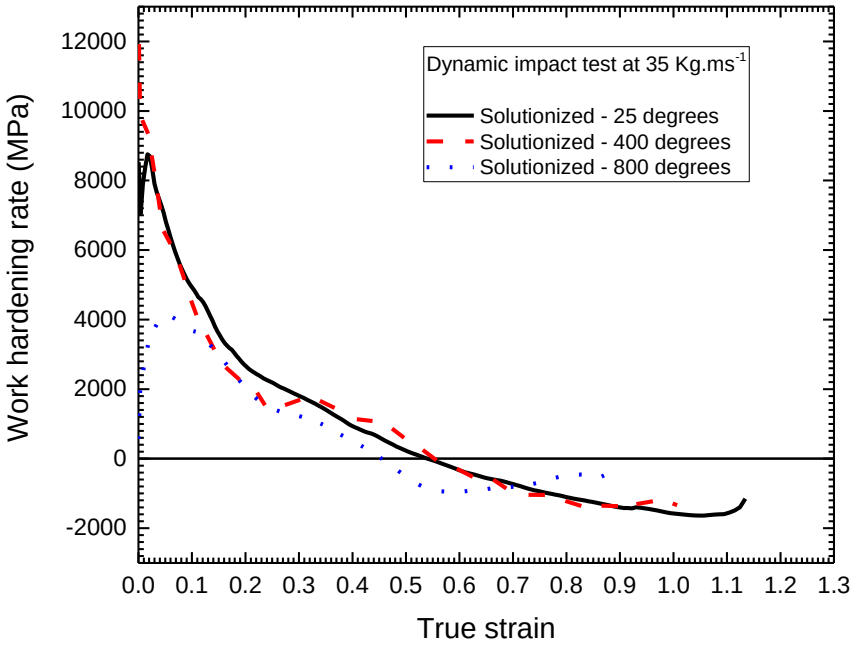

Figure 4.22: Work hardening rate vs true strain for dynamic impact behaviour of Haynes 282 from 25ºC to 800ºC in the solutionized heat treatment condition

4.4.2.2 Special Aged Heat Treatment Condition

The flow curves for the dynamic deformation at high strain rates after the special aged heat treatment are shown in Figure 4.23(a). The true stress vs true strain curves shows that the strength of Haynes 282 after special ageing is a function of temperature. There is an obvious decrease in the flow stress as deformation proceeds from 25^{o}C to 400^{o}C and more stable deformation from 400^{o}C to 800^{o}C as shown in Figure 4.23(b). Greater plastic deformation, up to a strain of 0.6, is observed at 400^{o}C. It is considered that Haynes 282 can undergo more deformation due to increased thermal energy. However, at very high temperatures (800^{o}C), the increased thermal energy could enhance the movement of dislocations within the lattice. In addition, the rapid rate of dislocation annihilation and the increase in heat accumulation in localized regions exacerbate the thermal softening effect thus leading to failure at lower strains of ~0.4. Moreover, transmission electron microscopy examination by Zhang et al. [150] revealed that, above 760 ^{o}C, Orowan looping rather than precipitate shearing, becomes the dominant deformation mechanism during the tensile deformation of Haynes 282 alloy. The work hardening rate against true strain presented in Figure 4.24 shows that Haynes 282 strain hardens the least at very high temperatures in the special aged heat treatment condition.

(a)

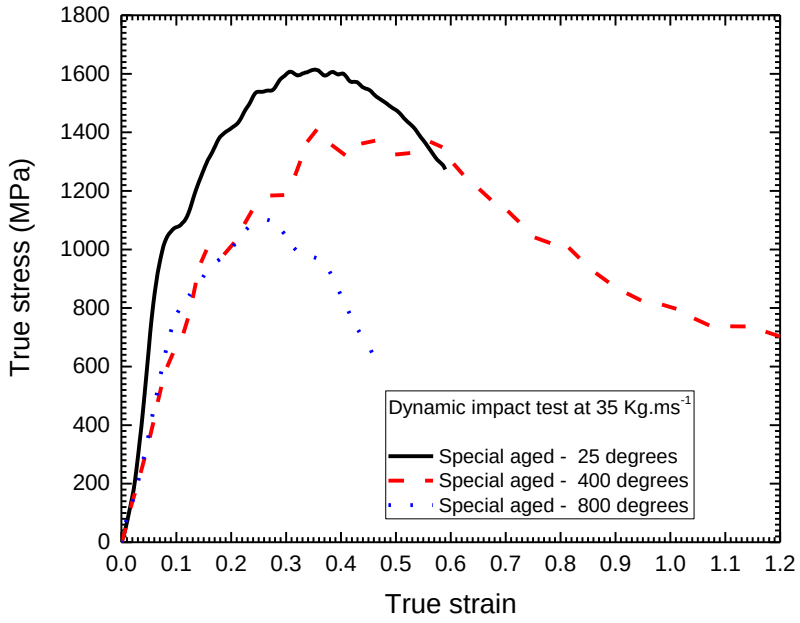

(b)

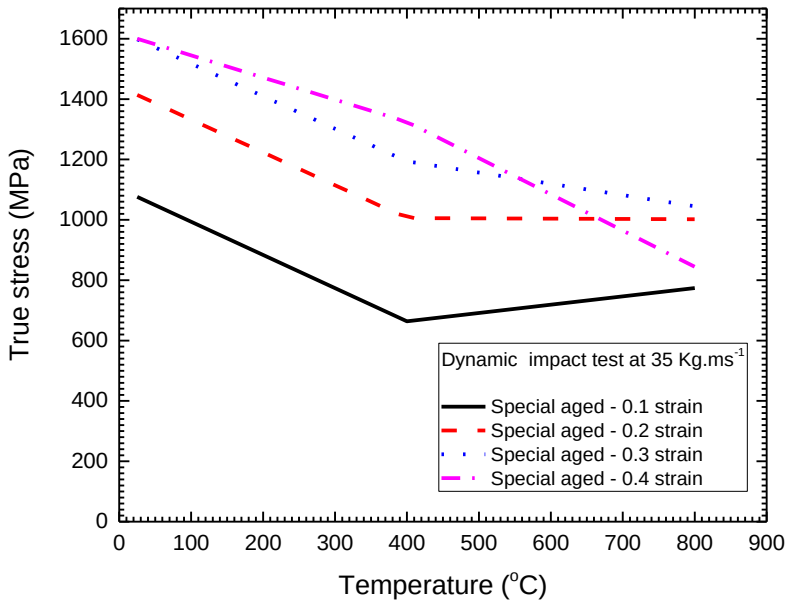

Figure 4.23: (a) True stress vs true strain, (b) Temperature sensitivity plots for dynamic impact behaviour of Haynes 282 from 25°C to 800°C in the special aged heat treatment condition

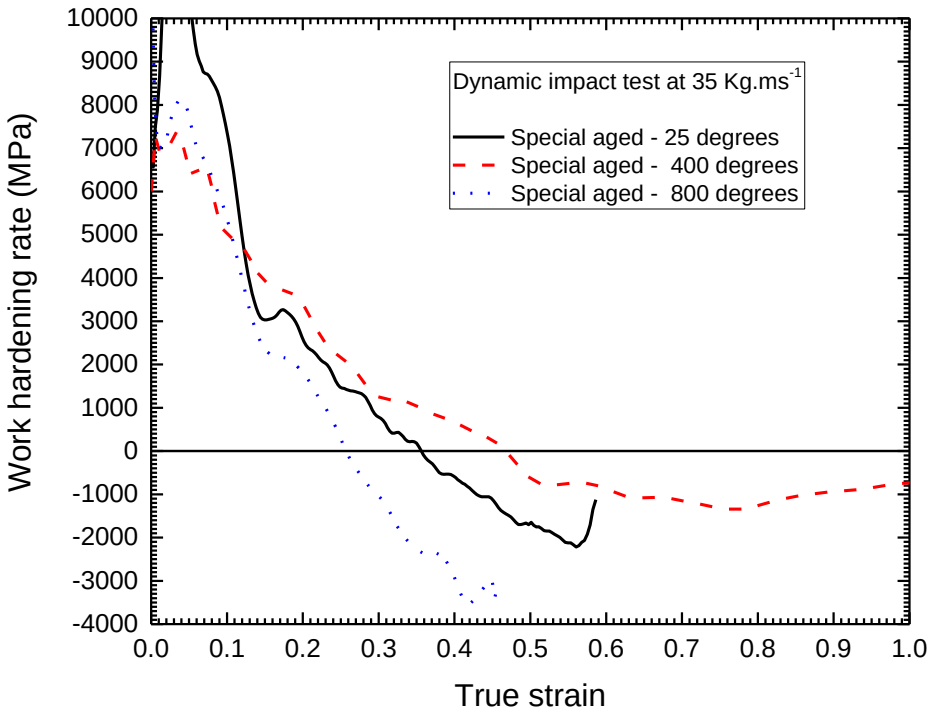

Figure 4.24: Work hardening rate vs true strain for dynamic response behaviour of Haynes 282 from 25°C to 800°C in the special aged heat treatment condition

4.4.2.3 Standard Heat Treatment Condition

The influence of temperature on the dynamic impact behaviour of Haynes 282 after the standard heat treatment is discussed here. Figure 4.25(a) shows the flow stress variation with strain as a function of temperature. Consistent with the observations in the special aged heat treatment condition, the strength of Haynes 282 is decreased with increases in temperature during dynamic impact loading from room temperature to 800^{o}C. At a low strain of 0.1, a linear decrease in the strength of Haynes 282 is observed across the deformation temperatures. As the strain increases, the observed reduction in strength is higher at a temperature range of 25^{o}C – 400^{o}C, and nearly constant from 400^{o}C to 800^{o}C as shown in Figure 4.25(b). However, once the critical deformation strain is reached, a monotonous decline in strength is observed from 25^{o}C to 800^{o}C. This can be attributed to the effect of thermal softening overriding work hardening at higher strains. Strain softening arises from the shearing of the γ' precipitates and increased localized heating that increases the likelihood that Haynes 282 will form ASBs. Once an ASB is formed, plastic deformation is narrowed within the shear band further reducing the strength required to continue deformation. Moreover, the shearing of the ordered γ' precipitates by superlattice dislocations results in the loss of order strengthening in the alloy. The plotted work hardening rate against true strain in Figure 4.26 shows an inverse relationship between work hardening rate and temperature. As the deformation temperature increases, the alloy begins to lose its strain hardening capability due to the temperature softening effect.

(a)

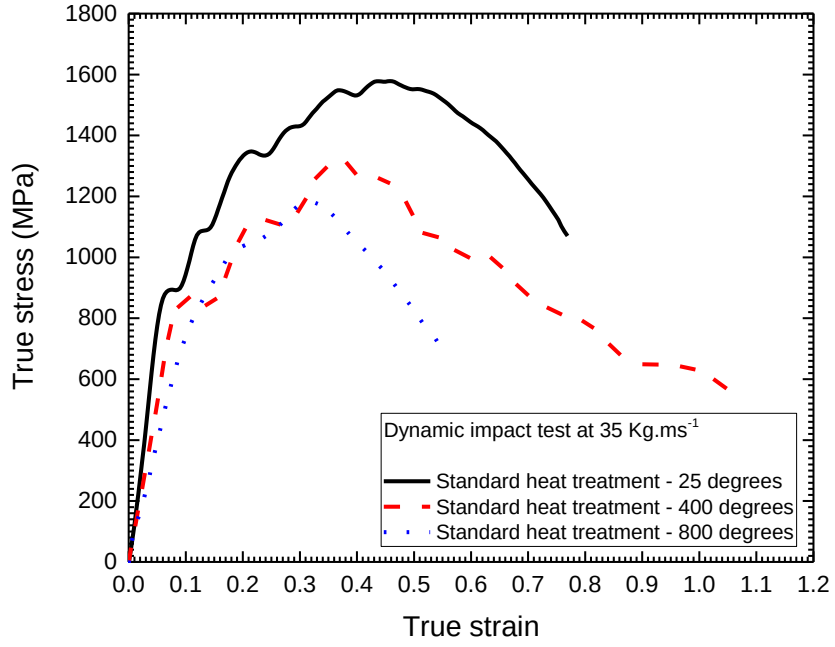

(b)

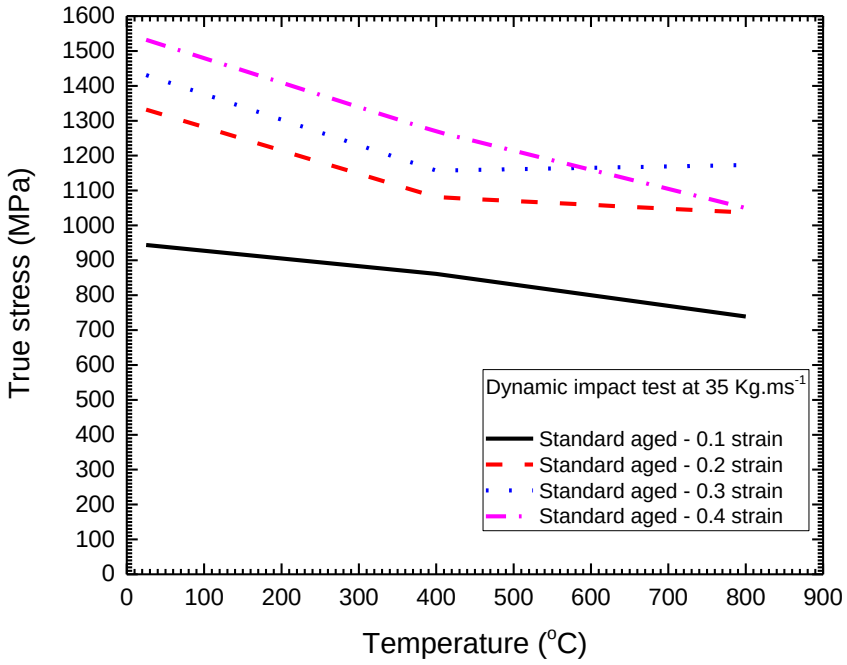

Figure 4.25: (a) True stress vs true strain, (b) Temperature sensitivity plots for dynamic impact behaviour of Haynes 282 from 25ºC to 800ºC in the standard heat treatment condition

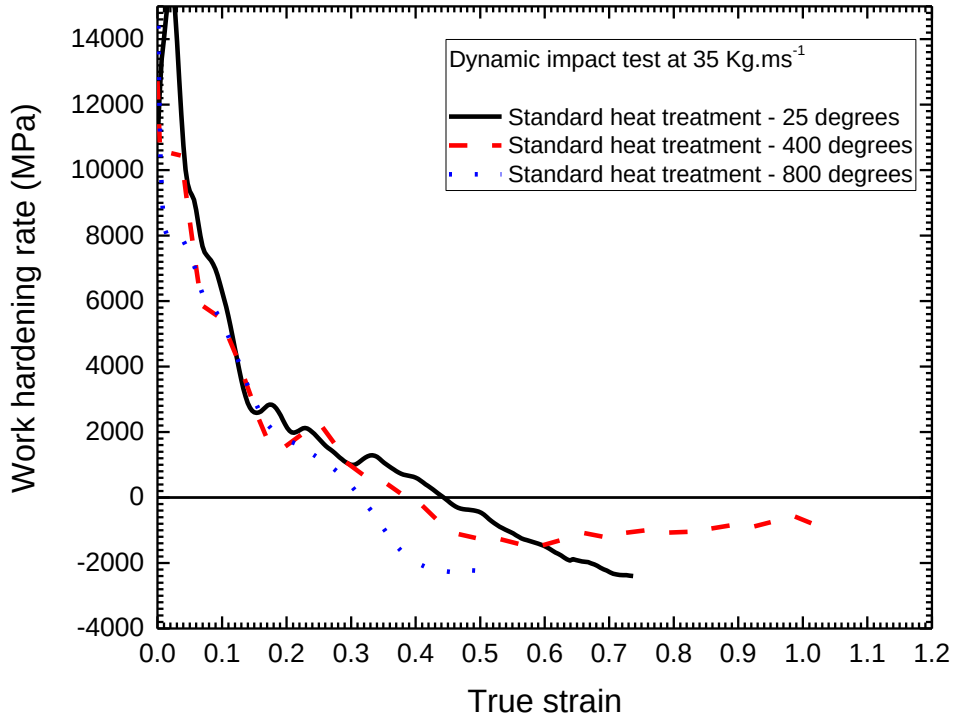

Figure 4.26: Work hardening rate vs true strain for dynamic response behaviour of Haynes 282 superalloy from 25^{o}C to 800^{o}C after standard heat treatment

4.4.3 Comparison of Effect of Temperature on Dynamic Impact Behaviour in the Aged and Solutionized Heat Treatment Conditions

In this section, the observed dynamic impact behaviour of Haynes 282 is compared for temperatures that range from 25^{o}C to 800^{o}C and impact momentum of 35 Kg.ms^{-1}. As mentioned earlier, the deformation temperature and strain rate have a significant effect on the dynamic impact behaviour of Haynes 282 in the three heat treatment conditions used in this study. It is observed that the flow stress of the alloy decreases or remains almost constant with increases in the strain rate and temperature. Temperature has a more pronounced effect than the strain rate on deformation behaviour. This results from the greater ease of dislocation movement with an increase in temperature. The solutionized heat treatment condition (Figure 4.27(a)) shows a consistent decrease in flow stress from room temperature to 800^{o}C at all plastic strains. This contrasts with the special aged condition, which at strains up to 0.3, shows a decrease in the flow stress as the temperature is increased from 25^{o}C to 400^{o}C, and thereafter, a near constant flow stress as Haynes 282 is deformed from 400^{o}C to 800^{o}C. In the standard heat treatment condition, there is less reduction in the deformation strength, compared with the special aged condition, from room temperature to 400^{o}C, and a near constant flow stress, as observed for the special aged condition, from 400^{o}C to 800^{o}C. There appears to be an anomalous behaviour in the deformation behaviour at 400^{o}C, namely more extensive deformation and higher work hardening rate, with the effect being more pronounced in the special aged heat treatment condition. This is likely due to the strong dynamic strain aging effect observed in Haynes 282 at 400^{o}C [170]. The increased cyclic hardening during dynamic strain aging was attributed to the temporary immobilization of mobile dislocations due to repeated locking and un-locking of dislocations by solute atoms, which led to

an increased dislocation density [170]. Dynamic strain aging has the tendency to increase the work hardening rate of a material [171].

The temperature sensitivity of Haynes 282 during dynamic deformation increases at a higher strain above 0.4, with the effect being more pronounced in the special aged heat treatment that shows a monotonous decrease in the strength of the alloy from 25^{o}C to 800^{o}C as shown in Figure 4.27(a). This may be due to increased adiabatic heating from localized temperature increase and continuous shearing of the ordered γ' precipitates at higher strains. Dissolution of the second phase precipitates in the ASBs due to strain-enhanced diffusion has been reported in the literature as a major contributor to the observed softening effect [172]. Moreover, the effect occurred at strains beyond the peak stress at which stage mechanical instability due to thermal softening dominates the deformation mechanism.

The work hardening rate in Figure 4.27(b) shows that Haynes 282 in the solutionized condition strain hardened at a higher rate, followed by the standard heat treatment condition, and lastly, the special aged condition. In addition, it is observed that the strain hardening capability across the three heat treatment conditions decreases with an increase in temperature. Although it may be expected that the strength of Haynes 282 will decrease with increases in temperature due to the increased rate of dislocation annihilation provided by the thermal energy of deformation, however, as the deformation temperature is increased beyond 400^{o}C, no appreciable loss in strength is observed. This observation at elevated temperatures may be attributed to the assertion by some academics [5], [7] that Haynes 282 has excellent thermal stability at high temperatures due to the absence of deleterious phases, such as sigma, Laves, and mu, and resistance to γ' coarsening in the alloy. Similarly, in a comparative study of the thermomechanical behaviour of Inconel 718, Allvac 718Plus, and Haynes 282 above 700^{o}C, Huber et al. [173] observed that Haynes 282 shows no

transformation, but only slight coarsening of the γ′ precipitates. The authors concluded that the outstanding performance of Haynes 282 is due to the stability and distribution of grain boundary carbides that retard softening by recrystallization.

Within the limits of the temperatures, strain rates, and strains studied, Haynes 282 shows a near constant to negative strain rate sensitivity with flow stress at room and elevated temperatures, a remarkable feature that could ease the formability of this alloy.

(a)

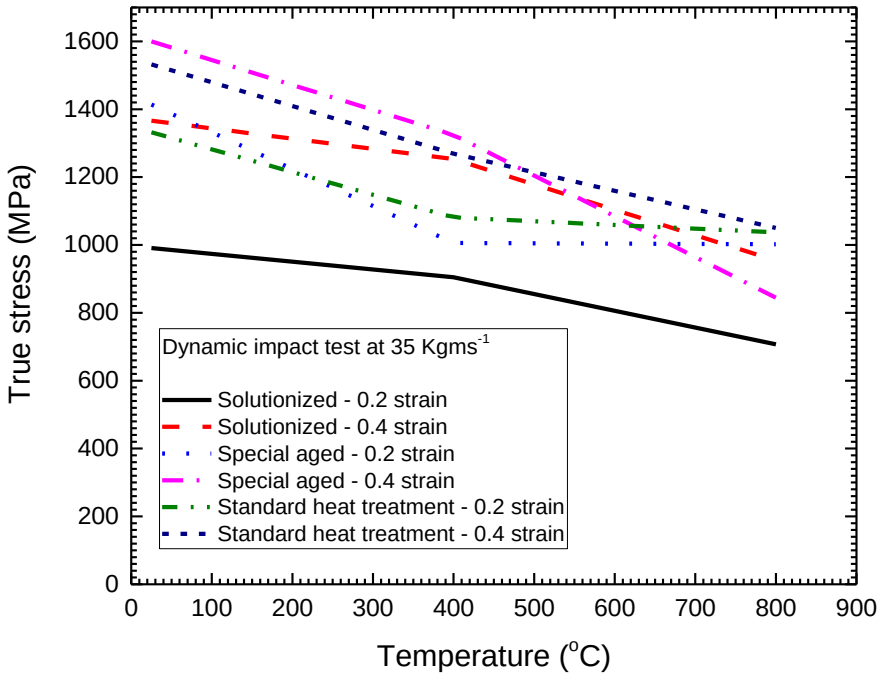

(b)

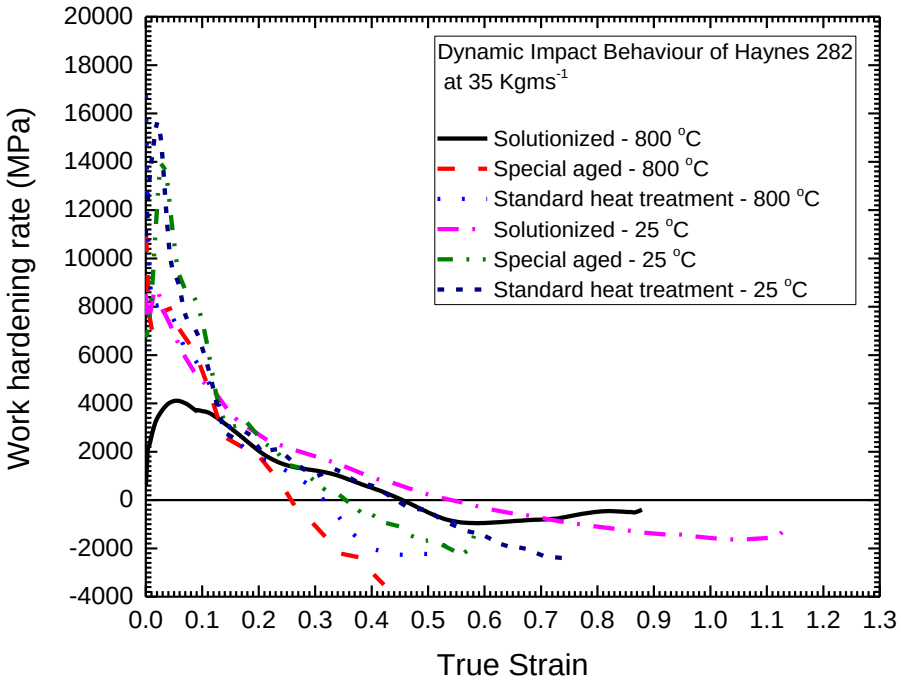

Figure 4.27: (a) Temperature sensitivity, (b) Work hardening rate vs true strain plots for the dynamic impact behaviour of Haynes 282 from 25°C to 800°C in the three heat treatment conditions

4.4.4 Likelihood that Haynes 282 forms Adiabatic Shear Bands

In this section, the likelihood of Haynes 282 to form ASBs in the solutionized, special aged, and standard heat treatment conditions that invariably leads to failure during dynamic impact loading is discussed. This likelihood is influenced by the mechanical properties of Haynes 282, such as compressive strength and strain hardening capability that predisposes this alloy to ASB formation.

There are several assumptions on the critical conditions necessary for the formation of ASBs during impact loading. Nevertheless, it is widely acknowledged in the literature that the tendency for shear localization increases with increases in strength and decreases in the strain hardening capability of an alloy [22], [174]–[178]. This was validated by Li et al. [179] who found remarkable resistance to adiabatic shear failure in a high entropy alloy deformed under high strain rate loading. The resistance of the high entropy alloy was attributed to its excellent strain hardening capability. Similarly, in a study of the ballistic behaviour of Inconel 718, Pereira and Lerch [18] observed that the annealed material with lower strength and higher ductility has better impact energy absorbing properties than the aged material. The aged Inconel 718 alloy that has a higher strength and moderate elongation showed narrow shear bands along which further deformation was restricted, thus leading to catastrophic failure.

It is observed in this study that solutionizing leads to the lowest strength and greatest strain hardening capability that suppresses the formation of ASBs during dynamic impact deformation. In contrast, aging leads to higher strength and limited strain hardening that causes localized deformation in Haynes 282. In the aged conditions, the special aged heat treatment increases the likelihood of failure as opposed to the standard heat treatment as it leads to higher strength and reduced strain hardening. Consistent with the observation made for quasi-static compressive

deformation, the higher strength after the special aged heat treatment may be attributed to the different mechanisms of dislocation-precipitate interaction compared to the standard heat treatment. As previously discussed, the larger precipitates (40 – 60 nm) after special aged heat treatment could increase the critical resolved shear stress required for dislocations to shear the precipitates, which leads to reduced strain hardening capability and increased compressive strength. In contrast, the smaller precipitates (15 – 30 nm) observed in the standard heat treatment condition could provide less resistance to precipitate shearing by moving dislocations, thus leading to a reduction in the strength of the material and an increase in the strain hardening capability. This correlates with the findings in [17], [168], and [169] that a precipitate that strengthens a material under quasi-static or low strain rate deformation promotes strain localization during impact deformation with an attendant decrease in the strain hardening capability of the material. The localization of plastic flow promotes the formation of ASBs which 'softens' the material. Table 4.2 shows the likelihood that Haynes 282 will form ASBs in impact deformation at room temperature. It can be observed that the solutionized condition shows no evidence of cracks up to the maximum impact momentum applied in this study. This attests to the higher strain hardening capability of Haynes 282 in the solutionized condition that suppresses the formation of ASBs.

When materials are deformed at large strains and high strain rates, their plastic flow has a limited amount of time to evolve and due to inhomogeneous deformation, regions of localized strain are formed. The temperature increase in the material, from the conversion of plastic work of deformation into entrapped heat, is concentrated in these localized regions at points of maximum shear stress [182]. The accumulated heat cannot be readily conducted away from the localized region within the limited timescale of the deformation (usually in the order of 50 – 200μs).

Table 4.3: Susceptibility of Haynes 282 to ASB formation in impact deformation at room temperature for different heat treatments

Type of heat treatment	**Impact momentum ($Kg.ms^{-1}$)**	**Condition of sample after impact**	**Likelihood of forming ASBs**
Solutionized	27	No fractures	Low
	35	No fractures	Low
	47	No fractures	Low
Standard heat treatment	27	No fractures	Moderate
	35	No fractures	Moderate
	47	Fractured	Moderate
Special aged	27	No fractures	High
	35	Fractured	High
	47	Fractured	High

As such, the ballistic energy associated with the deformation has to be rapidly dissipated by some other means, such as temperature increases in the material [182]. The localized temperature increase in the shear bands can be very high, which could possibly lead to melting or evolution of the microstructure into ultra-fine grains from dynamic recrystallization, which causes thermal instability and catastrophic failure [183], [184].

To understand the role of ASBs in the failure of Haynes 282 under impact loading, optical and scanning electron microscopies of the shear bands formed in the special aged were carried out. The optical microscopy micrograph in Figure 4.28 shows an ASB with a width of ~2μm that causes crack formation and subsequent failure of the material. Upon further examination of this ASB with the FEI Nova NanoSEM 450, it was observed that the precipitates in the ASB have dissolved and the precipitates near the ASB have been severely sheared; see Figure 4.29(b). Two mechanisms are suggested that could explain the instantaneous dissolution of the γ′ precipitates during dynamic impact deformation. One is adiabatic heating that arises from the conversion of plastic work into undissipated heat in the material (aided by shearing of the γ′ precipitates) and the second mechanism is strain-enhanced diffusion. It is worth noting that these mechanisms are complementary and the occurrence of one could lead to or exacerbate the effect of the other.

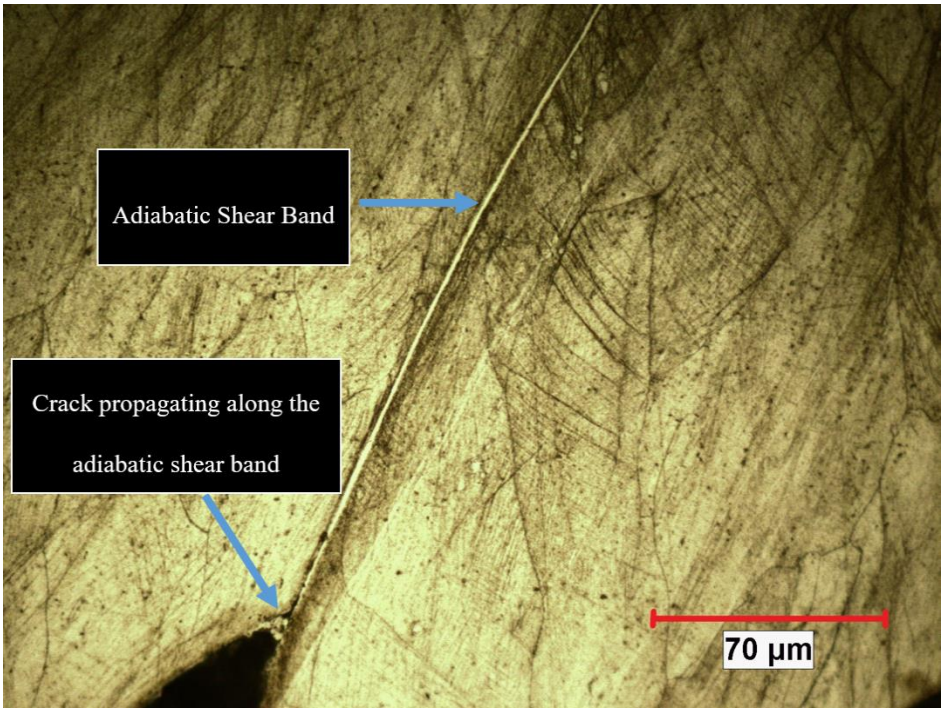

Figure 4.28: Optical microscopy micrograph of Haynes 282 in the special aged condition, deformed at room temperature and strain rate of 3,300/s which show adiabatic shear band

(a)

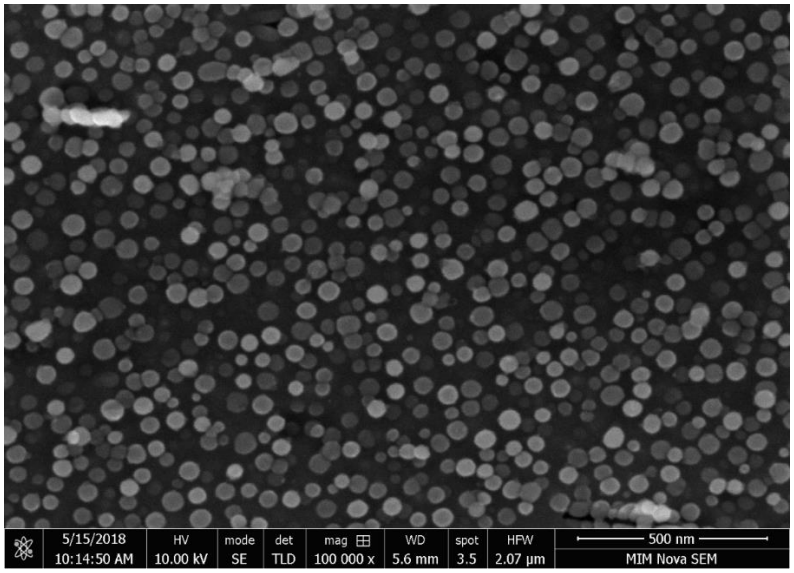

(b)

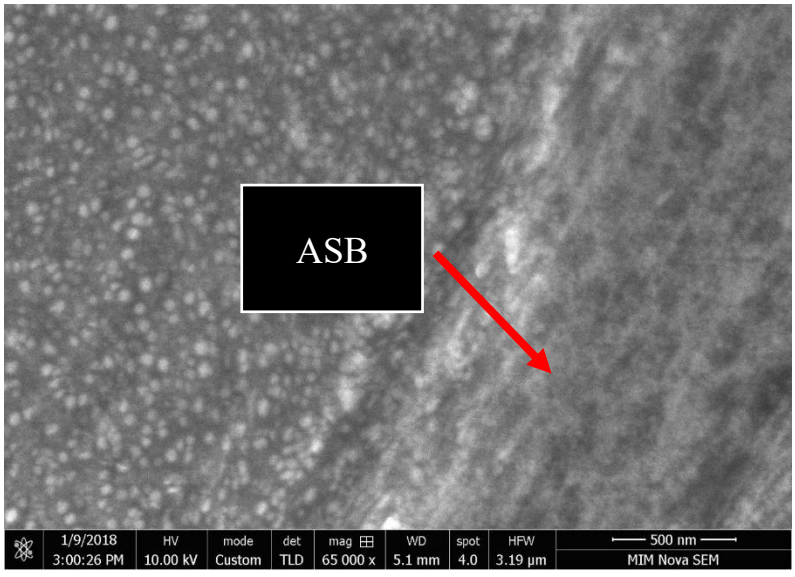

Figure 4.29: Micrograph taken with FEI Nova NanoSEM 450 of Haynes 282 after special aged heat treatment: (a) undeformed condition (b) deformed at room temperature and strain rate of 3,300/s that shows dissolved γ′ precipitates in the adiabatic shear band

4.4.4.1 Precipitate Dissolution arising from Heat Accumulation

Localized plastic flow causes a high degree of localized shear strain in the ASBs which is estimated to be between 2 and 6 [185]. The temperature increase inside the ASBs during plastic deformation has been estimated using different methods based on the assumption that nearly all the work of plastic deformation is converted into heat. However, approximately 15 percent of the plastic work was estimated to be retained as latent energy after deformation in [186]. The adiabatic temperature increase during impact deformation can be estimated by using [187]:

$$\Delta T = \frac{\beta}{\rho C_P} \int_0^{\varepsilon_f} \sigma d\varepsilon \qquad (4.2)$$

where β is the Taylor–Quinney coefficient that denotes the amount of plastic work converted into heat during deformation, ρ is the material density, C_P denotes the specific heat of the material, σ is the experimentally measured flow stress, and ε_f is the corresponding true strain. It should be noted that Equation 4.2 could be used to measure the temperature increase in an entire sample, but under-estimates the temperature rise inside the ASBs since the equation relies on the plastic strain measured in the bulk sample and not inside the ASBs.

To address this deficiency, Liu et al. [188] measured the geometry of the elongated grains after impact deformation to calculate the shear strain in the ASBs, which they concluded to be between 2 and 3. Li et al [189] applied a conservative shear strain of 1 to 2 in their study on AISI 52100 to estimate the temperature increase in the ASBs. Wang [190]–[192] adopted a gradient-dependent plasticity model to compute the average temperature increase in the ASBs. Clos et al. [193], Guduru et al. [194], and Cho et al. [195] successfully carried out in-situ temperature measurements with the use of an infrared detector to record the temperature increase in the ASBs. Therefore, consistent with the experimentally measured bulk plastic strain during deformation, a conservative

shear strain of 2 to 3 in the ASBs is assumed in this study in the special aged condition and the fraction of plastic work converted into heat is taken to be 0.9 [187]. Calculations carried out with Equation 4.2 estimate the temperature increase in the ASBs in the special aged condition deformed at room temperature with a strain rate of 3,300/s to be between 804^{o}C and 1206^{o}C, whilst the temperature increase in the bulk sample is ~142^{o}C. The calculated temperature increase in the ASBs is well above 997^{o}C which is the solvus (dissolution) temperature of the γ′ precipitates in Haynes 282 [5]. This partly explain for the instantaneous dissolution of the γ′ precipitates in the ASBs during deformation at high strain rates.

4.4.4.2 Precipitate Dissolution arising from Strain-Enhanced Diffusion

The concept of strain-enhanced diffusion discussed in [196]–[201] has re-emerged recently in [172], [202], [203] to explain for the dissolution of second phase particles in the ASBs during plastic deformation at high strain rates. The results of the modeling of kinetic dissolution by short-circuiting the diffusion of mobile dislocations in Yang et al. [172] could be applied here to partly explain for the observed instantaneous dissolution of the γ′ precipitates in the ASBs.

During deformation at high strain rates, the γ′ precipitates are continuously cut by advancing dislocations to overcome the barriers necessary for plastic deformation. As more dislocations approach and shear the precipitates, it becomes much easier for slip to continue along this active plane than been transferred to a neighboring inactive slip system. Under the prevailing high strain rate deformation conditions, there is the rapid generation and multiplication of dislocations, which results in the pile-up of these dislocations around the sheared γ′ precipitates. This then causes the dissolution of the precipitate atoms into the stationary dislocations core. Since dislocations are highly mobile during impact deformation, the dissolved atoms will be swept away by moving

dislocations thus giving rise to precipitate free zones. Thus, dislocation motion contributes to the diffusion process which is otherwise known as “dislocation-assisted diffusivity” [196]. Cohen [196] noted that the deformation strain rate must be sufficiently high and/or the deformation temperature sufficiently low for diffusion enhancement by dislocations to prevail. Strain-enhanced diffusion can be suppressed if recrystallization occurs during deformation and results in low dislocation density [196].

Since the tendency for strain localization increases with an increase in strength and decrease in work hardening, it is asserted within the limits of the strain rates and temperatures investigated in this study that under dynamic impact loading, Haynes 282 is most susceptible to impact damage in the special aged heat treatment condition, followed by the standard heat treatment condition, and least susceptible after solutionized heat treatment. This alloy is most amenable to forming operations after solutionizing; thereafter, the component should be aged for improved high-temperature mechanical strength through the precipitation of γ' hardening particles.

4.5 Constitutive Modeling of the Dynamic Impact Behaviour of Haynes 282

This section presents the constitutive equation based on the Arrhenius-type model to predict the dynamic impact behaviour of Haynes 282 in the solutionized, standard heat treatment, and special aged heat treatment conditions. The Arrhenius-type model was selected as it fits the experimental data better than the JC and modified JC models. Moreover, the JC model relies on the uncoupled effect of strain rate, strain hardening, and temperature to predict the flow behaviour of a material during deformation. As is pertinent during impact deformation, there is an obvious coupling effect amongst these deformation parameters. An ideal constitutive model to predict the dynamic impact behaviour of a material should have the ability to describe the coupled effects of the strain rate,

temperature, and strain rate hardening/softening phenomenon. However, development of such a model is a challenging and almost impossible task [204]. As such, assumptions may be necessary to simplify the model based on the application requirements.

4.5.1 Modeling Work Hardening Behaviour – Special Aged Heat Treatment Condition

The flow stress of a material during the work hardening-dynamic recovery stage can be modeled by using the following expression [205]:

$$\frac{\sigma}{\sigma_p} = \left[\frac{\varepsilon}{\varepsilon_p}\exp\left(1-\frac{\varepsilon}{\varepsilon_p}\right)\right]^{c_1} \qquad (4.3)$$

where σ_p represents the peak stress (MPa), ε_p is the peak strain, c_1 is a material constant which is weakly dependent on temperature and strain rate [205], σ is the flow stress and ε is the corresponding strain during deformation. The peak stress is related to the deformation strain rate by using a hyperbolic-sine Arrhenius equation [206], [207]:

$$\dot{\varepsilon} = AF(\sigma_p)\exp\left(-\frac{Q}{RT}\right) \qquad (4.4)$$

$$F(\sigma_p) = \begin{cases} \sigma_p^n & \alpha\sigma_p < 0.8 \\ \exp(\beta\sigma_p) & \alpha\sigma_p > 1.2 \\ [\sinh(\alpha\sigma_p)]^n & \text{for all } \sigma_p \end{cases} \qquad (4.5)$$

where $\dot{\varepsilon}$ is the strain rate (s^{-1}), T is the absolute deformation temperature (K), R is a universal gas constant (8.31 J mol^{-1} K^{-1}), and Q represents the activation energy of the deformation process (kJ mol^{-1}). A, α, β, and are experimentally determined constants, with $\alpha = \beta/n$. The coupled effects of temperature and strain rate have been widely represented [207]–[210] by using a Zener–Hollomon parameter (Z), and the peak flow stress during deformation can be determined by using the Z parameter as:

$$\sigma_p = \frac{1}{\alpha}\ln\left\{\left(\frac{Z}{A}\right)^{1/n} + \left[\left(\frac{Z}{A}\right)^{2/n} + 1\right]^{1/2}\right\} \qquad (4.6)$$

$$Z = \dot{\varepsilon}\exp(Q/RT) \qquad (4.7)$$

To obtain the parameters for Equation 4.4, $F(\sigma_p)$ from Equation 4.5 are substituted into Equation 4.4, and the natural logarithm of both sides are taken to yield:

$$\ln(\sigma_p) = \frac{1}{n}\ln(\dot{\varepsilon}) - \frac{1}{n}\ln(B) \qquad (4.8)$$

$$\sigma_p = \frac{1}{\beta}\ln(\dot{\varepsilon}) - \frac{1}{\beta}\ln(B') \qquad (4.9)$$

$$\ln[\sinh(\alpha\sigma_p)] = \frac{Q}{nRT} - \frac{\ln A}{n} + \frac{\ln\dot{\varepsilon}}{n} \qquad (4.10)$$

where B and B′ are temperature-independent material constants. The values of n and β were obtained from the slopes of $\ln\sigma_p$ vs $\ln\dot{\varepsilon}$ and σ_p vs $\ln\dot{\varepsilon}$ plots, respectively, as shown in Figure 4.30 and Figure 4.31. The samples were deformed at an impact momentum of 27, 35, and 47 Kg.ms^{-1} using a sample aspect ratio of 1.0. No influence of the sample size on the alloy flow stress was observed experimentally, only an increase in the strain rate with decreasing sample aspect ratio following the expression in Equation 4.11. This assumption will allow the use of a constant aspect ratio during simulation of the dynamic impact behaviour of Haynes 282.

$$\dot{\varepsilon} = \left(-\frac{2C_o}{L}\right) * \varepsilon_t \qquad (4.11)$$

The average values of n and β are -5.617 and -0.00436966, respectively; see Figure 4.30 and Figure 4.31. $\alpha = \beta/n$ becomes 0.00077794. Substituting the experimentally obtained peak stresses at different deformation temperatures and strain rates, and the derived value of α into Equation 4.10,

$\ln[\sinh(\alpha\sigma_p)]$ is plotted against $\ln\ \dot{\varepsilon}$ in Figure 4.32 that gives the updated n value as -4.228. The constant Q is obtained by differentiating Equation 4.10 to give:

$$Q = nR\frac{d\{\ln[\sinh(\alpha\sigma_p)]\}}{d(1/T)} \qquad (4.12)$$

From the slope of the $\ln[\sinh(\alpha\sigma_p)]$ versus 1/T plots at different strain rates shown in Figure 4.33, the average value of Q and A can be derived as -7.077 KJ/mole and 1342.75/s, respectively.

The peak strain during dynamic impact deformation depends on the deformation strain rate and temperature [208], and can be expressed as:

$$\varepsilon_p = kZ^{n'} \qquad (4.13)$$

Taking the natural logarithm of both sides in Equation 4.13 yields:

$$\ln\varepsilon_p = n'\ln Z + \ln k \qquad (4.14)$$

K and n' are material constants obtained as 0.1248053444 and 0.1542 from the slope and intercept of the plotted $\ln\varepsilon_p$ against $\ln Z$, respectively, as shown in Figure 4.34.

Based on the above analysis, the peak flow stress and peak strain of Haynes 282 in the special aged heat treatment condition can be derived by using:

$$\begin{cases} \sigma_p = \frac{1}{0.00077794}\ln\left\{\left(\frac{Z}{1342.75}\right)^{1/(-4.228)} + \left[\left(\frac{Z}{1342.75}\right)^{2/(-4.228)} + 1\right]^{1/2}\right\} \\ \varepsilon_p = 0.1248053444 \times Z^{0.1542} \\ Z = \dot{\varepsilon}\exp\left(\frac{-7077}{RT}\right) \end{cases} \qquad (4.15)$$

The coupled effect of the deformation strain rate and temperature on the material constant c_1 is obtained by taking the natural logarithm of Equation 4.3 to give:

$$ln\left(\frac{\sigma}{\sigma_p}\right) = c_1\left[ln\left(\frac{\varepsilon}{\varepsilon_p}\right) + \left(1 - \frac{\varepsilon}{\varepsilon_p}\right)\right] \quad (4.16)$$

The peak stress and peak strain for Equation 4.16 are calculated by using Equation 4.15, and thereafter substitute the experimentally measured flow stresses and the corresponding strains during the work hardening-dynamic recovery period into Equation 4.16. The values of C_1 for all deformation temperatures and strain rates are obtained by using the plotted $ln\left(\frac{\sigma}{\sigma_p}\right)$ against $\left[ln\left(\frac{\varepsilon}{\varepsilon_p}\right) + \left(1 - \frac{\varepsilon}{\varepsilon_p}\right)\right]$. The linear relationship among the deformation temperature, strain rate, and material constant, C_1 is then derived by using the ln C_1 – ln Z plot as shown in Figure 4.35. The intercept and slope of the line of best fit obtained are 0.5858 and -0.0782, respectively, and the material constant c_1 can be expressed as:

$$C_1 = 0.5858Z^{(-0.0782)} \quad (4.17)$$

4.5.2 Modeling Flow Softening Behaviour – Special Aged Heat Treatment Condition

During the dynamic impact deformation of materials, the effects of strain hardening, dynamic recovery softening, and dynamic recrystallization softening often coexist [211]. The effect of thermal softening can override that of strain hardening, which results in mechanical instability. Several methods, such as the Avrami kinetics of dynamic recrystallization, have been used to study the dynamic impact behaviour of materials beyond the work hardening-dynamic recovery stage [209], [211], [212]. In this study, the methodology in [208] is adopted by extending the constitutive relationship of Equation 4.3 to describe the dynamic softening behaviour of Haynes 282 as shown in Equation 4.18, where C_2 is a material constant which is weakly dependent on the deformation temperature and strain rate [205].

$$\frac{\sigma}{\sigma_p} = \left[\frac{\varepsilon}{\varepsilon_p} exp\left(1 - \frac{\varepsilon}{\varepsilon_p}\right)\right]^{c_2} \qquad (4.18)$$

Taking the natural logarithm of both sides in Equation 4.18 gives:

$$ln\left(\frac{\sigma}{\sigma_p}\right) = c_2\left[ln\left(\frac{\varepsilon}{\varepsilon_p}\right) + \left(1 - \frac{\varepsilon}{\varepsilon_p}\right)\right] \qquad (4.19)$$

Due to the large scatter in the data points during the dynamic softening stage, the value of C_2 at a fixed strain of 0.3 was obtained at all deformation temperatures and strain rates by plotting $\ln\left(\frac{\sigma}{\sigma_p}\right)$ against $\left[\ln\left(\frac{\varepsilon}{\varepsilon_p}\right) + \left(1 - \frac{\varepsilon}{\varepsilon_p}\right)\right]$. Similar to the procedure used to obtain C_1, the peak stress and peak strains for Equation 4.19 were calculated by using the expression in Equation 4.15. The relationship among the deformation temperature, strain rate, and material constant, C_2, were evaluated by using the ln C_2 – ln Z plot as shown in Figure 4.36. Linear regression fitting gives the intercept and slope as 1.9707 and -0.1056 respectively, and the material constant C_2 for all the experimental conditions can be expressed as:

$$C_2 = 1.9707Z^{(-0.1056)} \qquad (4.20)$$

Based on the strength of the above analysis, the following Arrhenius-type constitutive model is developed to predict the dynamic impact behaviour of Haynes 282 in the special aged condition.

$$\begin{cases} \dfrac{\sigma}{\sigma_p} = \left[\dfrac{\varepsilon}{\varepsilon_p} exp\left(1 - \dfrac{\varepsilon}{\varepsilon_p}\right)\right]^{c} \\ \sigma_p = \dfrac{1}{0.00077794} ln\left\{\left(\dfrac{Z}{1342.75}\right)^{1/(-4.228)} + \left[\left(\dfrac{Z}{1342.75}\right)^{2/(-4.228)} + 1\right]^{1/2}\right\} \\ \varepsilon_p = 0.1248053444 * Z^{0.1542} \\ Z = \dot{\varepsilon}\, exp\left(\dfrac{-7077}{RT}\right) \\ c = \begin{cases} 0.5858Z^{(-0.0782)} & \text{(for work hardening – dynamic recovery stage)} \\ 1.9707Z^{(-0.1056)} & \text{(for dynamic flow softening stage)} \end{cases} \end{cases} \qquad (4.21)$$

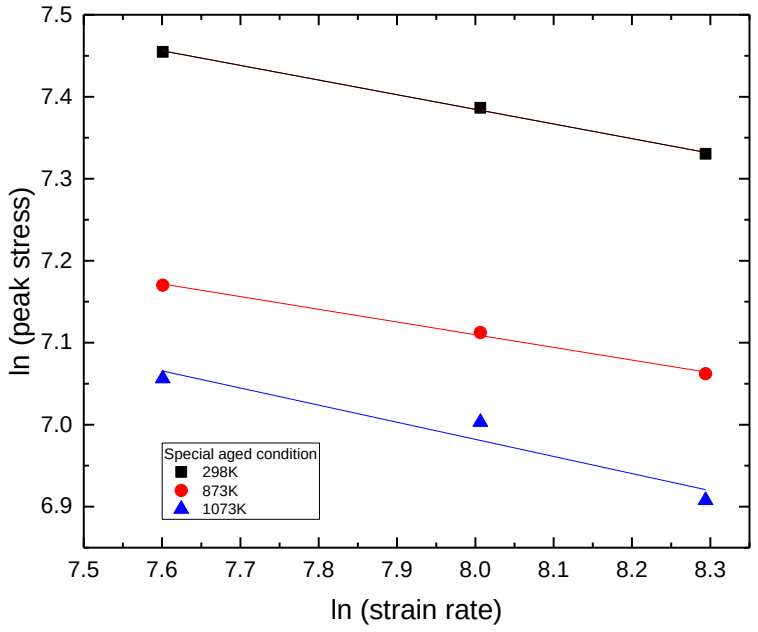

Figure 4.30: ln (σ_p) plotted against ln ($\dot{\varepsilon}$) for special aged heat treatment

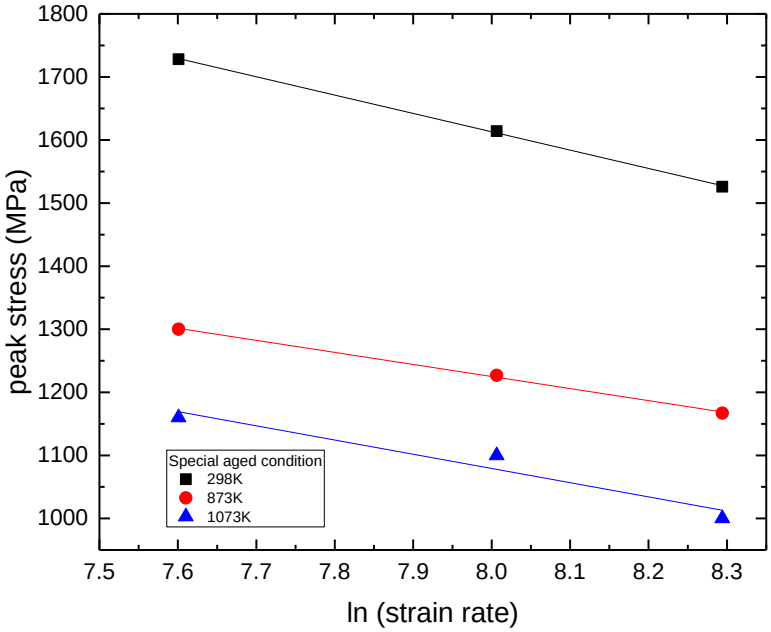

Figure 4.31: σ_p plotted against ln ($\dot{\varepsilon}$) for special aged heat treatment

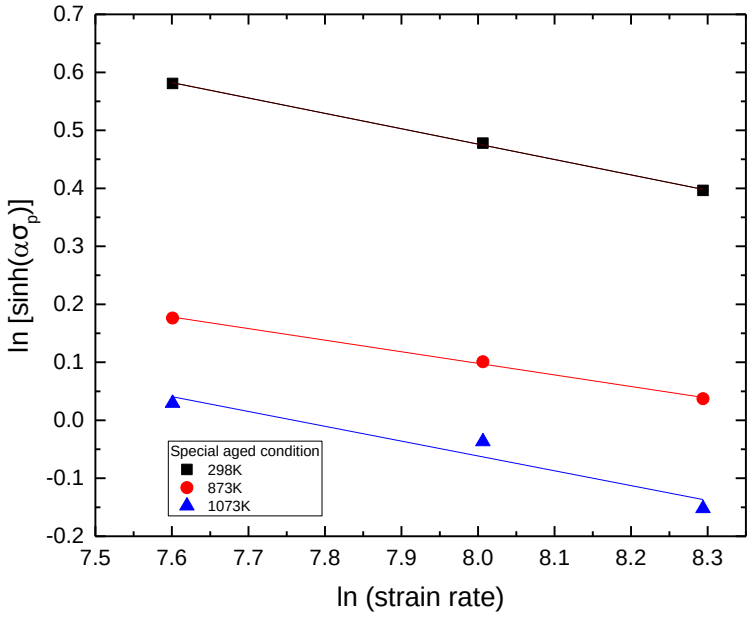

Figure 4.32: ln [sinh ($\alpha\sigma_p$)] plotted against ln ($\dot{\varepsilon}$) for special aged heat treatment

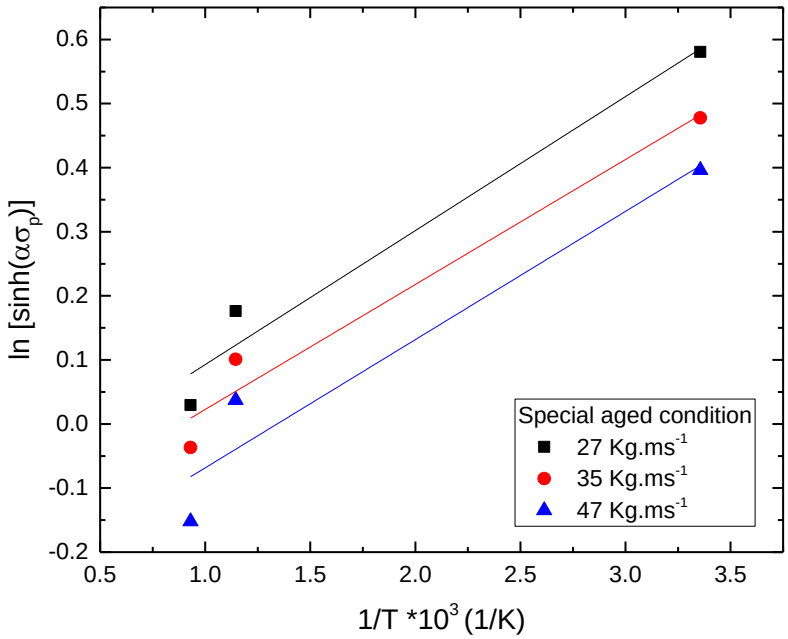

Figure 4.33: ln [sinh ($\alpha\sigma_p$)] plotted against 1/T for special aged heat treatment

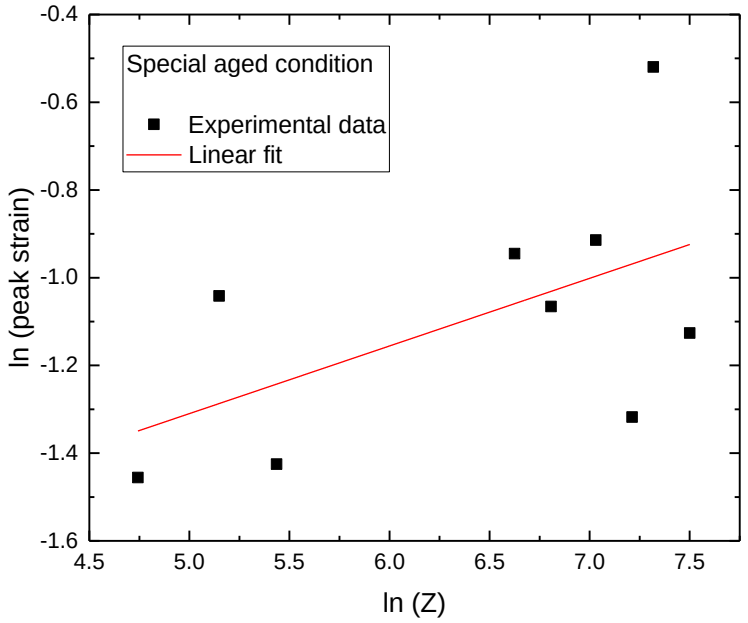

Figure 4.34: ln (σ_p) plotted against ln (Z) for special aged heat treatment

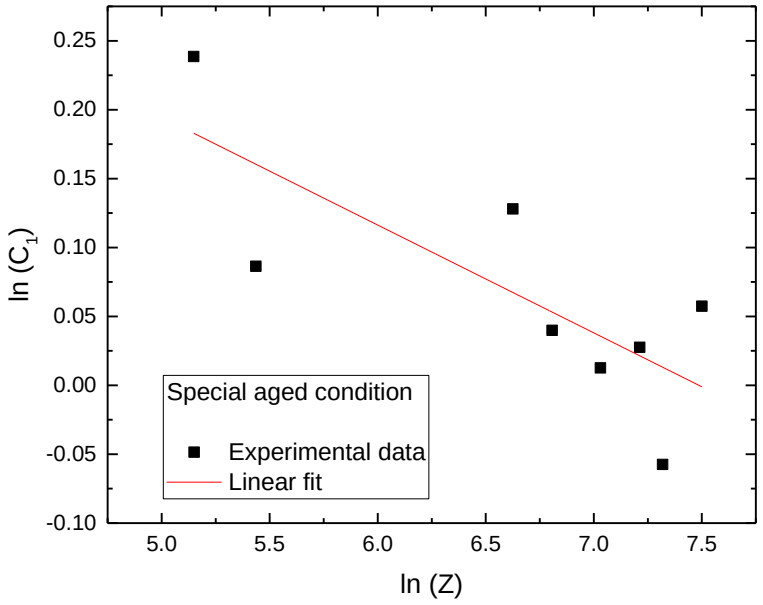

Figure 4.35: ln (C_1) plotted against ln (Z) for special aged heat treatment

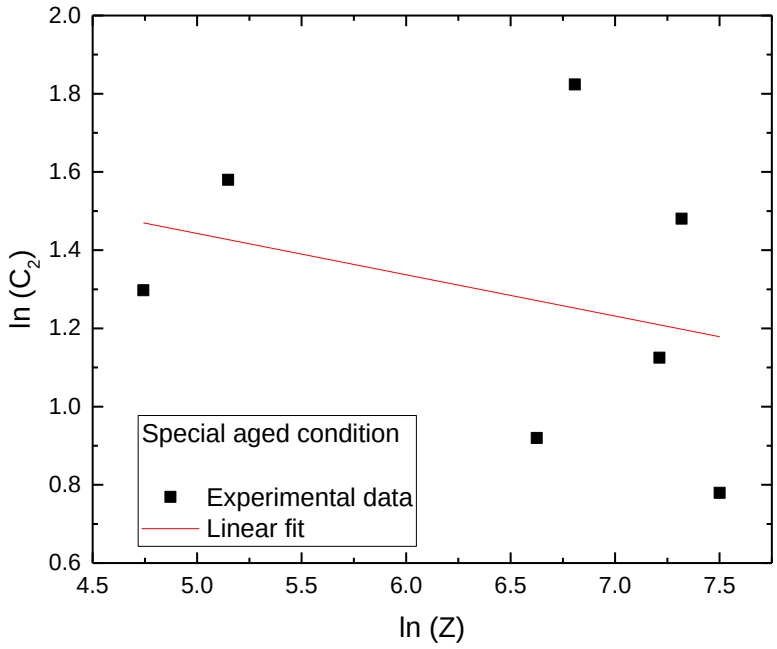

Figure 4.36: ln (C_2) plotted ln (Z) for special aged heat treatment

4.5.3 Modeling Dynamic Impact Behaviour of Haynes 282 – Standard Heat Treatment Condition

The constitutive model used to describe the dynamic impact behaviour of Haynes 282 in the standard heat treatment condition was derived by following a similar procedure outlined for the special aged heat treatment condition. Based on the analysis, the following Arrhenius-type constitutive model is developed for predicting the dynamic impact behaviour of Haynes 282 in the standard heat treatment condition.

$$\begin{gathered}\frac{\sigma}{\sigma_{\mathrm{p}}}=\left[\frac{\varepsilon}{\varepsilon_{\mathrm{p}}} exp\left(1-\frac{\varepsilon}{\varepsilon_{\mathrm{p}}}\right)\right]^{C} \\ \sigma_{\mathrm{p}}=\frac{1}{0.00079381} ln\left\{\left(\frac{Z}{A}\right)^{1/(-3.74)}+\left[\left(\frac{Z}{A}\right)^{2/(-3.74)}+1\right]^{1/2}\right\} \\ \varepsilon_{\mathrm{p}}=0.2455634 * Z^{0.0787} \\ Z=\dot{\varepsilon}\, exp\left(\frac{-4569}{\mathrm{R}T}\right) \\ C\ =\ 0.059 Z^{(-0.0314)} \\ A=\begin{cases}1684 & (\leq 2000/\mathrm{s\ strain\ rate}) \\ 2585 & (>2000/\mathrm{s\ strain\ rate})\end{cases}\end{gathered} \tag{4.22}$$

4.5.4 Modeling Dynamic Impact Behaviour of Haynes 282 – Solutionized Heat Treatment Condition

The constitutive model used to describe the dynamic impact behaviour of Haynes 282 in the solutionized condition was again derived by following a similar procedure for the special aged heat treatment. Based on the analysis, the following Arrhenius-type constitutive model is developed for predicting the dynamic impact behaviour of Haynes 282 superalloy in the solutionized condition:

$$\frac{\sigma}{\sigma_p} = \left[\frac{\varepsilon}{\varepsilon_p} exp\left(1 - \frac{\varepsilon}{\varepsilon_p}\right)\right]^c$$

$$\sigma_p = \frac{1}{0.00077058} ln\left\{\left(\frac{Z}{1919.88}\right)^{1/(-2.9855)} + \left[\left(\frac{Z}{1919.88}\right)^{2/(-2.9855)} + 1\right]^{1/2}\right\}$$

$$\varepsilon_p = 0.00198427831 * Z^{0.633} \quad (4.23)$$

$$Z = \dot{\varepsilon}\, exp\left(\frac{-2789.85}{RT}\right)$$

$$c = \begin{cases} 0.65 & \text{(for work hardening – dynamic recovery stage)} \\ 0.95 & \text{(for dynamic flow softening stage)} \end{cases}$$

4.6 Validation of the Proposed Constitutive Model

A comparison between the experimentally measured flow stress and those predicted by the Arrhenius-type model at various strain rates and temperatures are shown in Figure 4.37 to Figure 4.41. The predictability of the model under high strain rate condition is quantified by using statistical parameters, such as the average absolute relative error (AARE) and correlation coefficient (R) [213]–[215].

The AARE is calculated by using a term-by-term comparison of the relative error. It is an unbiased method for verifying the predictability of a model. R describes the linear relationship between the predicted and measured flow stresses [216]. These parameters can be expressed as [217]:

$$AARE = \frac{1}{N}\sum_{i=1}^{N} \left|\frac{E_i - P_i}{E_i}\right| \times 100\% \quad (4.24)$$

$$R = \frac{\sum_{i=1}^{N}(E_i - \bar{E})(P_i - \bar{P})}{\sqrt{\sum_{i=1}^{N}(E_i - \bar{E})^2 \sum_{i=1}^{N}(P_i - \bar{P})^2}} \quad (4.25)$$

where E_i and P_i are the experimental and model-predicted flow stresses, respectively. $\overline{E}$ and $\overline{P}$ are the mean values of the experimental and model-predicted flow stresses, respectively. N is the number of data points used in this study. Table 4.3 lists the values of the AARE and R that are calculated for the various strain rates and temperatures. For most impact conditions, there is a good agreement between the predicted and measured flow curves, particularly for deformations at room temperature.

A promising application of the proposed model is in finite element modelling to predict the stresses and strains that are found during high strain rate loading conditions, such as machining, ballistic impact, and blade containment system in aero engines. The model could be utilized in computer codes for simulation by directly inserting the model material constants into the software material database, or by incorporating a code into commercial software such as ABAQUS, LS-DYNA, and Marc [218]. By varying the model input parameters, such as the deformation strain rate and temperature, the model provides a tool for the machinist to optimize the cutting and feed forces, cutting power, maximum deformation temperature, etc. to improve the quality of the machined part.

Table 4.4: Predictability of proposed Arrhenius-type constitutive model

Type of heat treatment	**Impact momentum ($Kg.ms^{-1}$)**	**Temperature (^oC)**	**AARE (%)**	**R**
Standard heat treatment	35	25	1	0.98
	35	400*	10	0.87
	35	600	1	0.97
	35	800	12	0.93
Special aged	35	25	4	0.97
	35	400*	3	0.96
	35	600	14	0.96
	35	800	12	0.96
Solutionized	27	25	1.5	0.99
	35	25	2.7	0.94
	35	400	7.5	0.94
	35	800	16	0.92

*Experiment not used to calibrate the model

(a)

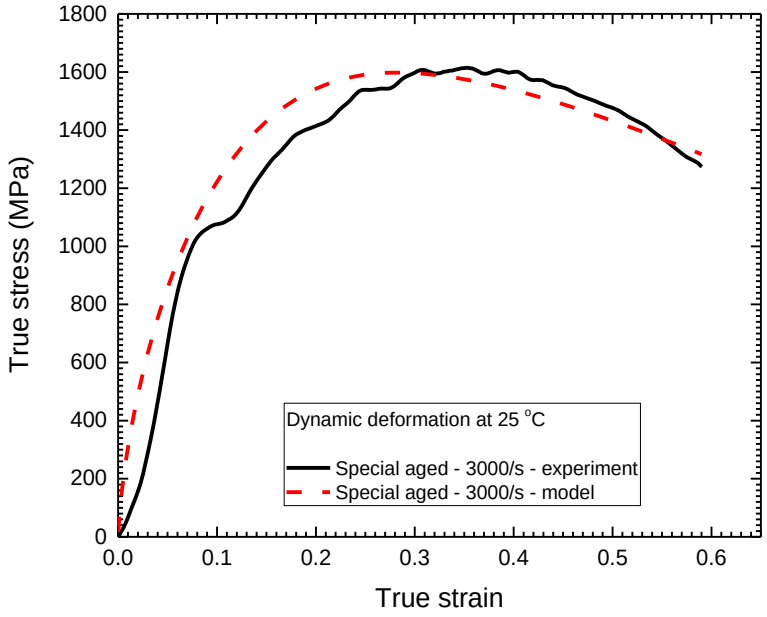

(b)

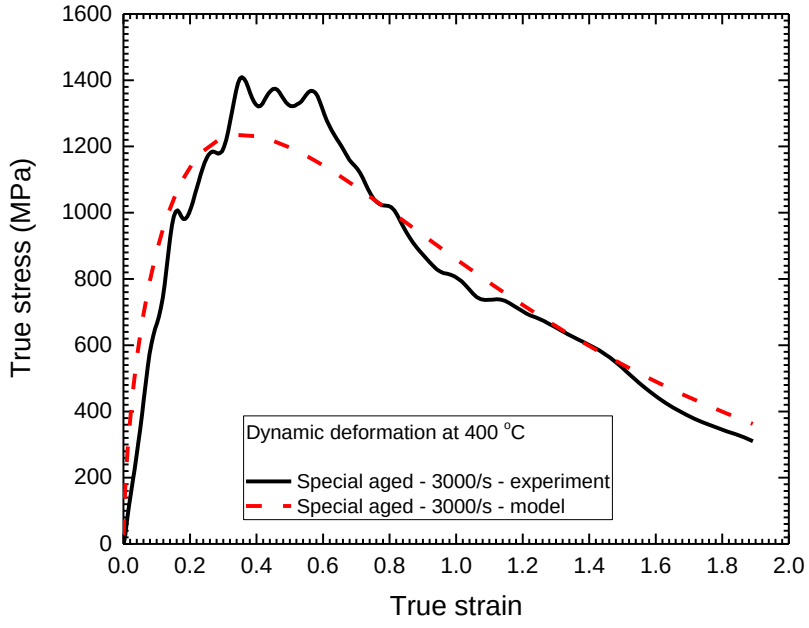

Figure 4.37: Comparison between experimental and predicted flow curves with the developed Arrhenius-type model for Haynes 282 in the special aged heat treatment at strain rate of 3000/s: (a) 25°C and (b) 400°C

(a)

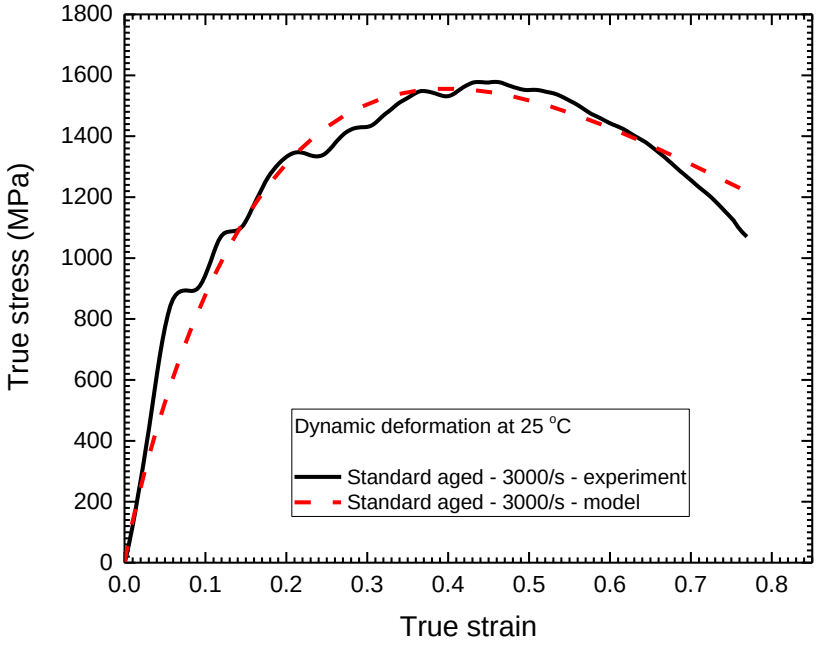

(b)

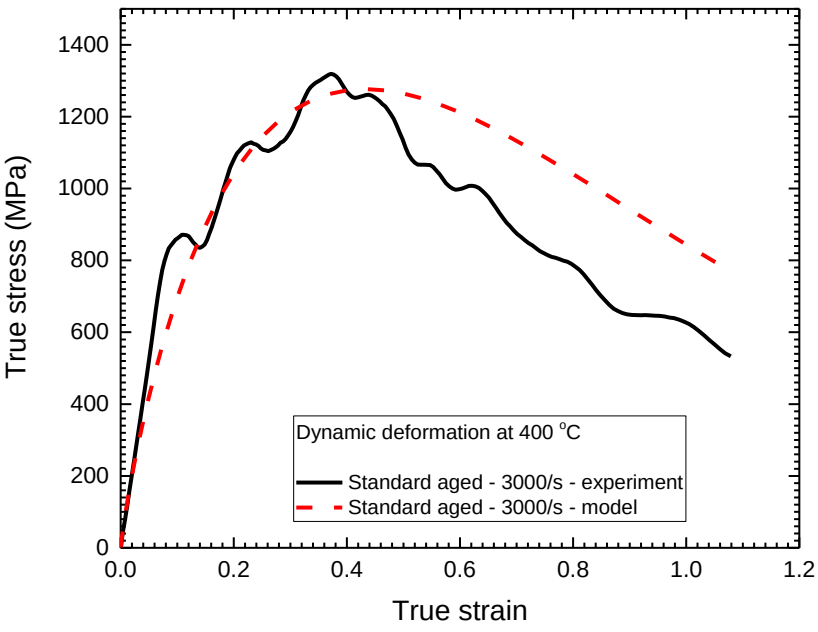

Figure 4.38: Comparison between experimental and predicted flow curves with the developed Arrhenius-type model for Haynes 282 in the standard heat treatment condition at strain rate of 3000/s: (a) 25°C and (b) 400°C

(a)

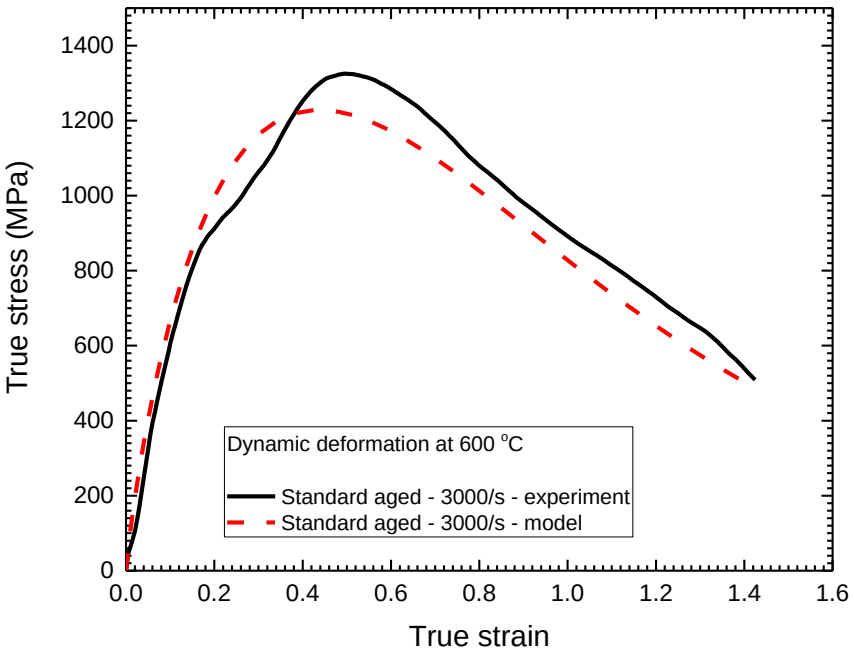

(b)

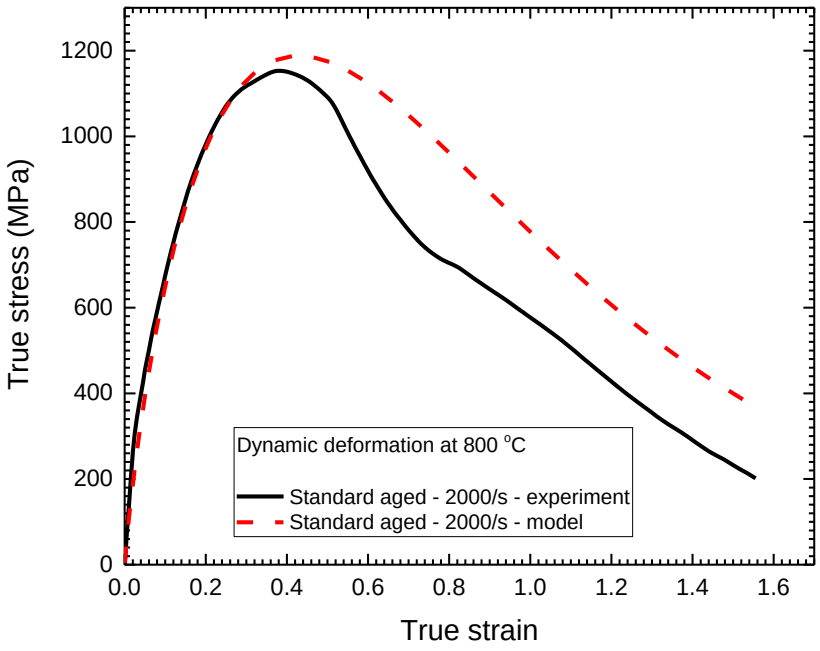

Figure 4.39: Comparison between experimental and predicted flow curves with the developed Arrhenius-type model for Haynes 282 in the standard heat treatment condition at (a) temperature of 600ºC and strain rate of 3000/s, (b) temperature of 800ºC and strain rate of 2000/s

(a)

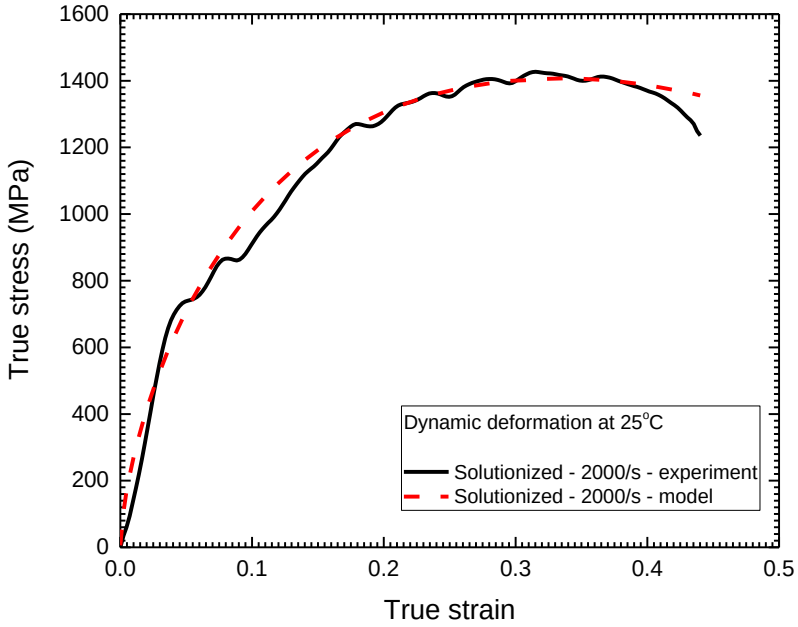

(b)

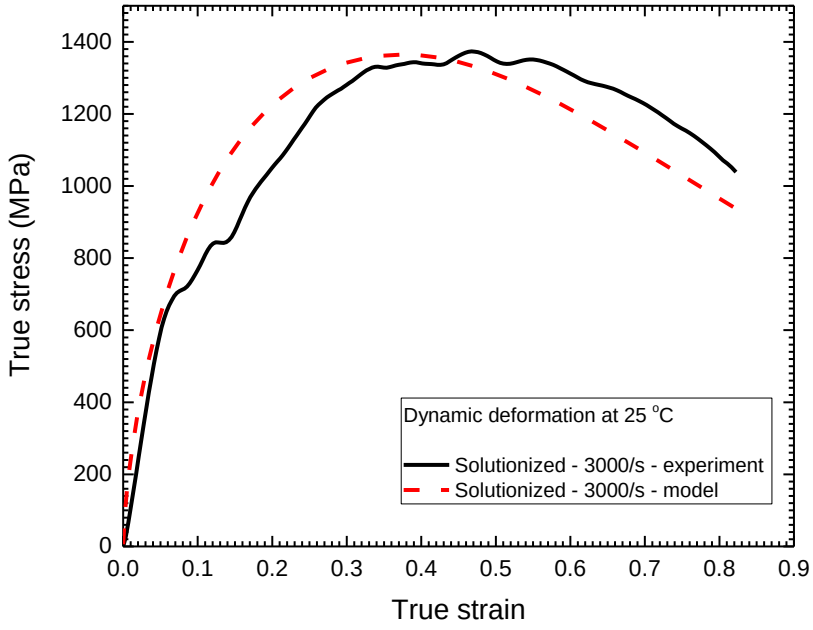

Figure 4.40: Comparison between experimental and predicted flow curves with the developed Arrhenius-type model for Haynes 282 in the solutionized heat treatment condition at room temperature and strain rate of (a) 2000/s and (b) 3000/s

(a)

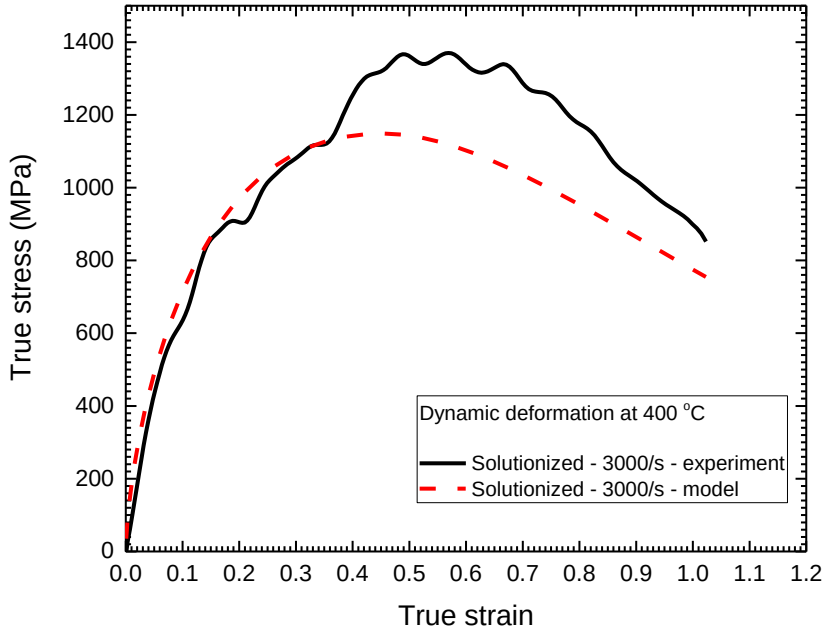

(b)

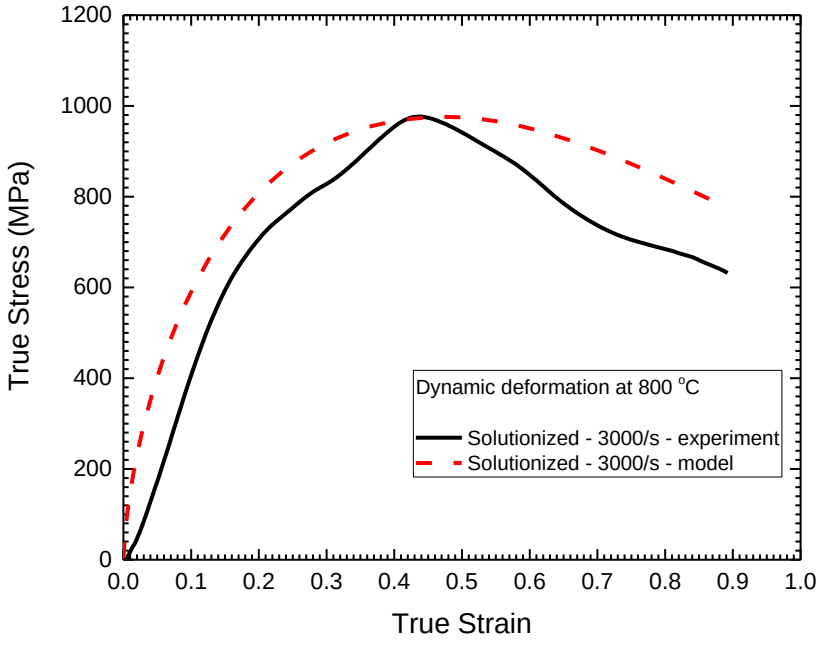

Figure 4.41: Comparison between experimental and predicted flow curves with the developed Arrhenius-type model for Haynes 282 in the solutionized heat treatment condition at strain rate of 3000/s and temperature of (a) 400°C and (b) 800°C

CHAPTER 5

CONCLUSIONS AND RECOMMENDATIONS FOR FUTURE WORK

5.1 Summary and Conclusions

A study on the quasi-static compressive and tensile properties and the dynamic impact behaviour of Haynes 282 superalloy has been carried out under three types of heat treatment conditions - solutionized, standard heat treatment, and special aged. A summary of the findings and conclusions from this research work is presented as follows:

1. Under quasi-static compressive loading, Haynes 282 has the highest strength after undergoing special aged heat treatment, followed by standard heat treatment, whilst the lowest strength is observed after solutionized heat treatment.
2. Under quasi-static compressive loading, no stress saturation or thermal softening effect is observed within the range of the strain rates examined (0.006/s and 0.035/s) after the three types of heat treatments are carried out. The deformation mechanism is therefore dominated by strain hardening.
3. Under quasi-static tensile loading, Haynes 282 has the highest yield and tensile strength after the special aged heat treatment, followed by standard heat treatment, whilst the lowest strength is observed after solutionized heat treatment.
4. The ductility of Haynes 282 is highest after solutionizing, followed by special aged heat treatment, but the least extent of elongation is observed after standard heat treatment.
5. Interestingly, in the aged condition, notwithstanding the higher yield and tensile strengths obtained after special aged heat treatment developed at the University of Manitoba, as

compared to the manufacturer's recommended standard heat treatment, the former produces a larger ductility (40%) compared to the latter, which exhibits a ductility of 27%.

6. Under dynamic impact deformation, the strength of Haynes 282 is observed to decrease with increased deformation temperature. The corresponding decrease in strength is greater at a temperature range of 25^{o}C to 400^{o}C and remains nearly constant when deformed at temperatures from 400^{o}C to 800^{o}C.
7. Haynes 282 has a near constant to negative strain rate sensitivity of the flow stress during impact loading in all the three heat treatment conditions. Its negative strain rate sensitivity could reduce the energy required for its deformation during machining.
8. The strength of Haynes 282 under impact loading is consistent with the trend observed during quasi-static loading. Special aged exhibits the highest strength followed by standard heat treatment, whilst the lowest strength is observed in the solutionized condition.
9. Under ballistic loading, Haynes 282 is most susceptible to failure after special aged heat treatment, followed by standard heat treatment, whilst solutionizing the alloy results in the least likelihood of failure due to its high strain hardening capability that suppresses the formation of ASBs.
10. Although special aged heat treatment provides better mechanical properties than standard heat treatment under quasi-static conditions, the higher strength and lower strain hardening capability of Haynes 282 under special aged makes it more susceptible to forming ASBs under impact loading.
11. It is observed that the main strengthening phase of the alloy in the aging heat treatments, the γ' precipitate phase, is dissolved into the ASBs during impact deformation. This could

be attributed to the synergistic effect from adiabatic heating, shearing of the precipitates, and strain-enhanced diffusion during deformation.

12. The coupled effects of strain rate, temperature, and strain rate softening under dynamic impact deformation is reasonably captured and predicted by an Arrhenius-type model. The model can be used for the numerical simulation of high strain rate applications, such as machining, ballistic impact, and blade containment system in aero engines.

5.2 Suggestions for Future Work

In this study, a phenomenological-based constitutive model has been developed to predict the high strain rate behaviour of Haynes 282. Future studies can implement the model in a finite element code to simulate and optimize design parameters in ballistic loading events. In addition, since considerable efforts are ongoing to develop a one-step aging heat treatment for Haynes 282 for A-USC steam boiler applications, it is recommended that the one-step aging heat treatment (900^{o}C/1 hour/FC) developed in this institution be evaluated for A-USC applications.

REFERENCES

[1] S. Haas, J. Andersson, M. Fisk, J.-S. Park, and U. Lienert, "Correlation of precipitate evolution with Vickers hardness in Haynes® 282® superalloy: In-situ high-energy SAXS/WAXS investigation," *Mater. Sci. Eng. A*, vol. 711, pp. 250–258, 2018.

[2] K. Nicol, "Status of advanced ultra-supercritical pulverised coal technology," *CCC/229, ISBN*, pp. 978–992, 2013.

[3] R. Viswanathan *et al.*, "US program on materials technology for ultra-supercritical coal power plants," *J. Mater. Eng. Perform.*, vol. 14, no. 3, pp. 281–292, 2005.

[4] M. Hörnqvist, C. Joseph, C. Persson, J. Weidow, and H. Lai, "Dynamic strain aging in Haynes 282 superalloy," *MATEC Web Conf.*, vol. 14, p. 16002, Aug. 2014.

[5] L. M. Pike, "Development of a fabricable gamma-prime (γ') strengthened superalloy," *Superalloys 2008*, pp. 191–200, 2008.

[6] D. L. Klarstrom, L. M. Pike, and V. R. Ishwar, "Nickel-base alloy solutions for ultrasupercritical steam power plants," *Procedia Eng.*, vol. 55, pp. 221–225, 2013.

[7] L. M. Pike, "Long Term Thermal Exposure of Haynes 282 Alloy," *Superalloy 718 Deriv.*, pp. 644–660, 2012.

[8] J. A. Hawk, T. Le Cheng, J. S. Sears, P. D. Jablonski, and Y. H. Wen, "Gamma Prime Stability in Haynes 282: Theoretical and Experimental Considerations," *J. Mater. Eng. Perform.*, vol. 24, no. 11, pp. 4171–4181, 2015.

[9] S. K. Srivastava, J. L. Caron, and L. M. Pike, “Recent Developments in the Characterisatics of Haynes 282 Alloy for Use in A-USC Applications,” pp. 120–130, 2014.

[10] C. Joseph, C. Persson, and M. Hornqvist Colliander, “Influence of heat treatment on the microstructure and tensile properties of Ni-base superalloy Haynes 282,” *Mater. Sci. Eng. A*, vol. 679, no. June 2016, pp. 520–530, 2017.

[11] J. Saarimäki, J. J. Moverare, and M. H. Colliander, “Time- and cycle-dependent crack propagation in Haynes 282,” *Mater. Sci. Eng. A*, vol. 658, pp. 463–471, 2016.

[12] K. A. Rozman, J. J. Kruzic, and J. A. Hawk, “Fatigue Crack Growth Behavior of Nickel-base Superalloy Haynes 282 at 550-750 °C,” *J. Mater. Eng. Perform.*, vol. 24, no. 8, pp. 2841–2846, 2015.

[13] R. A. Buckson and O. A. Ojo, “Cyclic deformation characteristics and fatigue crack growth behaviour of a newly developed aerospace superalloy Haynes 282,” *Mater. Sci. Eng. A*, vol. 555, pp. 63–70, 2012.

[14] M. Rodríguez-Millán, J. Díaz-Álvarez, R. Bernier, J. Cantero, A. Rusinek, and M. Miguelez, “Thermo-Viscoplastic Behavior of Ni-Based Superalloy Haynes 282 and Its Application to Machining Simulation,” *Metals (Basel).*, vol. 7, no. 12, p. 561, Dec. 2017.

[15] J. J. DeMange, V. Prakash, and J. M. Pereira, “Effects of material microstructure on blunt projectile penetration of a nickel-based super alloy,” *Int. J. Impact Eng.*, vol. 36, no. 8, pp. 1027–1043, Aug. 2009.

[16] A. L. Noradila, Z. Sajuri, J. Syarif, Y. Miyashita, and Y. Mutoh, “Effect of strain rates on

tensile and work hardening properties for Al-Zn magnesium alloys," in *IOP Conference Series: Materials Science and Engineering*, 2013, vol. 46, no. 1, p. 12031.

[17] A. G. Odeshi, S. Al-Ameeri, and M. N. Bassim, "Effect of high strain rate on plastic deformation of a low alloy steel subjected to ballistic impact," *J. Mater. Process. Technol.*, vol. 162–163, no. SPEC. ISS., pp. 385–391, 2005.

[18] J. M. Pereira and B. A. Lerch, "Effects of heat treatment on the ballistic impact properties of Inconel 718 for jet engine fan containment applications," *Int. J. Impact Eng.*, vol. 25, no. 8, pp. 715–733, Sep. 2001.

[19] C. Zener and J. H. Hollomon, "Effect of strain rate upon plastic flow of steel," *J. Appl. Phys.*, vol. 15, no. 1, pp. 22–32, 1944.

[20] B. Dodd and Y. Bai, *Adiabatic shear localization: frontiers and advances*. Elsevier, 2012.

[21] R. Culver, "Thermal instability strain in dynamic plastic deformation," in *Metallurgical effects at high strain rates*, Springer, 1973, pp. 519–530.

[22] H. C. Rogers, "Adiabatic shearing-general nature and material aspects," in *Material Behavior Under High Stress and Ultrahigh Loading Rates*, Springer, 1983, pp. 101–118.

[23] R. Dormeval, "Adiabatic shear phenomena," *DGM Informationsgesellschaft mbH, Impact Load. Dyn. Behav. Mater.*, vol. 1, pp. 43–56, 1988.

[24] Y. L. Bai, "A criterion for thermo-plastic shear instability," in *Shock waves and high-strain-rate phenomena in metals*, Springer, 1981, pp. 277–284.

[25] M. R. Staker, "The relation between adiabatic shear instability strain and material

properties," *Acta Metall.*, vol. 29, no. 4, pp. 683–689, 1981.

[26] A. G. Odeshi, M. N. Bassim, and S. Al-Ameeri, "Effect of heat treatment on adiabatic shear bands in a high-strength low alloy steel," *Mater. Sci. Eng. A*, vol. 419, no. 1–2, pp. 69–75, 2006.

[27] M. P. Jackson and R. C. Reed, "Heat treatment of UDIMET 720Li: the effect of microstructure on properties," *Mater. Sci. Eng. A*, vol. 259, no. 1, pp. 85–97, 1999.

[28] H. Qi, M. Azer, and A. Ritter, "Studies of standard heat treatment effects on microstructure and mechanical properties of laser net shape manufactured Inconel 718," *Metall. Mater. Trans. A*, vol. 40, no. 10, pp. 2410–2422, 2009.

[29] C. T. Sims, N. S. Stoloff, and W. C. Hagel, *superalloys II*. Wiley New York, 1987.

[30] C. D. Desforges, "Metals and alloys for high temperature applications. Current status and future prospects," in *1. Petten colloquium on advanced high temperature materials: technological and industrial aspects. Petten, Netherlands, 29-30 January 1976*, 1977.

[31] E. F. Bradley, "Source book on materials for elevated-temperature applications: a comprehensive collection of outstanding articles from the periodical and reference literature," 1979.

[32] J. K. Tien and T. Caulfield, *Superalloys, supercomposites, and superceramics*. Academic Press, 1989.

[33] A. P. Mouritz, *Introduction to aerospace materials*. Elsevier, 2012.

[34] M. J. Donachie and S. J. Donachie, "Superalloys: A Technical Guide, Second Edition,"

2001.

[35] F. C. Campbell, “Superalloys [J],” *Manuf. Technol. Aerosp. Struct. Mater.*, pp. 211–272, 2006.

[36] Wikimedia Commons contributors, “File:Jet engine Processing.png,” *Wikimedia Commons, the free media repository.*, 2016. .

[37] J. Silk, “ATI Jet Engine Materials,” 2018. [Online]. Available: https://www.slideshare.net/johnpsilk/ati-jet-engine. [Accessed: 05-Apr-2018].

[38] E. Akca and A. Gürsel, “A review on superalloys and IN718 Nickel-based INCONEL superalloy,” *Period. Eng. Nat. Sci.*, vol. 3, no. 1, 2015.

[39] C. P. Sullivan and M. J. Donachie Jr, “Iron-Base and Iron-Containing Superalloys,” *Source B. Mater. Elev. Appl. a Compr. Collect. Outst. Artic. from Period. Ref. Lit.*, p. 239, 1979.

[40] S. H. M. Anijdan and A. Bahrami, “A new method in prediction of TCP phases formation in superalloys,” *Mater. Sci. Eng. A*, vol. 396, no. 1–2, pp. 138–142, 2005.

[41] W. F. Simmons and H. J. Wagner, “Where you can use todays superalloys,” *MET PROG*, vol. 71, no. 6, pp. 87–92, 1967.

[42] M. J. Donachie Jr, “Relationship of Properties to Microstructure in Superalloys,” *Am. Soc. Met. Superalloys--Source Book*, pp. 102–111, 1984.

[43] A. Luna Ramírez, J. Porcayo-Calderon, Z. Mazur, V. M. Salinas-Bravo, and L. Martinez-Gomez, “Microstructural Changes during High Temperature Service of a Cobalt-Based Superalloy First Stage Nozzle,” *Adv. Mater. Sci. Eng.*, vol. 2016, pp. 1–7, May 2016.

[44] T. Henhoeffer, X. Huang, S. Yand, P. Au, and D. Nagy, “Microstructure and high temperature tensile properties of wide gap brazed cobalt based superalloy X-40,” 2013.

[45] B. Geddes, H. Leon, and X. Huang, *Superalloys: alloying and performance*. ASM International, 2010.

[46] C. T. Sims, “A contemporary view of cobalt-base alloys,” *JOM*, vol. 21, no. 12, pp. 27–42, 1969.

[47] S. K. Makineni, B. Nithin, and K. Chattopadhyay, “Synthesis of a new tungsten-free γ–γ′ cobalt-based superalloy by tuning alloying additions,” *Acta Mater.*, vol. 85, pp. 85–94, 2015.

[48] J. R. Davis, *Nickel, cobalt, and their alloys*. ASM International, 2000.

[49] C. P. Sullivan, J. D. Varin, and M. Donachie, “Relationship of properties to microstructure in cobalt-base superalloys,” 1968.

[50] T. Nishizawa and K. Ishida, “The Co (cobalt) system,” *Bull. Alloy phase diagrams*, vol. 4, no. 4, pp. 387–390, 1983.

[51] R. Lizárraga, F. Pan, L. Bergqvist, E. Holmström, Z. Gercsi, and L. Vitos, “First principles theory of the hcp-fcc phase transition in cobalt,” *Sci. Rep.*, vol. 7, no. 1, p. 3778, 2017.

[52] E. Vacchieri, A. Costa, G. Roncallo, and G. Cacciamani, “Service induced fcc→hcp martensitic transformation in a Co-based superalloy,” *Mater. Sci. Technol.*, vol. 33, no. 9, pp. 1100–1107, 2017.

[53] Birmingham Metallurgical Society and W. O. Alexander, *Metallurgical achievements :*

selection of papers presented at the Birmingham Metallurgical Society's diamond jubilee session, 1963-1964. .

[54] H. J. Wagner and H. C. Cross, "Materials for Gas Turbines," *Gas Turbine Eng. Handb.*, pp. 227–238, 1966.

[55] G. P. Sabol and R. Stickler, "Microstructure of Nickel-Based Superalloys," *Phys. status solidi*, vol. 35, no. 1, pp. 11–52, 1969.

[56] E. W. Ross and C. T. Sims, "Nickel-base alloys," *Wiley-Interscience, John Wiley Sons, Superalloys II--High Temp. Mater. Aerosp. Ind. Power*, pp. 97–133, 1987.

[57] W. S. Lee, C. Y. Liu, and T. N. Sun, "Dynamic impact response and microstructural evolution of inconel 690 superalloy at elevated temperatures," *Int. J. Impact Eng.*, vol. 32, no. 1–4, pp. 210–223, 2006.

[58] F. R. Morral, "Wrought superalloys," *Met. Handbook*, vol. 3, p. 219, 1980.

[59] C. Joseph, M. Hornqvist, and C. Persson, "Anisotropy of Room Temperature Ductility in Haynes 282 Forgings," pp. 601–609, 2014.

[60] L. O. Osoba, A. K. Khan, and O. A. Ojo, "Identification of Mo-based Precipitates in Haynes 282 Superalloy," *Metall. Mater. Trans. A Phys. Metall. Mater. Sci.*, vol. 48, no. 4, pp. 1540–1543, 2017.

[61] Y. Yang, R. C. Thomson, R. M. Leese, and S. Roberts, "Microstructural evolution in cast Haynes 282 for applications in advanced power plants," in *Advances in Materials Technology for Fossil Power Plants: Proceedings from the Seventh International*

Conference (EPRI 2013), 2014, pp. 143–154.

[62] "Haynes 282 Brochure," 2018. [Online]. Available: http://haynesintl.com/docs/default-source/pdfs/new-alloy-brochures/high-temperature-alloys/brochures/282-brochure.pdf?sfvrsn=20. [Accessed: 05-Apr-2018].

[63] S. J. Rosenberg, "Nickel and its alloys," National Bureau of Standards Gaithersburg MD, 1968.

[64] J. Everhart, *Engineering properties of nickel and nickel alloys*. Springer Science & Business Media, 2012.

[65] R. C. Reed, *The superalloys: fundamentals and applications*. Cambridge university press, 2008.

[66] J. C. Freche, R. L. Ashbrook, and S. J. Klima, "A New Series of Cobalt-Refractory-Metal Alloys for Advanced Space Power Systems." Cobalt, 1963.

[67] W. F. Smith, *Structure and properties of engineering alloys*. McGraw-Hill, 1993.

[68] S. D. Antolovich and J. E. Campbell, "Fracture properties of superalloys," *Appl. Fract. Mech. Sel. Met. Struct. Mater. 83-25317 10-26) Met. Park. OH, Am. Soc. Met. 1982*, pp. 253–310, 1982.

[69] D. R. Muzyka, "Physical metallurgy and effects of process variables on the microstructure of wrought superalloys," in *MiCon 78: Optimization of Processing, Properties, and Service Performance Through Microstructural Control*, ASTM International, 1979.

[70] H. K. D. H. Bhadeshia, "Nickel based superalloy: dislocation structure," 2018. [Online].

Available: http://www.phase-trans.msm.cam.ac.uk/2002/Zhang.html. [Accessed: 09-Apr-2018].

[71] H. T. Kim, S. S. Chun, X. X. Yao, Y. Fang, and J. Choi, "Gamma prime (γ′) precipitating and ageing behaviours in two newly developed nickel-base superalloys," *J. Mater. Sci.*, vol. 32, no. 18, pp. 4917–4923, 1997.

[72] F. C. Campbell, *Phase diagrams: understanding the basics*. ASM International, 2012.

[73] H. Monajati, M. Jahazi, R. Bahrami, and S. Yue, "The influence of heat treatment conditions on γ′ characteristics in Udimet® 720," *Mater. Sci. Eng. A*, vol. 373, no. 1–2, pp. 286–293, 2004.

[74] L. M. Pike, "HAYNES® 282™ Alloy: A New Wrought Superalloy Designed for Improved Creep Strength and Fabricability," in *ASME Turbo Expo 2006: Power for Land, Sea, and Air*, 2006, pp. 1031–1039.

[75] J. Andersson, G. Sjöberg, and M. Chaturvedi, "Hot Ductility Study of HAYNES® 282® Superalloy," in *Proceedings of the 7th International Symposium on Superalloy 718 and Derivatives*, 2012, pp. 539–554.

[76] S. Tin, T. M. Pollock, and W. T. King, "Carbon additions and grain defect formation in high refractory nickel-base single crystal superalloys," *Ann Arbor*, vol. 1001, p. 48109, 2000.

[77] C. T. Sims, N. S. Stoloff, W. C. Hagel, and S. II, "High temperature materials for aerospace and industrial power," *A Wiley-lnterscience Publ. John Wiley Sons, New York*, 1987.

[78] R. F. Decker, "The metallurgy of nickel-base alloys," *Superalloys*, vol. 33, 1972.

[79] L. O. Osoba, R. G. Ding, and O. A. Ojo, “Improved resistance to laser weld heat-affected zone microfissuring in a newly developed superalloy HAYNES 282,” *Metall. Mater. Trans. A*, vol. 43, no. 11, pp. 4281–4295, 2012.

[80] A. Ghoneim and O. A. Ojo, “Microstructure and mechanical response of transient liquid phase joint in Haynes 282 superalloy,” *Mater. Charact.*, vol. 62, no. 1, pp. 1–7, 2011.

[81] H. Matysiak *et al.*, “Microstructure of Haynes® 282® superalloy after vacuum induction melting and investment casting of thin-walled components,” *Materials (Basel).*, vol. 6, no. 11, pp. 5016–5037, 2013.

[82] M. G. Fahrmann and L. M. Pike, “Experimental TTT Diagram of HAYNES 282 Alloy,” in *Proceedings of the 9th International Symposium on Superalloy 718 & Derivatives: Energy, Aerospace, and Industrial Applications*, 2018, pp. 565–578.

[83] R. F. Decker, “Strengthening mechanisms in nickel-base superalloys,” in *Steel Strengthening Mechanisms Symposium, Zurich, Switzerland, May 5 and 6, 1969*, 1969, pp. 1–23.

[84] R. Nordheim and N. J. Grant, “Resistivity anomalies in the nickel chromium system as evidence of ordering reactions,” *J. Inst. Met.*, vol. 82, no. 9, pp. 440–444, 1954.

[85] G. M. Janowski, “The effect of tantalum on the structure/properties of two polycrystalline nickel-base superalloys: B-1900+ Hf MAR-M247. MS Thesis, Final Report,” 1985.

[86] M. Durand-Charre, “The microstructure of superalloys. 1997,” *Gordon Breach Sci. Publ.*

[87] M. C. Kushan, S. C. Uzgur, Y. Uzunonat, and F. Diltemiz, “ALLVAC 718 Plus™

superalloy for aircraft engine applications," in *Recent Advances in Aircraft Technology*, InTech, 2012.

[88] J. C. Lippold, S. D. Kiser, and J. N. DuPont, *Welding metallurgy and weldability of nickel-base alloys*. John Wiley & Sons, 2011.

[89] H. Gleiter and E. Hornbogen, "Precipitation hardening by coherent particles," *Mater. Sci. Eng.*, vol. 2, no. 6, pp. 285–302, 1968.

[90] S. M. Copley and B. H. Kear, "A dynamic theory of coherent precipitation hardening with application to nickel-base superalloys," *Trans. Met. Soc. AIME*, vol. 239, pp. 984–992, 1967.

[91] R. F. Decker and J. R. Mihalisin, "Coherency strains in gamma prime hardened nickel alloys," *ASM TRANS QUART*, vol. 62, no. 2, pp. 481–489, 1969.

[92] M. Segersäll, "Nickel-Based Single-Crystal Superalloys: the crystal orientation influence on high temperature properties." Linköping University Electronic Press, 2013.

[93] F. Bianchini, "Mechanical Properties of Nickel-based Superalloys A Multiscale Atomistic Investigation," 2018.

[94] T. Gladman, "Precipitation hardening in metals," *Mater. Sci. Technol.*, vol. 15, no. 1, pp. 30–36, 1999.

[95] C. H. Lund, "Physical Metallurgy of Nickel-Base Superalloys," Battelle Memorial Inst. Columbus OH Defense Metals Information Center, 1961.

[96] G. E. Totten and D. S. MacKenzie, *Handbook of Aluminum: Vol. 1: Physical Metallurgy*

and Processes, vol. 1. CRC Press, 2003.

[97] J. A. Zukas, T. Nicholas, H. F. Swift, L. B. Greszczuk, D. R. Curran, and L. E. Malvern, "Impact dynamics," *J. Appl. Mech.*, vol. 50, p. 702, 1983.

[98] L. D. Oosterkamp, A. Ivankovic, and G. Venizelos, "High strain rate properties of selected aluminium alloys," *Mater. Sci. Eng. A*, vol. 278, no. 1–2, pp. 225–235, 2000.

[99] J. Harding, "The effect of high strain rate on material properties," in *Materials at high strain rates*, Elsevier Applied Science London, 1987, pp. 133–186.

[100] X. Wang, C. Huang, B. Zou, H. Liu, H. Zhu, and J. Wang, "Dynamic behavior and a modified Johnson-Cook constitutive model of Inconel 718 at high strain rate and elevated temperature," *Mater. Sci. Eng. A*, vol. 580, pp. 385–290, 2013.

[101] W.-S. Lee, C.-Y. Liu, and T.-N. Sun, "Deformation behavior of Inconel 690 super alloy evaluated by impact test," *J. Mater. Process. Technol.*, vol. 153, pp. 219–225, 2004.

[102] R. J. Wasley, *Stress wave propagation in solids: an introduction*, vol. 7. M. Dekker, 1973.

[103] J. Achenbach, *Wave propagation in elastic solids*, vol. 16. Elsevier, 2012.

[104] B. Hopkinson, "A method of measuring the pressure produced in the detonation of high explosives or by the impact of bullets," *Philos. Trans. R. Soc. London. Ser. A, Contain. Pap. a Math. or Phys. Character*, vol. 213, no. 497–508, pp. 437–456, 1914.

[105] H. Kolsky, "An investigation of the mechanical properties of materials at very high rates of loading," *Proc. Phys. Soc. Sect. B*, vol. 62, no. 11, p. 676, 1949.

[106] M. Demiral, T. Leemet, M. Hokka, V. T. Kuokkala, A. Roy, and V. V. Silberschmidt, "Finite-Element Simulations of Split Hopkinson Test of Ti-Based Alloy," *Adv. Mater. Res.*, vol. 223, pp. 296–303, 2011.

[107] W.-S. Lee, T.-H. Chen, C.-F. Lin, and W.-Z. Luo, "Dynamic Mechanical Response of Biomedical 316L Stainless Steel as Function of Strain Rate and Temperature.," *Bioinorg. Chem. Appl.*, no. December 2011, p. 173782, 2011.

[108] M. K. Asada, "An Analytical Evaluation of Spall Suppression of Impulsively Loaded Aluminum Panels Based on a One Dimensional Stress Wave Propagation Model," Naval Postgraduate School, Monterey, California, 1984.

[109] G. Gray, "Classic Split-Hopkinson Pressure Bar Testing.," *Mater. Park. OH ASM Int. 2000.*, vol. 8, pp. 462–476, 2000.

[110] G. R. Johnson and W. H. Cook, "A constitutive model and data for metals subjected to large strains, high strain rates and high temperatures," *7th International Symposium on Ballistics*. pp. 541–547, 1983.

[111] E. Voce, "The relationship between stress and strain for homogeneous deformation," *J. Inst. Met.*, vol. 74, pp. 537–562, 1948.

[112] A. S. Khan and S. Huang, "Experimental and theoretical study of mechanical behavior of 1100 aluminum in the strain rate range 10− 5− 104s− 1," *Int. J. Plast.*, vol. 8, no. 4, pp. 397–424, 1992.

[113] Y. C. Lin and G. Liu, "A new mathematical model for predicting flow stress of typical high-

strength alloy steel at elevated high temperature," *Comput. Mater. Sci.*, vol. 48, no. 1, pp. 54–58, 2010.

[114] D. Trimble, H. Shipley, L. Lea, A. Jardine, and G. E. O'Donnell, "Constitutive analysis of biomedical grade Co-27Cr-5Mo alloy at high strain rates," *Mater. Sci. Eng. A*, vol. 682, pp. 466–474, 2017.

[115] A. He, G. Xie, H. Zhang, and X. Wang, "A comparative study on Johnson-Cook, modified Johnson-Cook and Arrhenius-type constitutive models to predict the high temperature flow stress in 20CrMo alloy steel," *Mater. Des.*, vol. 52, pp. 677–685, 2013.

[116] Y. Zhao, J. Sun, J. Li, Y. Yan, and P. Wang, "A comparative study on Johnson-Cook and modified Johnson-Cook constitutive material model to predict the dynamic behavior laser additive manufacturing FeCr alloy," *J. Alloys Compd.*, 2017.

[117] M. Vural and J. Caro, "Experimental analysis and constitutive modeling for the newly developed 2139-T8 alloy," *Mater. Sci. Eng. A*, vol. 520, no. 1–2, pp. 56–65, 2009.

[118] H. Zhang, W. Wen, and H. Cui, "Behaviors of IC10 alloy over a wide range of strain rates and temperatures: Experiments and modeling," *Mater. Sci. Eng. A*, vol. 504, no. 1–2, pp. 99–103, 2009.

[119] Y. C. Lin, M.-S. Chen, and J. Zhong, "Constitutive modeling for elevated temperature flow behavior of 42CrMo steel," *Comput. Mater. Sci.*, vol. 42, no. 3, pp. 470–477, 2008.

[120] C. Gang *et al.*, "Strain-compensated Arrhenius-type constitutive model for flow behavior of Al-12Zn-2.4 Mg-1.2 Cu alloy," *Rare Met. Mater. Eng.*, vol. 44, no. 9, pp. 2120–2125,

2015.

[121] D. Samantaray, S. Mandal, and A. K. Bhaduri, “A comparative study on Johnson Cook, modified Zerilli–Armstrong and Arrhenius-type constitutive models to predict elevated temperature flow behaviour in modified 9Cr–1Mo steel,” *Comput. Mater. Sci.*, vol. 47, no. 2, pp. 568–576, 2009.

[122] S. R. Chen and G. T. Gray, “Constitutive behavior of tantalum and tantalum-tungsten alloys,” *Metall. Mater. Trans. A*, vol. 27, no. 10, pp. 2994–3006, 1996.

[123] F. J. Zerilli and R. W. Armstrong, “Dislocation-mechanics-based constitutive relations for material dynamics calculations,” *J. Appl. Phys.*, vol. 61, no. 5, pp. 1816–1825, 1987.

[124] Y. C. Lin, M.-S. Chen, and J. Zhong, “Prediction of 42CrMo steel flow stress at high temperature and strain rate,” *Mech. Res. Commun.*, vol. 35, no. 3, pp. 142–150, 2008.

[125] Sr. Bodner and Y. Partom, “Constitutive equations for elastic-viscoplastic strain-hardening materials,” *J. Appl. Mech.*, vol. 42, no. 2, pp. 385–389, 1975.

[126] M.-C. Cai, L.-S. Niu, X.-F. Ma, and H.-J. Shi, “A constitutive description of the strain rate and temperature effects on the mechanical behavior of materials,” *Mech. Mater.*, vol. 42, no. 8, pp. 774–781, 2010.

[127] H. Mecking and U. F. Kocks, “Kinetics of flow and strain-hardening,” *Acta Metall.*, vol. 29, no. 11, pp. 1865–1875, 1981.

[128] N. Tsuchida, Y. Tomota, H. Moriya, O. Umezawa, and K. Nagai, “Application of the Kocks–Mecking model to tensile deformation of an austenitic 25Cr–19Ni steel,” *Acta*

Mater., vol. 49, no. 15, pp. 3029–3038, 2001.

[129] S. Nemat-Nasser and Y. Li, "Flow stress of FCC polycrystals with application to OFHC Cu," *Acta Mater.*, vol. 46, no. 2, pp. 565–577, 1998.

[130] F. H. Abed and G. Z. Voyiadjis, "A consistent modified Zerilli-Armstrong flow stress model for BCC and FCC metals for elevated temperatures," *Acta Mech.*, vol. 175, no. 1–4, pp. 1–18, 2005.

[131] Y. C. Lin and X.-M. Chen, "A combined Johnson–Cook and Zerilli–Armstrong model for hot compressed typical high-strength alloy steel," *Comput. Mater. Sci.*, vol. 49, no. 3, pp. 628–633, 2010.

[132] Lius Fernando Moura Fernandes Braga, "Evaluation of Mechanical Properties of Aerospace Materials - Haynes 282," 2013.

[133] J. E. Pope, P. H. and Field, "Determination of strain in a dynamic compression test," *J. Phys. E.*, vol. 17, no. 9, pp. 817–820, 1984.

[134] R. Nakkalil, J. R. Hornaday Jr, and M. N. Bassim, "Characterization of the compression properties of rail steels at high temperatures and strain rates," *Mater. Sci. Eng. A*, vol. 141, no. 2, pp. 247–260, 1991.

[135] R. S. Hartley, T. J. Cloete, and G. N. Nurick, "An experimental assessment of friction effects in the split Hopkinson pressure bar using the ring compression test," *Int. J. Impact Eng.*, vol. 34, no. 10, pp. 1705–1728, 2007.

[136] K. T. Ramesh, "High rates and impact experiments," in *Springer handbook of experimental*

solid mechanics, Springer, 2008, pp. 929–960.

[137] G. Asala, J. Andersson, and O. A. Ojo, "Microstructure Dependence of Dynamic Impact Behaviour of ATI 718plus® Superalloy," in *Proceedings of the 9th International Symposium on Superalloy 718 & Derivatives: Energy, Aerospace, and Industrial Applications*, 2018, pp. 369–378.

[138] D. A. Gorham, P. H. Pope, and J. E. Field, "An improved method for compressive stress-strain measurements at very high strain rates," *Proc. R. Soc. Lond. A*, vol. 438, no. 1902, pp. 153–170, 1992.

[139] C. K. H. Dharan and F. E. Hauser, "Determination of stress-strain characteristics at very high strain rates," *Exp. Mech.*, vol. 10, no. September, pp. 370–376, 1970.

[140] R. Narayanasamy and K. S. Pandey, "Phenomenon of barrelling in aluminium solid cylinders during cold upset-forming," *J. Mater. Process. Technol.*, vol. 70, no. 1–3, pp. 17–21, 1997.

[141] ASTM-E8M-04, "Standard test methods for tension testing of metallic materials [Metric]." ASTM International West Conshohocken, PA, 2004.

[142] ASTM, "ASTM E112-13: Standard test methods for determining average grain size," *ASTM Int.*, pp. 1–28, 2013.

[143] C. T. Rueden *et al.*, "ImageJ2: ImageJ for the next generation of scientific image data," *BMC Bioinformatics*, vol. 18, no. 1, p. 529, 2017.

[144] ASTM, "E140-07 Standard hardness conversion tables for metals relationship among

brinell hardness, vickers hardness, rockwell hardness, superficial hardness, knoop hardness, and scleroscope hardness," *Astm*, pp. 1–21, 2007.

[145] D. L. Klarstrom and L. M. Pike, "Materials Solutions for Advanced Steam Power Plants," in *Advances in Materials Technology for Fossil Power Plants, Proc. Fifth Int. Conf*, 2007, pp. 107–118.

[146] L. O. Osoba, "A study on laser weldability improvement of newly developed Haynes 282 superalloy," 2012.

[147] J. Yan *et al.*, "Impact of Aging Temperature on the Performance of a Nickel-Iron-Based Superalloy," *Metall. Mater. Trans. A*, pp. 1–10, 2018.

[148] S. R. Reid and J. J. Harrigan, "Transient effects in the quasi-static and dynamic internal inversion and nosing of metal tubes," *Int. J. Mech. Sci.*, vol. 40, no. 2–3, pp. 263–280, 1998.

[149] M. Azarbarmas, M. Aghaie-Khafri, J. M. Cabrera, and J. Calvo, "Microstructural evolution and constitutive equations of Inconel 718 alloy under quasi-static and quasi-dynamic conditions," *Mater. Des.*, vol. 94, pp. 28–38, Mar. 2016.

[150] P. Zhang *et al.*, "Tensile Properties and Deformation Mechanisms of Haynes 282 at Various Temperatures," *Metall. Mater. Trans. A*, vol. 49, no. 5, pp. 1571–1578, 2018.

[151] S. Y. Zhong, V. Klosek, Y. De Carlan, and M. H. Mathon, "Modeling of structural hardening in oxide dispersion-strengthened (ODS) ferritic alloys," *J. Mater. Sci.*, vol. 51, no. 5, pp. 2540–2549, 2016.

[152] R. E. Stoltz and A. G. Pineau, "Dislocation-precipitate interaction and cyclic stress-strain

behavior of a γ′ strengthened superalloy," *Mater. Sci. Eng.*, vol. 34, no. 3, pp. 275–284, Aug. 1978.

[153] J. R. Davis, *Tensile testing*. ASM international, 2004.

[154] C. Joseph, M. Hörnqvist, and C. Persson, "Anisotropy of room temperature ductility in Haynes 282 forgings," in *Proceedings of the 8th International Symposium on Superalloy 718 and Derivatives*, 2014, pp. 601–609.

[155] J. H. Hollomon, "Tensile deformation," *Aime Trans*, vol. 12, no. 4, pp. 1–22, 1945.

[156] K. Gopinath, A. K. Gogia, S. V Kamat, R. Balamuralikrishnan, and U. Ramamurty, "Tensile properties of Ni-Based Superalloy 720Li: Temperature and strain rate effects," *Metall. Mater. Trans. A*, vol. 39, no. 10, pp. 2340–2350, 2008.

[157] M. Bauccio, *ASM metals reference book*. ASM international, 1993.

[158] G. R. Leverant and M. Gell, "The Elevated Temperature Fatigue of a Nickel-base Superalloy, MAR-M 200, in Conventionally-cast and Directionally Solidified forms," *TRANS MET SOC AIME*, vol. 245, no. 6, pp. 1167–1173, 1969.

[159] R. Hu, G. Bai, J. Li, J. Zhang, T. Zhang, and H. Fu, "Precipitation behavior of grain boundary M23C6 and its effect on tensile properties of Ni–Cr–W based superalloy," *Mater. Sci. Eng. A*, vol. 548, pp. 83–88, 2012.

[160] G. A. Rao, M. Kumar, M. Srinivas, and D. S. Sarma, "Effect of standard heat treatment on the microstructure and mechanical properties of hot isostatically pressed superalloy inconel 718," *Mater. Sci. Eng. A*, vol. 355, no. 1–2, pp. 114–125, 2003.

[161] T. P. Gabb, J. Telesman, P. T. Kantzos, and A. Garg, “Effects of temperature on failure modes for a nickel-base disk superalloy,” *J. Fail. Anal. Prev.*, vol. 7, no. 1, pp. 56–65, 2007.

[162] C. Wang, Y. Guo, J. Guo, and L. Zhou, “Investigation and improvement on structural stability and stress rupture properties of a Ni–Fe based alloy,” *Mater. Des.*, vol. 88, pp. 790–798, 2015.

[163] A. Sengupta *et al.*, “Tensile behavior of a new single-crystal nickel-based superalloy (CMSX-4) at room and elevated temperatures,” *J. Mater. Eng. Perform.*, vol. 3, no. 1, pp. 73–81, 1994.

[164] J. R. Groh and D. P. Mourer, “Alternate material for elevated temperature turbine cooling plate applications,” *Superalloys 2004*, pp. 101–108, 2004.

[165] J. R. Robertson, “Continued Developments in the Characteristics of HAYNES® 282® Alloy for Use in A-USC Applications,” in *ASME 2018 Symposium on Elevated Temperature Application of Materials for Fossil, Nuclear, and Petrochemical Industries*, 2018, p. V001T01A007-V001T01A007.

[166] R. W. Armstrong and S. M. Walley, “High strain rate properties of metals and alloys,” *Int. Mater. Rev.*, vol. 53, no. 3, pp. 105–128, 2008.

[167] W.-S. Lee and H.-C. Kao, “High temperature deformation behaviour of Haynes 188 alloy subjected to high strain rate loading,” *Mater. Sci. Eng. A*, vol. 594, pp. 292–301, 2014.

[168] W.-S. Lee, C.-F. Lin, T.-H. Chen, and H.-W. Chen, “Dynamic Impact Response of Inconel 718 Alloy under Low and High Temperatures,” *Mater. Trans.*, vol. 52, no. 9, pp. 1734–

1740, 2011.

[169] Y. Q. Ning, T. Wang, M. W. Fu, M. Z. Li, L. Wang, and C. D. Zhao, “Competition between work-hardening effect and dynamic-softening behavior for processing as-cast GH4720Li superalloys with original dendrite microstructure during moderate-speed hot compression,” *Mater. Sci. Eng. A*, vol. 642, pp. 187–193, Aug. 2015.

[170] M. Hörnqvist, C. Joseph, C. Persson, J. Weidow, and H. Lai, “Dynamic strain aging in Haynes 282 superalloy,” *MATEC Web Conf.*, vol. 14, p. 16002, 2014.

[171] Y. N. Dastur and W. C. Leslie, “Mechanism of work hardening in Hadfield manganese steel,” *Metall. Trans. A*, vol. 12, no. 5, pp. 749–759, 1981.

[172] Y. Yang, S. Luo, H. Hu, T. Tang, and Q. Zhang, “Diffusive transformation at high strain rate: On instantaneous dissolution of precipitates in aluminum alloy during adiabatic shear deformation,” *J. Mater. Res.*, vol. 31, no. 9, pp. 1220–1228, 2016.

[173] D. Huber, M. Hacksteiner, C. Poletti, F. Warchomicka, and M. Stockinger, “Thermomechanical behavior of different Ni-base superalloys during cyclic loading at elevated temperatures,” *MATEC Web Conf.*, vol. 14, p. 10002, 2014.

[174] H. C. Rogers and C. V. Shastry, “Material Factors in Adiabatic Shearing in Steels,” in *Shock Waves and High-Strain-Rate Phenomena in Metals*, Boston, MA: Springer US, 1981, pp. 285–298.

[175] P. C. Chou, J. Hashemi, A. Chou, and H. C. Rogers, “Experimentation and finite element simulation of adiabatic shear bands in controlled penetration impact,” *Int. J. Impact Eng.*,

vol. 11, no. 3, pp. 305–321, 1991.

[176] R. Dormeval, “The adiabatic shear phenomenon, In ‘Materials at High Strain Rates’, ed. by TZ Blazynski, London and New York.” Elsevier Applied Science Publishers LTD, 1987.

[177] J. M. Yellup and R. L. Woodward, “Investigations Into the Prevention of Adiabatic Shear Failure in High-Strength Armor Materials,” *Res. Mech.*, vol. 1, no. 1, pp. 41–57, 1980.

[178] Y. Xu, J. Zhang, Y. Bai, and M. A. Meyers, “Shear localization in dynamic deformation: microstructural evolution,” *Metall. Mater. Trans. A*, vol. 39, no. 4, p. 811, 2008.

[179] Z. Li, S. Zhao, H. Diao, P. K. Liaw, and M. A. Meyers, “High-velocity deformation of Al0.3CoCrFeNi high-entropy alloy: Remarkable resistance to shear failure.,” *Sci. Rep.*, vol. 7, p. 42742, Feb. 2017.

[180] W. Song, M. Hu, H. Zhang, and Y. Jin, “Effects of different heat treatments on the dynamic shear response and shear localization in Inconel 718 alloy,” *Mater. Sci. Eng. A*, vol. 725, pp. 76–87, 2018.

[181] J. Johansson, C. Persson, G. Testa, A. Ruggiero, N. Bonora, and M. H. Colliander, “Effect of microstructure on dynamic shear localisation in Alloy 718,” *Mech. Mater.*, vol. 109, pp. 88–100, 2017.

[182] C. H. Nguyen, “Analysis of some thermal instability criteria in the adiabatic shear banding process,” *Le J. Phys. IV*, vol. 7, no. C3, pp. C3-849, 1997.

[183] A. H. Chokshi and M. Meyers, “The prospects for superplasticity at high strain rates: preliminary considerations and an example,” *Scr. Met. Mater.*, vol. 24, no. 4, pp. 605–610,

1990.

[184] M. A. Meyers, *Dynamic behavior of materials*. John wiley & sons, 1994.

[185] L. C. D. Fielding and H. K. D. H. Bhadeshia, “Shear band structure in ballistically tested bainitic steels,” *Mater. Sci. Technol.*, vol. 30, no. 7, pp. 812–817, 2014.

[186] M. A. H Quinney, “The latent energy remaining in a metal after cold working,” *Proc. R. Soc. Lond. A*, vol. 143, no. 849, pp. 307–326, 1934.

[187] J. Liu, S. Li, A. Fan, and H. Sun, “Effect of fibrous orientation on dynamic mechanical properties and susceptibility to adiabatic shear band of tungsten heavy alloy fabricated through hot-hydrostatic extrusion,” *Mater. Sci. Eng. A*, vol. 487, no. 1–2, pp. 235–242, 2008.

[188] J. Liu, L. Shukui, Z. Xiaoqing, Z. Zhaohui, Z. Haiyun, and W. Yingchun, “Adiabatic shear banding in a tungsten heavy alloy processed by hot-hydrostatic extrusion and hot torsion,” *Scr. Mater.*, vol. 59, no. 12, pp. 1271–1274, Dec. 2008.

[189] S. X. Li, P. C. Zhao, Y. N. He, and S. R. Yu, “Microstructural evolution associated with shear location of AISI 52100 under high strain rate loading,” *Mater. Sci. Eng. A*, vol. 662, pp. 46–53, 2016.

[190] X. Wang, “Phenomenon of transformed adiabatic shear band surrounded by deformed adiabatic shear band of ductile metal,” *Trans. Nonferrous Met. Soc. China*, vol. 18, no. 5, pp. 1177–1183, Oct. 2008.

[191] X. B. Wang, “Effects of Temperature and Strain Rate on the Evolution of Thickness of

Transformed Adiabatic Shear Band," *Solid State Phenom.*, vol. 138, pp. 385–392, 2008.

[192] X. B. Wang, "Peak and Average Temperatures in Adiabatic Shear Band for Thermo-Viscoplastic Metal Materials," *Key Eng. Mater.*, vol. 345–346, pp. 133–136, 2007.

[193] R. Clos, U. Schreppel, and P. Veit, "Temperature, microstructure and mechanical response during shear-band formation in different metallic materials," *J. Phys. IV*, vol. 110, pp. 111–116, Sep. 2003.

[194] P. Guduru, A. Rosakis, and G. Ravichandran, "Dynamic shear bands: an investigation using high speed optical and infrared diagnostics," *Mech. Mater.*, vol. 33, no. 7, pp. 371–402, Jul. 2001.

[195] K. Cho, Y. C. Chi, and J. Duffy, "Microscopic observations of adiabatic shear bands in three different steels," *Metall. Trans. A*, vol. 21, no. 5, pp. 1161–1175, May 1990.

[196] M. Cohen, "Self-diffusion during plastic deformation," *Trans. Japan Inst. Met.*, vol. 11, no. 3, pp. 145–151, 1970.

[197] A. L. Ruoff and R. W. Balluffi, "Strain-enhanced diffusion in metals. II. Dislocation and grain-boundary short-circuiting models," *J. Appl. Phys.*, vol. 34, no. 7, pp. 1848–1853, 1963.

[198] R. W. Balluffi and A. L. Ruoff, "Enhanced diffusion in metals during plastic deformation," *Appl. Phys. Lett.*, vol. 1, no. 3, pp. 59–60, 1962.

[199] J. E. Lawrence, "The cooperative diffusion effect," *J. Appl. Phys.*, vol. 37, no. 11, pp. 4106–4112, 1966.

[200] A. R. Wazzan and J. E. Dorn, “Analysis of enhanced diffusivity in nickel,” *J. Appl. Phys.*, vol. 36, no. 1, pp. 222–228, 1965.

[201] T. E. Volin and R. W. Balluffi, “Direct Observation of Rapid Self-diffusion along Dislocations in Aluminum,” *Appl. Phys. Lett.*, vol. 11, no. 8, pp. 259–261, 1967.

[202] Z. Liu, S. Bai, X. Zhou, and Y. Gu, “On strain-induced dissolution of θ′ and θ particles in Al–Cu binary alloy during equal channel angular pressing,” *Mater. Sci. Eng. A*, vol. 528, no. 6, pp. 2217–2222, 2011.

[203] Y. Wang, W. Shao, and L. Zhen, “Dissolution behavior of δ phase and its effects on deformation mechanism of GH4169 alloy,” *Chinese J. Nonferrous Met.*, vol. 21, no. 2, p. 341í342, 2011.

[204] R. Liang and A. S. Khan, “A critical review of experimental results and constitutive models for BCC and FCC metals over a wide range of strain rates and temperatures,” *Int. J. Plast.*, vol. 15, no. 9, pp. 963–980, 1999.

[205] A. Cingara and H. J. McQueen, “New formula for calculating flow curves from high temperature constitutive data for 300 austenitic steels,” *J. Mater. Process. Technol.*, vol. 36, no. 1, pp. 31–42, Dec. 1992.

[206] H. Mirzadeh, J. M. Cabrera, J. M. Prado, and A. Najafizadeh, “Hot deformation behavior of a medium carbon microalloyed steel,” *Mater. Sci. Eng. A*, vol. 528, no. 10–11, pp. 3876–3882, Apr. 2011.

[207] Z. Akbari, H. Mirzadeh, and J.-M. Cabrera, “A simple constitutive model for predicting

flow stress of medium carbon microalloyed steel during hot deformation," *Mater. Des.*, vol. 77, pp. 126–131, Jul. 2015.

[208] Y. C. Lin, D. X. Wen, J. Deng, G. Liu, and J. Chen, "Constitutive models for high-temperature flow behaviors of a Ni-based superalloy," *Materials and Design*, vol. 59. pp. 115–123, 2014.

[209] Z. Hao, F. Ji, Y. Fan, J. Lin, X. Liu, and S. Gao, "Flow characteristics and constitutive equations of flow stress in high speed cutting Alloy 718," *J. Alloys Compd.*, vol. 728, pp. 854–862, Dec. 2017.

[210] Y. C. Lin, F.-Q. Nong, X.-M. Chen, D.-D. Chen, and M.-S. Chen, "Microstructural evolution and constitutive models to predict hot deformation behaviors of a nickel-based superalloy," *Vacuum*, vol. 137, pp. 104–114, Mar. 2017.

[211] W. Wang, J. Zhao, R. X. Zhai, and R. Ma, "Arrhenius-Type Constitutive Model and Dynamic Recrystallization Behavior of 20Cr2Ni4A Alloy Carburizing Steel," *steel Res. Int.*, vol. 88, no. 3, p. 1600196, Mar. 2017.

[212] J. J. Jonas, X. Quelennec, L. Jiang, and É. Martin, "The Avrami kinetics of dynamic recrystallization," *Acta Mater.*, vol. 57, no. 9, pp. 2748–2756, May 2009.

[213] G. Chen, C. Ren, Z. Ke, J. Li, and X. Yang, "Modeling of flow behavior for 7050-T7451 aluminum alloy considering microstructural evolution over a wide range of strain rates," *Mech. Mater.*, vol. 95, pp. 146–157, 2016.

[214] Y. Tian, L. Huang, H. Ma, and J. Li, "Establishment and comparison of four constitutive

models of 5A02 aluminium alloy in high-velocity forming process," *Mater. Des.*, vol. 54, pp. 587–597, 2014.

[215] G. Ji, Q. Li, and L. Li, "A physical-based constitutive relation to predict flow stress for Cu–0.4 Mg alloy during hot working," *Mater. Sci. Eng. A*, vol. 615, pp. 247–254, 2014.

[216] H. Li, X. Wang, J. Duan, and J. Liu, "A modified Johnson Cook model for elevated temperature flow behavior of T24 steel," *Mater. Sci. Eng. A*, vol. 577, pp. 138–146, 2013.

[217] G. Quan, Y. Shi, C. Yu, and J. Zhou, "The improved arrhenius model with variable parameters of flow behavior characterizing for the as-cast AZ80 magnesium alloy," *Mater. Res.*, vol. 16, no. 4, pp. 785–791, May 2013.

[218] G. Quan, G. Li, Y. Wang, W. Lv, C. Yu, and J. Zhou, "A characterization for the flow behavior of as-extruded 7075 aluminum alloy by the improved Arrhenius model with variable parameters," *Mater. Res.*, vol. 16, no. 1, pp. 19–27, 2013.